UNIVERSITÀ DEGLI STUDI DI MILANO

DIPARTIMENTO DI FISICA

CORSO DI DOTTORATO DI RICERCA IN

FISICA, ASTROFISICA E FISICA APPLICATA

CICLO XXIX

Smart materials for stretchable electronics, sensors and soft actuation

Settore Scientifico disciplinare FIS/03

Tesi di Dottorato di:

Andrea Bellacicca

Coordinatore: Prof. Francesco Ragusa

Supervisore: Prof. Paolo Giuseppe Carlo Piseri

Co-Supervisore: Prof. Paolo Milani

A.A. 2015-2016

Commission of the final examination:

External Member:

Prof. Federico Carpi

External Member:

Prof. Arianna Menciassi

Internal Member:

Prof. Paolo Milani

Final examination:

Date February 20, 2017

Università degli studi di Milano, Dipartimento di Fisica, Milano, Italy

A mia madre Simona, mio zio Paolo

e mio nonno Luigi

1 Introduction

Over the past few decades, the semiconductor industry has experienced a striking growth. In fact, since 1970s the number of transistors integrated on a chip has doubled every 2 years circa (first Moore's law). This has resulted in improved performances, reduced power and lowered cost of chips, favoring the word-scale diffusion of electronic devices in several fields. For example, healthcare has been positively influenced by introducing new sensors and electronic tools for diagnostic and monitoring. More computational power has led to the developing of new advanced artificial intelligences that are exploited in factories to automatize part of the manufacturing processes, often in combination with robotic apparatus. Moreover, electronic devices striking diffusion has deeply influenced our habits, completely changing the way we live, work and learn.

By 2025, advances in mobile computing and cloud connectivity combined with the growth of sensor networks will have been setting the basis for a cyber-physical world with ubiquitous computing capability [1]. Sensors will be embedded into objects [2], clothes [3, 2] or widely distributed in the environment [2]: the networked sensor systems will enable real-time data processing on wireless computing devices, creating intelligent and adaptive cyber environments (called internet of things) for emerging applications such as autonomous transportation systems [4], smart diagnostic systems for health [5], food packaging [6], predictive maintenance [7], energy harvesting [8] etc. It is expected that by 2020 the number of interconnected electronic devices equipped with sensing and actuation functionalities will grow up to trillions of connected units, i.e. 1000 elements per person [9].

Usually, electronic devices, sensors and actuators are made by hard materials and all the functionalities rely only on the electronic circuit architecture and on the software embedded in the device chip. This approach has serious

drawbacks since a rigid structure imposes severe limitations on the device application domains. In some cases, it is possible to overcome these limitations augmenting the complexity either of the device physical structure or of the embedded software, resulting in an unwanted great increase in the final cost or in degraded performances.

Thus, it is strategic to develop materials that facilitate disruptive or transformative changes while being fully compatible with standard electronics [10]. These smart materials do not act just as static structural components, but they actively interact with the environment and respond to external stimuli altering their physical properties (e.g. electrical, optical, mechanical etc.) in a way that can be exploited to improve the functionalities of a device. One of the main requirements for these

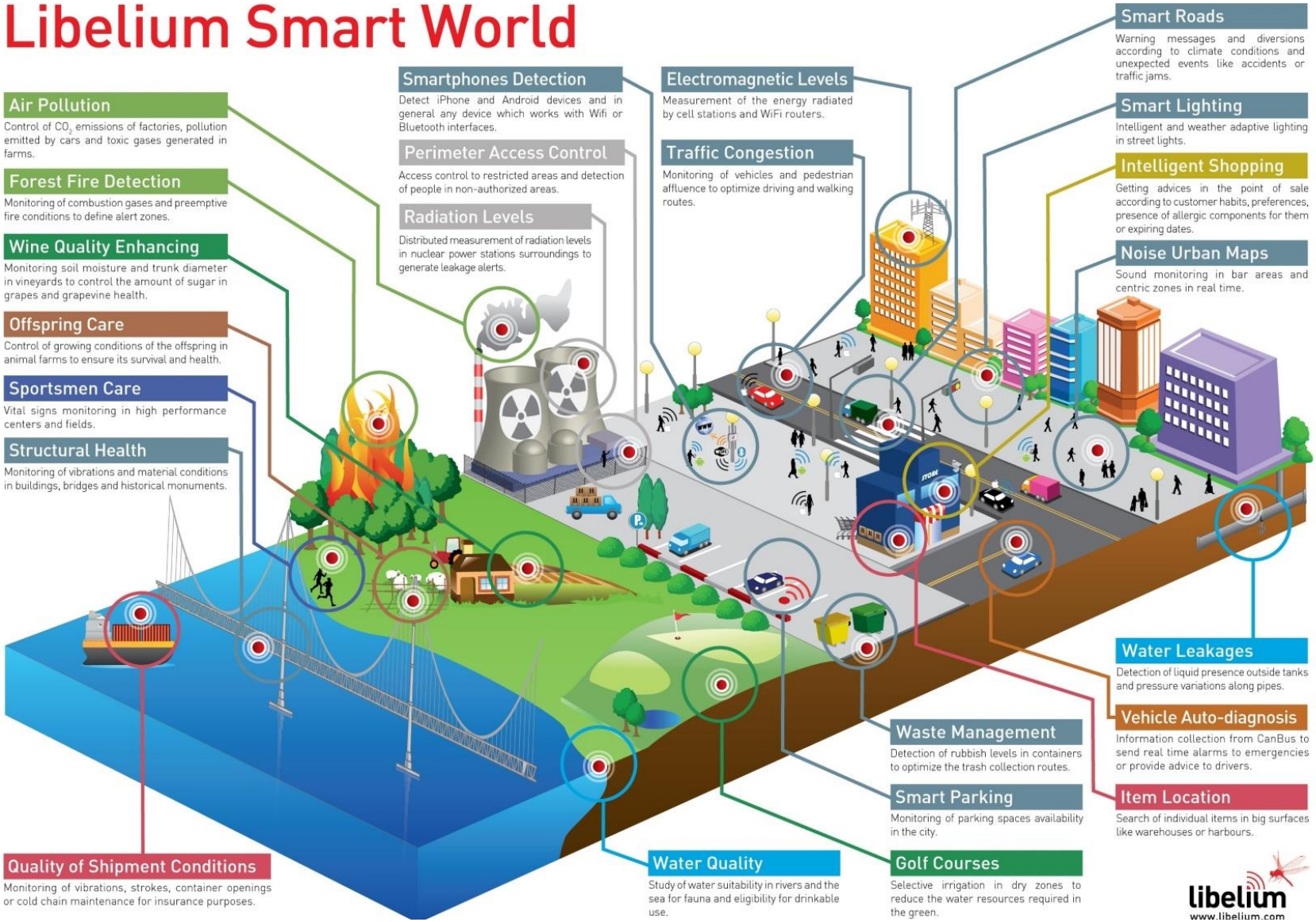

Figure 1: *Advanced information and electronic technologies will be used to enhance the performance and interactivity of urban services to improve life quality, to reduce costs and resource consumption. To address this challenge, new materials with novel functionalities are required to bring disruptive innovations [146].*

materials, is stretchability, defined as the ability to withstand large deformations during usage (millions of times) [11] without any loss of functionality due to mechanical or electrical failure [12].

A typical example is the adjustment of the focal length of an eye, in contraposition with the one of a camera [13]. A camera adjusts its focal length by zooming (a rigid-body translation) while an eye does so by deforming the lens. It implies that zooming is unsuitable for thin smartphones, that use instead dedicated algorithms to obtain a similar but still cheaper results (software corrections) or complicated actuator-lens complexes based on micro electro-mechanical systems (complex device structure). Instead a deformable lens would fit the need while keeping the design simple: an elastomeric lens can change its curvature by deforming in response to an applied voltage [14].

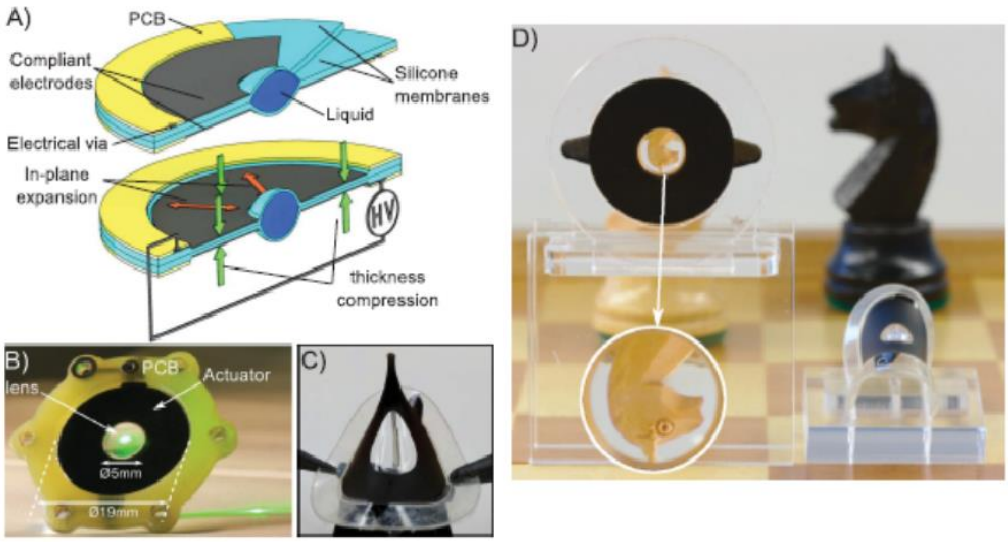

***Figure 2**: A) Schematic of an elastomeric lens with two compliant electrodes patterned around it, encapsulating a transparent fluid, forming a biconvex lens. When a voltage is applied the expansion of the electrode due to Maxwell pressure compresses the lens in-plane, causing a decrease in the focal length.*

B) Picture of the device. C) Extreme deformation of the lens to show its resilience. D) The lens showing a white knight of chess set [15]

Another example inspired from nature is the regulation of water flow inside the microchannels in the plants. The flow is changed in response to variation of salt concentration mediated by pectins [16], polysaccharides that are present in jellies and jams. The pectins absorb water forming a hydrogel that swells according to the concentration of salt. The swelling alters the size of microchannels regulating in turn the rate of the flow. The swelling of gels can be exploited to regulate the flow of liquid in microfluidic devices [17] used for medical diagnosis.

Polymers are the best candidates to be used in smart material fabrication because of their structural and functional properties that can be easily tuned. Moreover, they are low-cost, versatile and can be processed into any shape including thin films. Anyway, polymers do not provide all the needed functionalities on their own (most of the polymers are not electrically conductive and this means that they cannot directly be used in conjunction with classic electronic elements), but they have to be used in conjunction with hard materials, like metals, semi-conductors or standard electronic components too [13]. Novel functionalities can be obtained by combining electrical and mechanical properties from all classes of materials (e.g. gels, rubbers, metals, semi-conductors, etc.).

1.1 Soft Actuators

An actuator is a mechanical device for moving or controlling a system. Typical actuators include motors, servomotors, pneumatic actuators, etc. Robots embedding these actuators are perfect for repetitive work in a structured environment, due to their fast and precise operation. But they fail to be effective whenever they have to deal with uncertainty and highly dynamic tasks because they are composed of rigid materials [18], like alloys, metals and magnets that

hardly adapt to the surroundings. They are unsuitable for all that applications that require the system to interact with an unstructured and complex environment, for example locomotion in irregular and unknown terrain or grasping of unknown objects. Moreover, the high-power consumption, limited size, restrictive shape and the weight have led researcher to investigate alternative technologies. New forms of soft actuators are being explored mimicking nature to enable a host of novel applications that span from consumer and mobile appliances to biomedical systems, sports, and healthcare [19, 20].

Soft actuators can be exploited in many areas like soft robotics [21, 22], haptic devices for touch interaction with humans [23, 24], tunable optics [14, 25, 26] and camouflage systems [27, 28], microfluidics [29, 30] and energy harvesting [31, 32]. Compared to their rigid counterparts, soft actuators have several unique properties that make them able to perform task that would be difficult or impossible to achieve with rigid motors and mechanicals joints. In fact, a system based on rigid actuators works by moving rigid parts relative to each other. On the contrary, a soft actuator can modulate its entire shape or can change its stiffness locally, providing distributed actuation, enabling the system to adapt to the environment and enhancing the performances. Materials having a wide range of mechanical and chemical properties can be employed: from liquids and gels to organic and inorganic solids.

Soft actuators can achieve actuation by employing a variety of methods. They include actuation with the aid of pressurized fluids [21, 33] (liquid or air), shape-memory alloys [34], chemical reactions [35], temperature [36], humidity [37], and electric charges [20]. Among these, pneumatic soft actuators, are particularly attractive because their ease of fabrication, safety operation and low cost. They resemble smart air balloons with complicate system of inflatable chambers that are swollen and deflated to make the system move [21]. These

actuators need an air compressor and complex software to manage the movements, this imply that they fit very well only in industrial environments, although there exist some examples of inflatable robots that can work in real environments. In order to extend the application domain of soft actuators, they need to rely on electrical energy to move, because electricity is easy to store and deliver. To make them a valid alternative to classical actuators, several issues are yet to be solved.

1.2 Paper electronics

Flexible electronics enable the fabrication of electronic circuits that can be bent without compromising the device functionalities. They typically implement organic materials as flexible substrate. A standard one side flexible printed circuit board (PCB) has a five-layers architecture: 1) a base layer of polyimide, 2) a layer of adhesive, 3) a layer of copper, 4) a second layer of adhesive and 5) a cover layer of polyimide [38]. Although this design is inexpensive and convenient when large quantities of circuits are required, it leads to circuits with limited flexibility, e.g. it is impossible to fabricate permanent 3D folded shapes. It is also expensive when small-quantity production and prototyping are required [38]. Because of these reasons, over the last years, novel materials have been proposed to substitute polyimide. Among them, paper has been targeted as a possible alternative to polyimide for low-cost flexible electronics [39, 40].

Paper, can be broadly defined as thin, porous sheet. It is by far the cheapest and most widely used flexible substrate in daily life, mainly used for packaging and for displaying and storing information. It is foldable and can be easily trimmed for tailoring it to specific needs [41], it has the ability to wick fluids via capillary action and it can be used as a cell for filtering and separating microscopic components. Furthermore, paper is also environmentally friendly,

since it is recyclable and made of renewable raw materials. Paper was used for the first time as a substrate for electronic components in the late 1960s [42, 43]: thin-film transistors were deposited onto paper on a roll inside a vacuum chamber. Nowadays, paper is used in several electronic disposable applications including: low-cost portable diagnostic system [44] for medical and biological use, self-assembling robots [45], teaching aids [40], toys [41]. However, integrating new materials and electronic components with paper is not an easy task due to the nature of the substrate, making electronic on paper far from being truly used in advanced applications.

1.3 Aim of the work

This work aimed to address the issues related with the fabrication of novel smart materials that can be used in advanced electronic devices or innovative actuation systems. Current fabrication processes fail to attend all the requirements demanded to produce robust smart materials that can be successfully employed in real world applications: smart materials are either too fragile or the reproducibility of the manufacturing processes is not assured because of their complexity. Exploiting techniques named Supersonic Cluster Beam Implantation (SCBI) and Supersonic Cluster Beam Deposition (SCBD), I demonstrated that it is possible to produce new smart materials, designing both their electrical and mechanical properties with sharp precision.

Different new smart materials have been produced to obtain sensors, actuators and electronic devices, combining different hard materials with soft ones. Their electrical and mechanical properties have been characterized. Actuators based on silver/polydimethylsiloxane nanocomposite are presented. Electronic components based on gold/paper nanocomposite have been fabricated by SCBD. Two hybrid devices based on smart materials interacting with classic

electronic components have been realized to demonstrate that SCBI is an effective way to fabricate robust smart materials with precise physical properties. The electronic circuits take full advantage from the properties of the smart materials making possible the realization of devices with extended functionalities that can be used in real world applications. The performance of these devices has been tested under different stress conditions that classical electronic circuits are not able to stand.

2 Metal-polymer nanocomposites

Stretchable electronic circuits [46], artificial skins [47], artificial neural networks [48], artificial muscles [20], energy storage systems [49], energy harvester systems [50], wearable electronics [3], diagnostic devices [5] are just a few of many examples where materials with cutting-edge features that could be customized regulating their physical properties are demanding. These materials are not only used as an alternative substrate for standard electronic devices, but they can provide new functionalities because they can respond to external stimuli altering their physical properties. Thus, it means that they can be used as active components in innovative devices. These smart materials are mostly hybrids of hard and soft materials [13]. Materials with novel and emergent properties can be produced combining different materials in a composite in such a way they can benefit from a synergic coupling interaction among the constituents.

Combining two or more known substances into a composite has become an effective way for developing entirely new materials with unique properties not obtainable in existing materials. Although each component maintains its chemical and structural identity, the composite shows superior characteristics to those of its constituents [51]. A typical example is fiberglass-reinforced plastics

developed during 1940s, where fiber materials are dispersed in plastic materials to mechanically enhance the strength and elasticity of plastics. When the dimension of at least one component is in the range of a few angstroms to tens of nanometers, the material is called nanocomposite. Shrinking the size to the nanometric scale leads to a great enhancement in the properties of the nanocomposite. Moreover, novel and emergent properties that are not exhibited by any of the constituents in the composite can be produced. This synergic integration of different materials to form nanocomposites provides new opportunities and strategies for fabricating smart materials with desired properties for specific applications. Examples of these materials include polymer-based, metal-based, oxide-based and organic-inorganic hybrid nanocomposites.

The macroscopic properties of nanocomposites depend not only on the properties of their constituents and their microstructures, but also the spatial arrangements of these constituents play an important role in determining the ultimate functionalities of the nanocomposites [51]. Figure 3 shows the most commonly architectures typical implemented in actual nanocomposites.

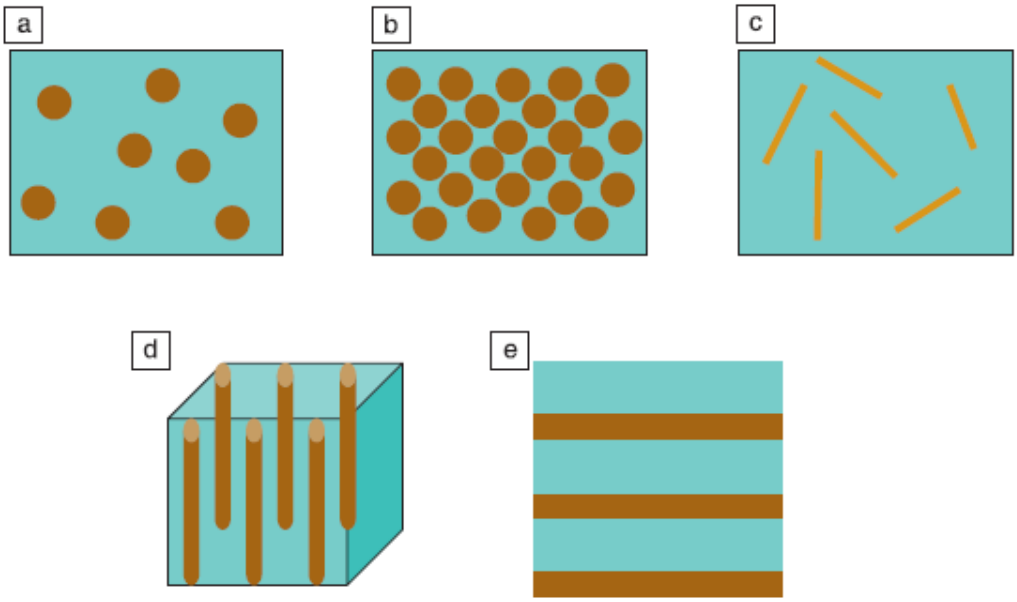

***Figure 3**: Schematic illustrations of the most commonly investigated nanocomposite architectures: a) nanoparticles dispersed in a matrix; b) periodic nanoparticles arrangement obtained by self-assembly; c) nanocomposite with nanofibers dispersed in a matrix; d) nanofibers aligned in a matrix; e) single or multi-layer nanocomposite thin films [46]*

In this work, we are interested in developing and characterizing the electrical and mechanical properties of innovative smart materials that can be used as electronic components, sensors and actuators. They are typically made by conductive metallic layer deposited on a soft insulator substrate (nanocomposites films and layered nanocomposites Figure 3-e) or metal nanoparticles dispersed in a polymeric matrix [52] (Figure 3-a). As already stated, polymers are very attractive materials because their mechanical and functional properties. In fact, in a nanocomposite system metal and polymer are coupled together to form a new material at the nanoscale level. This leads to a better adhesion between the polymer and the metal, reducing the mechanical

instabilities and avoiding debonding during mechanical stresses. Moreover, it is possible to fabricate full stretchable conductive electrodes.

The mechanical and electrical properties of nanocomposites can be tuned controlling the inclusion of metallic clusters within the polymeric matrices and this makes possible to obtain smart materials that exhibit interesting mechanical and electronic properties [53, 54, 55] exploited for a host of technological applications [52, 56, 57] that span from transparent conductive films [58] to stretchable electronics [59], from sensors [60] to switching devices [61] and soft actuators [20].

These smart materials combine soft and elastic materials with hard and brittle materials, raising mechanical contrasts with amazing consequences. For example, a hard solid like a metal become unusually deformable when bonded to an elastic polymer [62]. But mixing two or more materials with great differences in mechanical properties into a new one is a challenging task. The elastic modulus, or Young's modulus, of the materials used spans a range of circa 12 orders of magnitude. Soft materials, like gels, for example have a Young's modulus of 200 Pa. Elastomers and rubbery materials Young's Modulus range from 1 to 100 MPa. Hard materials like gold, silicon and graphene hit values greater than GPa.

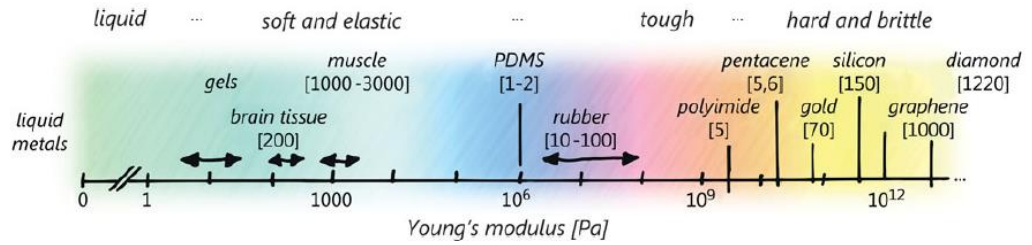

Figure 4*: Smart materials can be made combining different kind of material with many orders of magnitude differences in Young's modulus: elastic, plastic, brittle*

materials etc. The numbers in brackets are in Pa for soft, MPa for tough, and GPa for hard materials, respectively [51]

2.1 Nanocomposites fabrication

Several approaches such as wet chemical techniques (reduction of a metal salt) or vapor phase deposition techniques (plasma polymerization in conjunction with metal deposition [63], co-evaporation of a metal and an organic component [64], and co-sputtering [65], ion implantation [66], supersonic cluster beam implantation [67]) have been reported to produce polymer composites containing metal nanoparticles. Vapor phase deposition techniques are well suited for those applications that require good control of the metal filling factor and filling factor profile (i.e. nanoparticles distribution inside the polymeric matrix). On the contrary, wet chemical methods often offer much better control on particle size and shape [68].

Nanocomposite fabrication processes are named either in situ or ex situ according to the methods used to assemble nanoparticles [69]. In an in-situ process, nanoparticle precursors are incorporated in liquid monomers or within the polymeric matrix. Nanoparticles form through the reduction of precursors with chemical, thermal of UV radiation exposure or self-organization. Otherwise in an ex situ process, nanoparticles are first synthesized and then mixed to a monomer that is polymerized or they are dispersed in a polymeric matrix. The nanoparticles surface is often functionalized through thiol-metal covalent bonds [70], or by coating with a suitable polymeric shell [71] to limit clusters aggregation.

Since the physical properties of a metal-polymer nanocomposite strictly depend by the ratio between the amounts of their constituents, it is relevant to introduce a physical quantity called *filler volume fraction* $\mathbf{\Phi}$ before discussing

physical properties. It is defined as the ratio between the total volume of the metal clusters (filler) $\mathbf{V_{clust}}$ in the polymer matrix and the total volume of the nanocomposite $\mathbf{V_{nc}}$:

$$\Phi = \frac{V_{clust}}{V_{nc}} \quad (2.1)$$

The filler volume fraction is a key parameter to refer to since it plays a crucial role in nanocomposites fabrication: controlling its value means being able to control nanocomposite physical properties.

In addition to the filler volume fraction, also metal-polymer adhesion and patterning need to be considered in nanocomposites fabrication.

Adhesion of metal on a polymeric substrate is a critical parameter because it strongly influences how metal behaves when the substrate undergoes mechanical deformations. Consider for example a metallic thin film deposited on a polymer substrate: a mismatch in thermal expansion of the polymer and the metal can generate a stress sufficient to delaminate the metal layer from the polymeric substrate. Adhesion depends by the method exploited to fabricate the metal-polymer interface and, of course, by the materials involved. The adhesion problem intensifies when we are dealing with flexible or stretchable substrates. In this case the metal-polymer interface must sustain large strains preserving the system functionalities. The maximum strain attainable for a metal depends by the adhesion on the polymer substrate [72]. In case of no adhesion, the maximum strain that a freestanding thin film can tolerate without breakage is smaller than the rupture strains of the corresponding bulk metals, and it is approximately of 2% [73, 74]. In fact, in this case the metal film experiences a localized deformation concurrently with the deformation of the whole system, called necking, that weakens the film in a specific region. On further deformation of the

whole system, all the deformations of the metal film concentrate on the neck region causing a rupture [75, 76].

The adhesion to the substrate is a crucial aspect to assure the highest maximum strain attainable for a system, however adhesion is not the only key parameter. The possibility to fabricate conductive patterns with specific geometries is a key point to integrate electronics on polymer. There exist many lithography techniques capable to pattern circuits on silicon wafers, but their use with polymeric substrate is not obvious because of the aggressive chemical agents involved in the process. These chemical agents can damage and contaminate the polymeric substrate, compromising its mechanical and functional stability. A better approach is thus using stencil masks, which do not require the use of chemicals, but on the contrary it can suffer from shadowing effects that lower the achievable lateral resolution. Patterning is also a relevant parameter because it is possible to improve further the stretchability of a particular metal-polymer nanocomposite. Indeed, depending by the application, a particular material could be subjected just to a single type of deformation (see Figure 5) and knowing it a-priori could be exploited to optimize its stretchability with geometric considerations on the shape of the metallic electrodes. This implies that the best strategy to create a nanocomposite has to be chosen on a case-by-case basis.

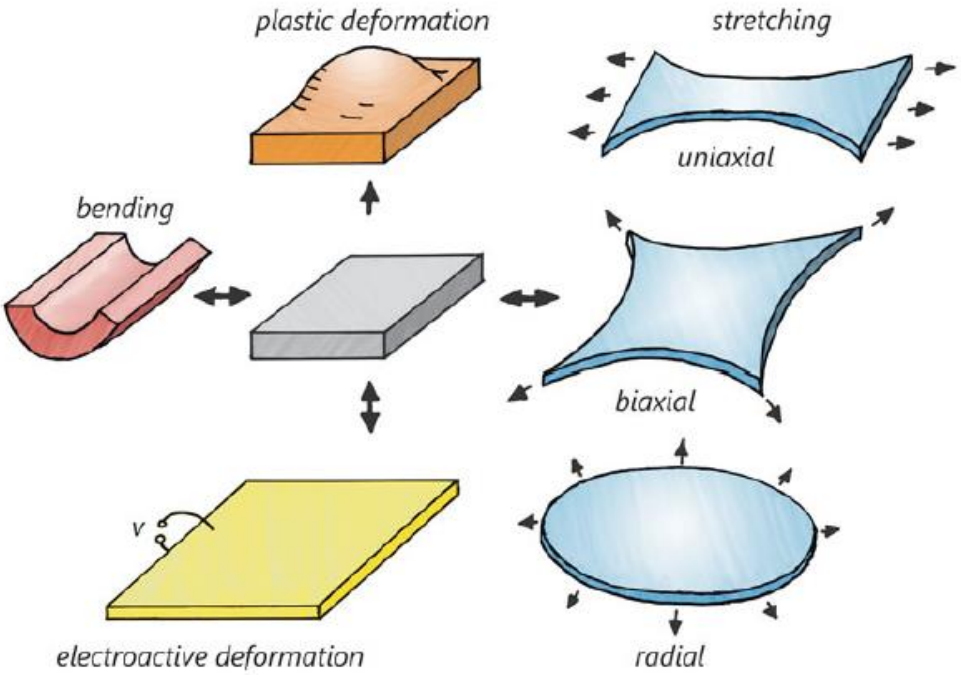

Figure 5*: A substrate can be subjected to several kinds of deformation: bending, uniaxial stretching, biaxial stretching, radial stretching etc. Knowing a priori which kind of deformation a device will be subject to, could help optimize its stretchability [46].*

Hereafter are described the most common techniques [68] used to fabricate metal/polymer nanocomposites.

2.1.1 Vapor phase deposition

Vapor phase depositions techniques are a class of nanocomposites synthesis methods [77, 78] that rely generally on the co- or tandem deposition of metallic and organic components and subsequently formation of metallic nanoparticles by self-organization. The self-organization process that occurs during the fabrication of the nanocomposite is similar to the process that leads to metal clusters formation on a polymer surface [79]. When energetic metal atoms

impinge on the polymer surface they undergo several processes, e.g. random walk on the surface, diffusion into the bulk or desorption [80]. Metal atoms are led to aggregate into stable clusters whenever they interact with other metal atoms or when they are captured by a surface detect, within their diffusion distance. The clusters are then embedded upon growth of the nanocomposite film. The volume filling factor, i.e. the metal/polymer ratio, depends either by the condensation coefficient of metal atoms on a given polymer surface [81] and by the metal/polymer deposition ratio [82].

These techniques are extensively used because of the possibility to tune the nanocomposites physical properties controlling the volume filling factor over the whole range from zero to unity. Lots of polymers/metal nanocomposites were successfully produced in such a way. Nonetheless, there are several major drawbacks related with them. In fact, it is reported a simultaneous increase of filling factor and particles size that induces a dramatic morphology variation [68]. Moreover, many of these techniques cause physical or chemical modification of the polymer, giving rise to poor mechanical properties [83].

2.1.1.1 Plasma polymerization

Plasma deposition is a versatile method for the preparation of metal-polymer nanocomposites [84, 63, 85]. A typical procedure consists in plasma polymerization of organic precursors and concurrent sputtering from a metal target. A large variety of polymers and metals can be used. The metal filling factor can be easily changed from a few percent to almost up to 100%, with a homogeneous metal nanoparticles distribution inside the polymeric matrix.

2.1.1.2 Evaporation and sputtering deposition

Nanocomposites can be fabricated also with co- or tandem evaporation or sputtering of both monomers and metals precursors. In the evaporation process,

the nanocomposite is formed by means of evaporation of monomers and subsequently polycondensation on the substrate [64], or by thermal cracking of suitable polymers and partial repolymerization of the fragments on the substrate [78]. For what concern sputtering deposition process, an RF magnetron sputters the target polymer while metal atoms are sputtered with a dc sputter from a metal or alloy target [86, 65].

In co-evaporation, the energy of the metal atoms impinging the polymer surface is very low compared to co-sputtering. This implies that the structure of the nanocomposite not only depends by the metal/polymer deposition rate ratio but also on the sticking coefficient of the metal atoms on the polymer surface [82].

These kinds of nanocomposites are considered to be a very attractive option because the absence of solvents and catalysts in the processes used for their fabrication. A major problem related with this technique is the deposition rate, which in many cases is too low for large-scale applications.

2.1.1.3 Ion implantation

Ion implantation is one of the most and widely used methods to insert ions or ionized particles within a material and it can be exploited to produce metal-polymer nanocomposites. Its working principle is schematized as follow: metallic ions are produced within a source through electronic ionization, electrical discharge or radioactive ion. The ions are then extracted from the source, accelerated by an electric field and mass selected through a magnetic field. After that, the ion beam is accelerated again with a second electric field and collimated by means of a magnetic quadrupole. The beam eventually intercepts the substrate target. It is possible to pattern the substrate due to two pairs of scan electrodes that orient the collimated beam to specific points of the target [83].

A nanocomposite fabricated in this way is able to sustain large deformation while remaining conductive. Nevertheless, its mechanical and electrical properties cannot be tailored independently from each other [87]: to obtain stretchable conductors, low ion doses must be used, so only conductors with high resistivity can be produced. On the contrary, a good conductive nanocomposite has poor mechanical performances. Moreover, the energy involved in the implantation process, causes the carbonization of the polymeric chains, leading to reduced elastic properties [83].

2.1.1.4 Supersonic cluster beam implantation

Supersonic cluster beam implantation (SCBI) [88] has recently gained a lot of attention for metal-polymer nanocomposites production and it will be discussed in detail in the next chapter. It consists in directing a highly collimated beam of electrically neutral metallic nanoparticles towards a polymeric substrate (in opposition with the use of atoms or ions like in the previous cases). The low energy (0.5 eV/atom) owned by the clusters is sufficient to allow the nanoparticles to enter the polymeric matrix, avoiding charging and carbonization to the polymeric substrate. Nanocomposites made with SCBI have good electrical and mechanical properties [89] that can be easily tuned controlling the amount of cluster implanted [89]. The implantation process guarantees good mechanical adhesion between the polymer and the metal nanoparticles. Because of the highly collimated beam SCBI is compatible with patterning by means of stencil masks, but at the same time the area hit by the clusters is as small as few centimeters. Thus, SCBI is coupled with a set of moving samples holder to allow large area implantation [67].

2.1.2 Wet chemical techniques

Wet chemical techniques include both in situ and ex situ procedures. In situ approach is used in the majority of the cases [90, 91, 92]. Nanoparticles are

formed within the polymer typically by the reduction of a metal salt or the decomposition of a metal complex. On the contrary, in ex situ techniques, the nanoparticles are synthetized separately with chemical methods which permit the exact control of particles size and shape [93]. The nanoparticles are often functionalized with organic tails to prevent aggregation and to improve solubility. Eventually, they are dispersed in a monomer solution for subsequent polymerization. Monodispersed nanoparticles can be used in optical application, e.g., to obtain sharper particle plasmon resonances [68], or in magnetic data storage [94]. One of the major drawbacks is due to the impossibility to obtain nanocomposites with high values of filler factor. In fact, a large amount of nanoparticles interferes with the polymerization process. Also, patterning is very difficult because of the random nature of the dispersion process making impossible to have the nanoparticles at fixed position in the liquid monomer.

2.2 Structural and functional properties

The possibility to control the filling factor of a nanocomposite means being able to fabricate nanocomposites with well-defined mechanical and electrical properties. Features like elastic modulus, tensile strength, hardness and conductivity can be tuned [95, 96] in this way.

2.2.1 Mechanical properties

Several models to describe the mechanical properties of metal/polymer nanocomposites have been proposed, but due to the high complexity of the system and the large number of polymers and fillers used, a general model is far from being developed. Nonetheless, several decades ago Guth and Gold introduced a quadratic equation that well describe the reinforcing effect observed in elastomers with spherical fillers, starting from the Smallwod-Einstein equation and taking into account the interaction between the filler particles [97].

The equation relates the elastic modulus (Young's modulus) of the nanocomposite with the elastic modulus of the pristine polymer and the filling factor:

$$E = E_m[1 + 2.5\Phi + 14.1\Phi^2] \quad (2.2)$$

Where E is Young's modulus of filled elastomer, E_m is matrix Young's modulus and Φ is the filling factor. This equation can be applied just for a small amount of spherical filler [98]. If the filler concentration is higher than 10%, the modulus increases more rapidly than the equation would predict because of the formation of a network by the spherical filler chains. This led Guth to introduce a shape factor α (length/breadth) to take also in account the evolving structure of the spherical filler [99].

The equation is then modified:

$$E = E_m[1 + 0.67\alpha\Phi + 14.1(\alpha\Phi)^2]$$

Figure 6 shows the effect of the shape factor for increasing values of the filling factor.

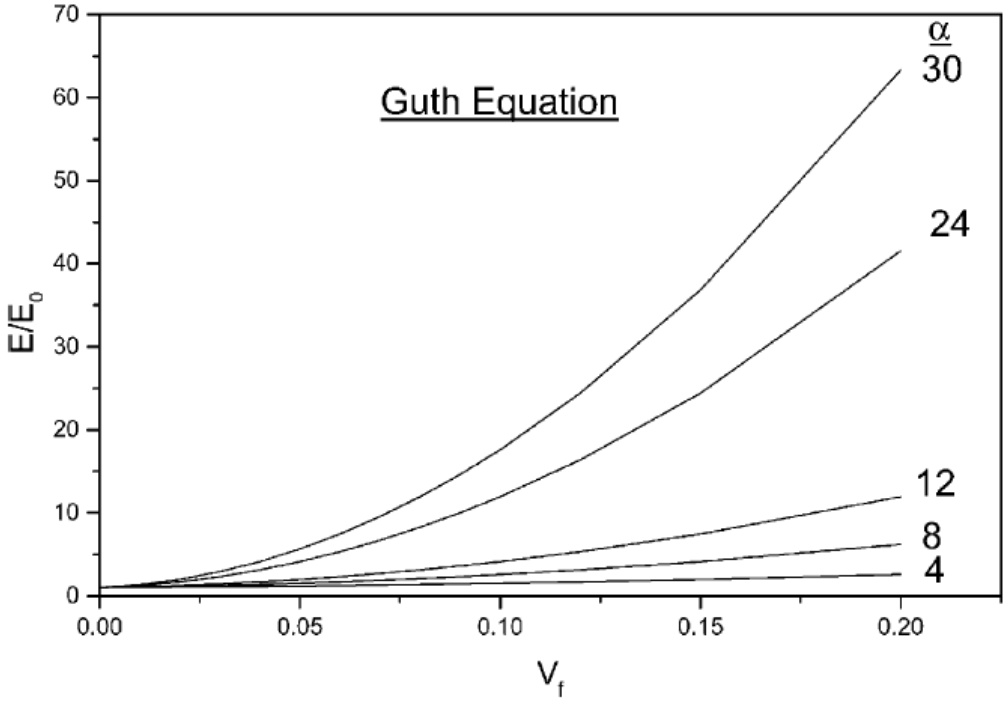

Figure 6: *Effect of the aspect ratio α on the modulus ratio in Guth equation [98]*

The modified Guth equation can be used to predict the modulus of polymers with spherical fillers over a wide range of filling factor [98].

2.2.2 Electrical properties

The electrical transport mechanism for a metal-polymer nanocomposite varies from insulating to metallic as a function of the filler volume fraction. It is possible to distinguish three different conduction regimes according to the metal filler concentration [100], as showed in Figure 7:

- **Dielectric regime:** for low values of the filler volume fraction, the nanoparticles immersed in a dielectric medium are well isolated from each other's. Thus, the system is almost insulating. Electrical conduction,

if present, is ascribed to tunneling effects or temperature activated hopping.

- **Transition regime:** in this regime, the nanocomposite shows random insulator-conductor mixture behaviors. The clusters begin to touch each other's forming the first conductive paths. The resistivity of the nanocomposite drops over many orders of magnitude when a critic filler volume fraction is reached [101, 102]. This transition is generally modeled within the framework of percolation theory as a 3D network of electrically connected filler particles distributed along the film matrix [103, 104].
- **Metallic regime:** when the filler factor tends to unity, the nanoparticles are well connected and the electrical transport shows Ohmic behaviors typical of thin metallic films.

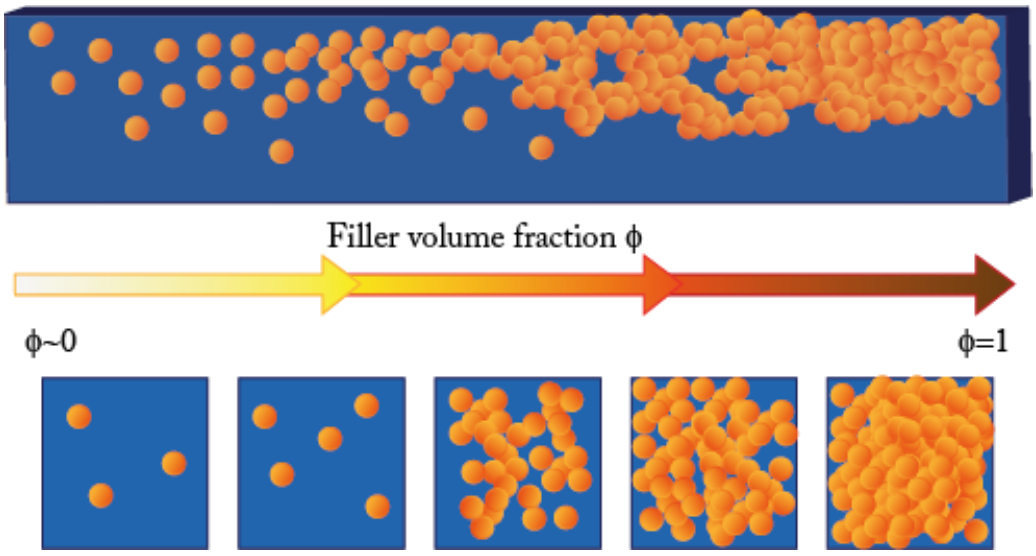

***Figure 7**: For low values of the filler volume fraction, the nanoparticles immersed in a dielectric medium are well isolated from each other's. The system is insulating. Increasing the filler volume fraction, we reach a critical point*

where the resistivity of the nanocomposite drops over many orders of magnitude, showing percolative behaviors. When the filler factor tends to unity, the nanoparticles are well connected and the nanocomposite shows Ohmic behaviors [105].

While metal-polymer nanocomposites with low values of filler volume fraction (dielectric regime) are mostly used in optical applications, nanocomposites with a filling factor above the critic value are interesting for their electrical and mechanical properties. Stretchable conductive electrodes are made patterning metal clusters on a polymer to produce a nanocomposite with a high filling factor. In this way, the material electrical transport properties are typical of thin metallic films. The goal is the realization of electrodes that can sustain repeated large deformations without significant changes in electrical properties. Often is also required a good trade-off between the conductivity and the elastic properties of the nanocomposite: a large amount of nanoparticles reduces the electrical resistance of the nanocomposite at the expense of obtaining a stiffer material with poor mechanical properties.

More interesting functionalities are showed in nanocomposite with electrical properties typical of the transition regime. Innovative memories for computer data storage systems, neuromorphic components, sensors, could be made controlling the filler volume fraction of a nanocomposite.

2.3 Metal-polymer nanocomposite films

The easiest approach to integrate active device components and highly conductive stretchable paths on a soft substrate consists in placing hard materials, components, devices and also circuits on it. There are several techniques that have been developed (Figure 8) to do it. They broadly are dived into two categories: direct integration techniques and lamination techniques [46]. For direct integration with the substrate, component materials are deposited and

patterned layer-by-layer on the soft material, in a similar way to the processes for conventional wafer-based or thin film integrated circuits fabrication. Patterns are formed either by deposition followed by selective removal (subtractively) or by direct printing of patterns (additively). Examples of techniques that fall in this category are: physical [106] and chemical [107] vapor deposition, electroplating [108], electroless plating [109], inkjet printing [110]. On the other hand, in lamination, components or complete circuits are adhered to the substrate with adhesives or by transfer printing. The components are pre-fabricated elsewhere on thin flexible wafers, or thin flexible plastic substrates, or rigid islands. Until now, there is not a universal technique used to fabricate nanocomposites that could be used with all materials and for all applications. The best approach is often chosen according to the type of deformation expected.

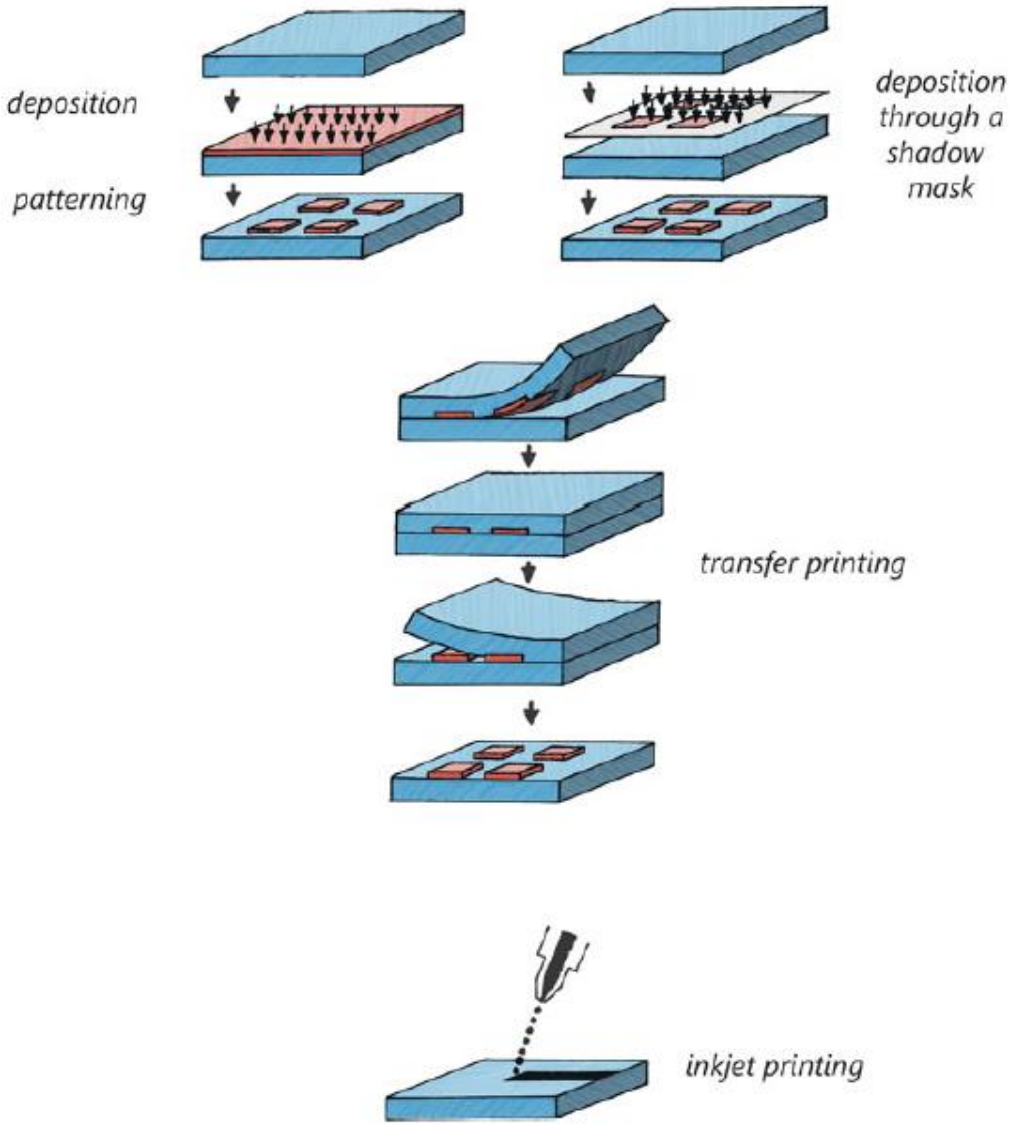

***Figure 8**: Techniques for fabricating devices on elastomeric substrates: deposition followed by lithographic patterning, deposition through a patterned shadow mask, transfer of devices by printing, and additive printing* [46]

We can consider the easiest case represented by bending of a thin flat substrate. In agreement with beam theory, the strain ε experienced by the surface

of a substrate having thickness H and bent to a radius of curvature r, is $\varepsilon = H/(2r)$. Thus, for H = 0.1 mm and r = 10mm, the strain is merely ε = 0.5%. A typical approach used in this case is to fabricate islands of hard materials on a substrate made of the bendable polymer (Figure 9) and to connect the islands with conductive paths made by thin metallic films [13].

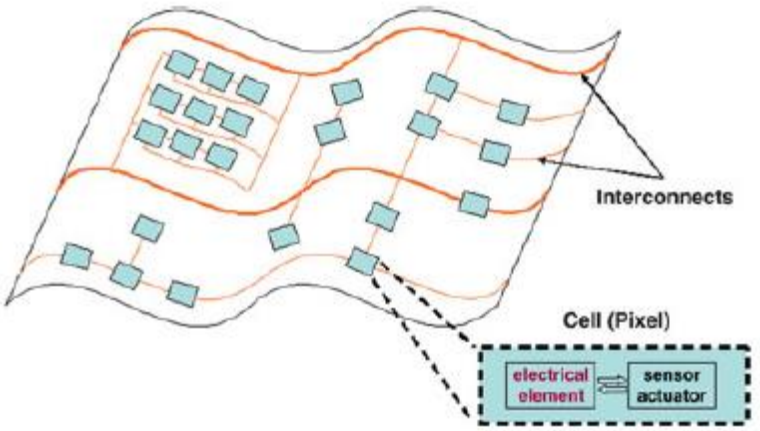

Figure 9*: Architecture of an elastic electronic surface. Cells with electronics functions are made on islands and are connected with flexible conductors on a flexible substrate [46]*

A second step toward a more complex system is considering a uniaxial stretching deformation. In this case, the previous approach is not feasible and it requires several improvements [13]. First of all, the island approach is inappropriate because the hard material can sustain strain as small as few percent, then it cracks and debonds [111]. However, the islands of stiff material can be decoupled from the strain imposed on the substrate by a thin layer of a soft material [112, 113]. This approach allows the system to be stretched up to 20% [114]. Secondly, the conductive interconnections need to be improved as well. Again, using geometrical considerations, it is possible to realize elastic conductors with particular geometries that stand uniaxial deformations (Figure

10): waves, meanders, helices of metal, bridges, spirals of silicon and liquid metal enclosed within microfluidic circuit.

Shifting from a uniaxial deformation-proof system to a biaxial or radial deformation-proof one is a non-trivial task. Most of the workarounds exploited for uniaxial stretching cannot be exploited in this case. For example, meanders and spirals can be stretched only in one direction. The others geometries can be used (Figure 11), though stretchability is highly degraded. In order to address this challenge, it is required a completely new approach that tailors the properties of materials at the nanoscale level. This will be discussed in the next chapters.

The most complex and general system requires withstanding three-dimensional deformations. This case is the least discussed because of its intrinsic complexity, yet it is the most interesting and useful one. In fact, up to now we've been discussed methods to deposit hard materials on soft ones on the same surface. Indeed, actual electronic circuits, including the simplest circuits, have complex multilayer architectures.

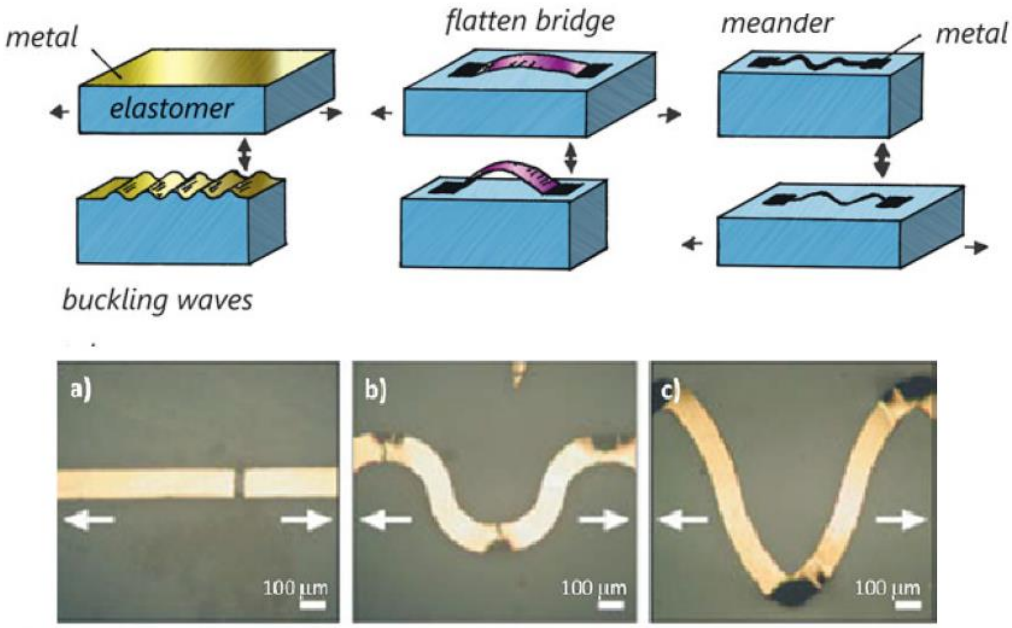

Figure 10*: Techniques for making stretchable conductive path, from top-left: waves, bridges, meander. Bottom: pictures of uni-axial stretchable interconnects [46].*

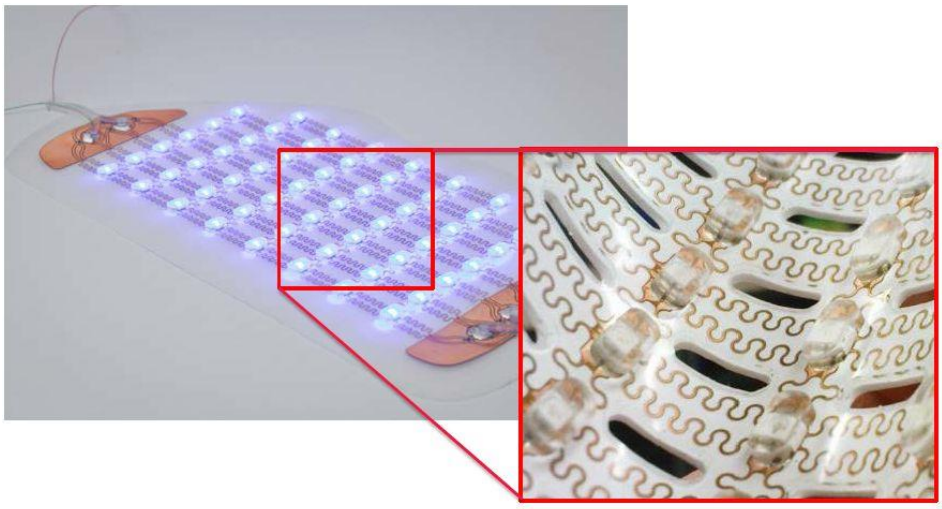

Figure 11: *2D stretchable conductive paths can be obtained arranging one-dimensional solutions. However, it results in degraded stretchability [115]*

The electrical connection among the layers is guaranteed by conductive vias. Being able to fabricate complex three-dimensional multilayer structures mixing hard materials and soft materials that withstand mechanical deformations without experience electrical failure, is demanding for the widespread diffusion of new devices with extensive functionalities based on smart materials. While conductive vias fabrication in classical hard substrates is a simple task, so far few solutions for 3D stretchable system has been proposed, addressing the solution only in case of bendable systems or augmenting architecture complexity, still obtaining poor results [116].

In the next chapter, a novel technique to fabricate metal-polymer nanocomposites, called supersonic cluster beam implantation (SCBI) will be described. Exploiting SCBI, it is possible to fabricate 3D stretchable conductive electrodes, overcoming all the limitations of layered nanocomposites that have been described in this section. Furthermore, SCBI can tailor the electrical and mechanical properties of nanocomposites to shape new materials with novel physical properties that can be exploited in several fields of application.

3 Experimental methods

This chapter aims to describe the main apparatus used for the fabrication and characterization of metal-polymer nanocomposites during this thesis work. First of all, the general working principles of the apparatus will be introduced. Then I will describe the source used to synthetize the metal clusters and I will discuss the improvements introduced during this PhD work to allow the manipulation of several polymeric samples during the same implantation process. Eventually, the characterization setup will be introduced. The majority part of mechanical and electronic components where designed during this work with cad software and fabricated in the laboratory. Stencil masks and sample holders were fabricated with a PowerWasp 3D printers. Several software solutions were developed to automatize and to parallelize the characterization process.

3.1 Supersonic Cluster Beam Implantation

3.1.1 Principle of operations

Supersonic cluster beam implantation (SCBI) is technique for metal-polymer nanocomposites fabrication characterized by high implantation rate, high collimated beam of neutral cluster and large-area implantation. The setup used during this thesis work and illustrated in Figure 12 consists of a pulse microplasma cluster source (PMCS), an aerodynamic focuser, an expansion chamber, an implantation chamber and a system of moving sample holders.

The synthesis process can be described as follows: metallic nanoparticles are produced in the PMCS chamber starting from atoms sputtered by an Argon plasma formed by a high-voltage discharge that erodes the atoms from a metallic rod target. The mixture of clusters and inert gas exit the PMCS through a nozzle toward the expansion chamber as a supersonic beam of electrically neutral clusters. Here the nanoparticles are focused and size-selected through the

aerodynamic focuser and then they expand as a supersonic beam into the expansion chamber kept at the high vacuum pressure of $1x10^{-7}$ Torr through a turbo-molecular pump with a flow rate of 1900 L/s and backed by a roots pump. Then, the beam intercepts the skimmer, a cone with a 2 mm hole in the summit aimed to maintain a differential vacuum between the expansion chamber and the implantation chamber, to preserve the supersonic characteristic of the beam and to further size select the beam. The skimmer connects the expansion chamber with the implantation chamber where the target substrates are stored. Here the clusters beam intercepts the target substrate and the metal nanoparticles enter the polymeric matrix with a soft implantation, without inducing any chemical or physical alteration [89] [67] due to the low kinetic energy (0.5 eV $atom^{-1}$) owned by the clusters. The samples are mounted on a moving sample holder that in combination with stencil masks superimposed on the targets, allows large area implantation and patterning. The implantation chamber is kept at a pressure of $1x10^{-5}$ Torr through a turbo-molecular pump having a flow rate of 520 L/s and backed by the same roots pump used for the expansion chamber. A quartz microbalance is used to measure in real time the implantation parameters, i.e., the thickness of the film deposited and the implantation rate.

Due to the nature of the process, the distribution of the nanoparticles inside the polymer is complex, thus it is impossible to obtain information about the total volume of nanoparticles implanted during the fabrication process. This implies that it is not possible to use the volume filler fraction to describe the nanocomposite properties. Nevertheless, it is essential to gather information about the amount of nanoparticles that constitute the nanocomposite. For this purpose, it is useful to introduce a new quantity named *equivalent thickness*, defined as the thickness of the metal thin film produced by the same amount of clusters and deposited on a rigid substrate placed close to the polymeric sample.

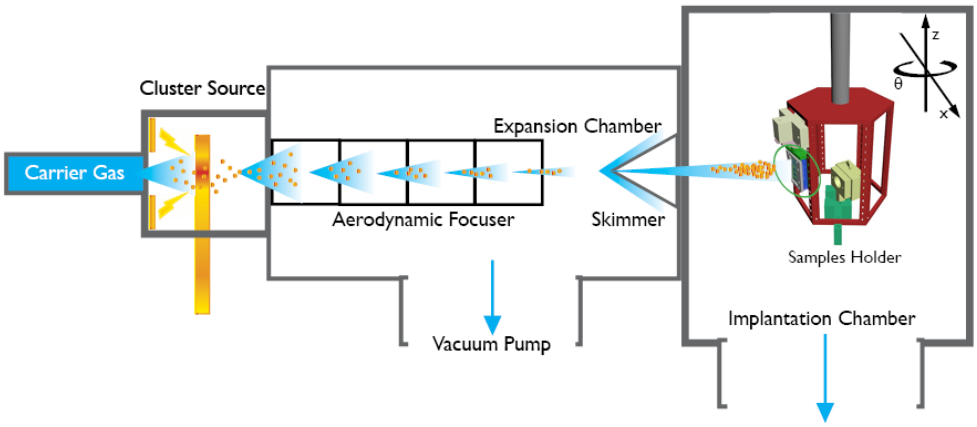

***Figure 12**: Neutral silver nanoparticles are produced in the most left chamber with a pulsed microplasma cluster source (PMCS). The nanoparticles are accelerated toward the next chamber and focalized with an aerodynamic lens system. A skimmer further selects the size of the nanoparticles. The focalized nanoparticles beam enters the last chamber and hit the polymeric target. The nanoparticles implant inside the polymeric matrix*

3.1.2 Pulsed microplasma cluster source (PMCS)

A pulsed microplasma cluster source (PMCS) was used due to its stability in clusters generation and its high throughput. Its working principle can be summarized into three stages: the vaporization of the target material, the clusters-gas mixing with subsequently thermalization of the vaporized material and the extraction of the clusters from the source. One of the major drawbacks using this approach is that the dynamic of the gas strictly depends on the shape of the target material that changes over time due to vaporization process. This leads to fluctuations in the intensity of the beam and in the size of the synthetized clusters [117]. A 3D model of PCMS is sketched in Figure 13. The PMCS source core is

composed by a hollow cylindrical ceramic body. Its entrance is matched with a pulsed valve that injects a burst of Ar at high-pressure (40 bar) inside the source. A copper nozzle is placed between the valve and the ceramic body. The other side is connected to a low conductance nozzle that provides the gateway to the expansion chamber. The target material is provided by a metallic rod placed perpendicularly to the ceramic body axis.

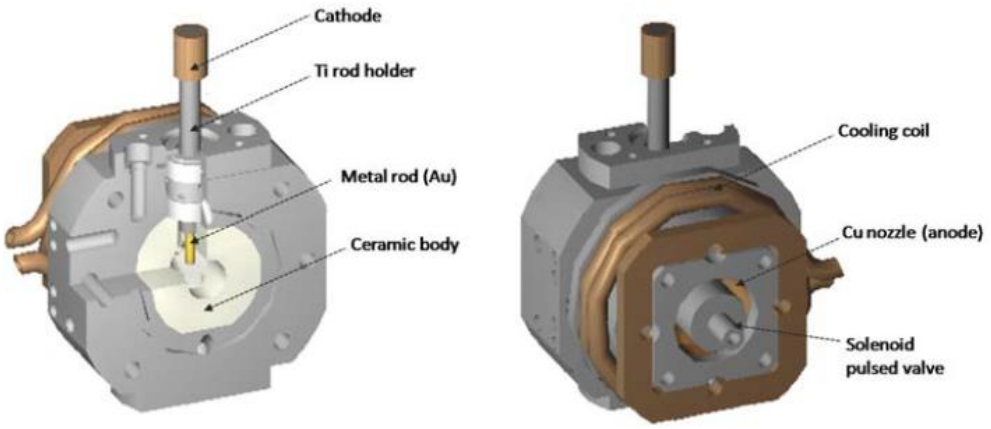

***Figure 13**: From left: front view and back view of the PMCS cluster source. The section on the left shows the inside of the source ceramic body, where ablation and the formation of metal clusters take place. The discharge is applied between the metal rod used (cathode) and the copper plate (anode), having a nozzle through which the gas enters the source. As shown on the right, the copper plate is placed between the solenoid valve and the ceramic body of the source [105]*

The clusters synthesis process can be summarized as follows (Figure 14): initially, the cavity is kept in vacuum (~10^{-4} mbar). Then the valve is opened for 245µs letting the Ar gas flows in. Here, the high-pressure gas creates a high-pressure and density region (smaller than one millimeter) close to the metal rod, for thermodynamic reasons [118]. After a delay of 490 µs since the valve closed,

a voltage of ~750V is applied for 80 µs between the metal rod (cathode) and the copper nozzle (anode). The high potential difference triggers a discharge that leads to the gas ionization. The so produced ions accelerate under the high electric field toward the cathode, forming in this way a plasma plume concentrated in the small high density region, inducing the plasma to erode the rod. In order to allow a uniform sputtering process all along the period while the source is used, the rod is kept rotating by a stepper motor. The erosion of the rod leads to the formation of an oversaturated gas of metal atoms, which condense inside the ceramic body forming metal clusters suspended in the inert gas. Eventually the pressure difference between the source and the expansion chamber drives the cluster-gas mixture through the nozzle to the expansion chamber, and accelerates it to a supersonic-speed up to 1000 m/s [118].

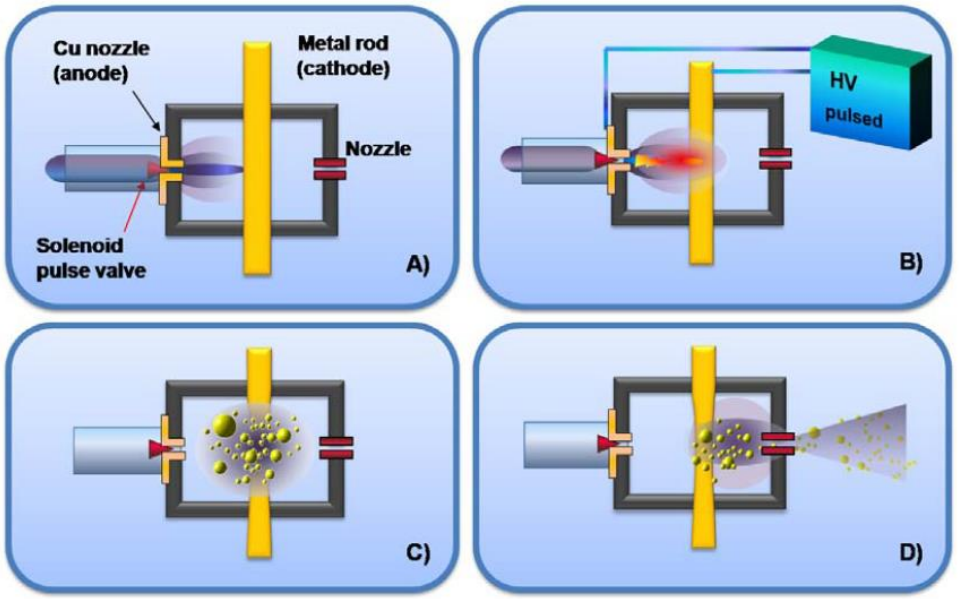

***Figure 14**: Schematic working principle of the Pulsed Microplasma Cluster Source. A) The solenoid valve opens for about 300 microseconds, allowing the entry of Ar gas at 40 bars. B) A voltage of about 750V is applied at the cathode, leading to the ionization of the gas and to the formation of a plasma*

plume able to sputters the metal atoms of the rod. C) The thermalized and ablated metal atoms aggregate to form clusters. D) Due to the pressure difference with the expansion chamber, a supersonic expansion of the cluster-gas mixture is established, leading to the evacuation of the mixture from the source. [105]

3.1.3 The aerodynamic focuser

The beam of neutral metallic nanoparticles entering the implantation chamber has a divergence less than 50 mrad [119] and a clusters size distribution centered around 4 nm [67]. This highly focused beam is obtained through the aerodynamic focuser (Figure 15) that consists of a series of hollow cylinders having an aerodynamic lens at the end. A lens consists of a metal disc with a central hole with a diameter smaller than the internal diameter of the hollow cylinder. The unfocused beam is forced to pass through a series of these hollow cylinders and lens. The sudden change in diameter occurring at the end of every cylinder results in an abrupt change in the direction of flow lines. This leads to a narrowing of the beam diameter and a size-select effect on the mass of the metal clusters [120]. In our setup, I used 4 lenses stages: the firsts 3 lenses have a 2mm hole while the latter has a 1mm hole.

3.1.4 Multi-Samples fabrication and manipulation

During this thesis work, it was developed an automatic system (Figure 16) to monitor and manipulate the samples inside the implantation chamber during the implantation process. Moreover, this system allows the implantation of metal clusters over multiple samples in the same implantation process, speeding up the fabrication of the nanocomposites.

The system, pictured in the Figure 16 is constituted by a main hexagonal samples holder provided with three stepper motors: two of them are dedicated to

move the samples holder along the plane perpendicular to the direction of the cluster beam and the latter is used to rotate it around its z-axis. In the center of the main samples holder there is the quartz microbalance used to measure the thickness of the deposited film. It is mounted over a stepper motor that rotates the microbalance quartz until it is exposed to the beam or removed from it on purpose. Every single side of the hexagonal samples holder could be provided with a smaller sample holder equipped with servomotors that can rotate by 180 degrees with a high angular resolution.

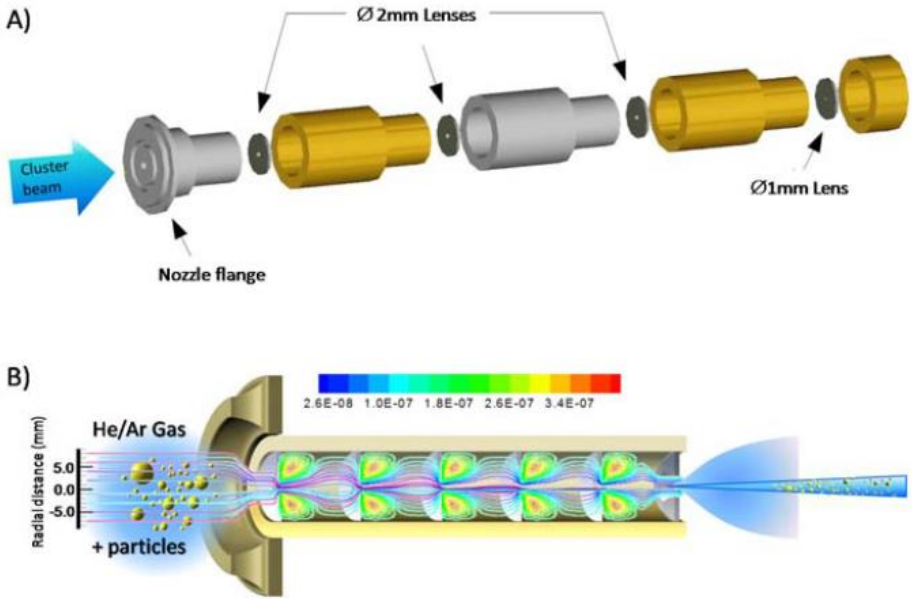

Figure 15: *A) Expanded view of the aerodynamic focuser used in the SCBI apparatus: the three aerodynamic lenses having a diameter of 2 mm and the last with a diameter of 1 mm are visible. The cylinders that form the focuser are made of steel and brass and mounted alternately, in order to avoid the seizing of the threads. B) Schematic representation of the aerodynamic focuser and its working principle. [105]*

A servomotor can rotate the sample by 180 degrees allowing a double face implantation. Moreover, the possibility to continuously change the angle from 0 degree to 180 degrees allows the implantation of metal clusters in 3D structures as will be showed in the chapter sixth chapter. Up to six servomotors could be mounted inside the implantation chambers. Both the servos and the microbalance stepper motor are controlled by a microprocessor (PIC 16F628A) based electronic circuit settled in an adjacent small chamber. The implantation chamber and the electronic circuit chamber are divided by a metal disk provided with electrical vias, to maintain a differential vacuum. The electronic circuit chamber is kept ad a 10^{-2} Torr pressure through a scroll pump. Outside the implantation chamber two webcams are attached to glass flanges used to monitor in real time the implantation process. A Raspberry pi 2 model B computer is used to drive the webcams, the servomotors and the stepper motors. A c++ program was developed to digital add a virtual gunsight to the video showed by the webcams in order to monitor the beam position. The Raspberry pi communicates with the webcams through USB ports while use a Universal Asynchronous Receiver-Transmitter (UART) module to drive the microprocessor that is inside the electronic chamber, through a flange provided with electric vias. All the system is powered with a 5V power supply. A PC is used to control the hexagonal sample holder motors and to acquire the thickness and rate parameters from the microbalance with software developed with LabVIEW. It has also been developed a web server and deployed on the PC to remotely check the implantation parameters through a mobile device. The implantation chamber is provided also with several electrical vias exploited to measure the electrical properties of the nanocomposites during the implantation process. This will be discussed in the next chapter.

Large area implantation is permitted using a raster scanning technique consisting in moving the hexagonal sample holder with its stepper motors system (Figure 16-C) during the implantation process. The virtual gunsight helps also to define the raster scanning path.

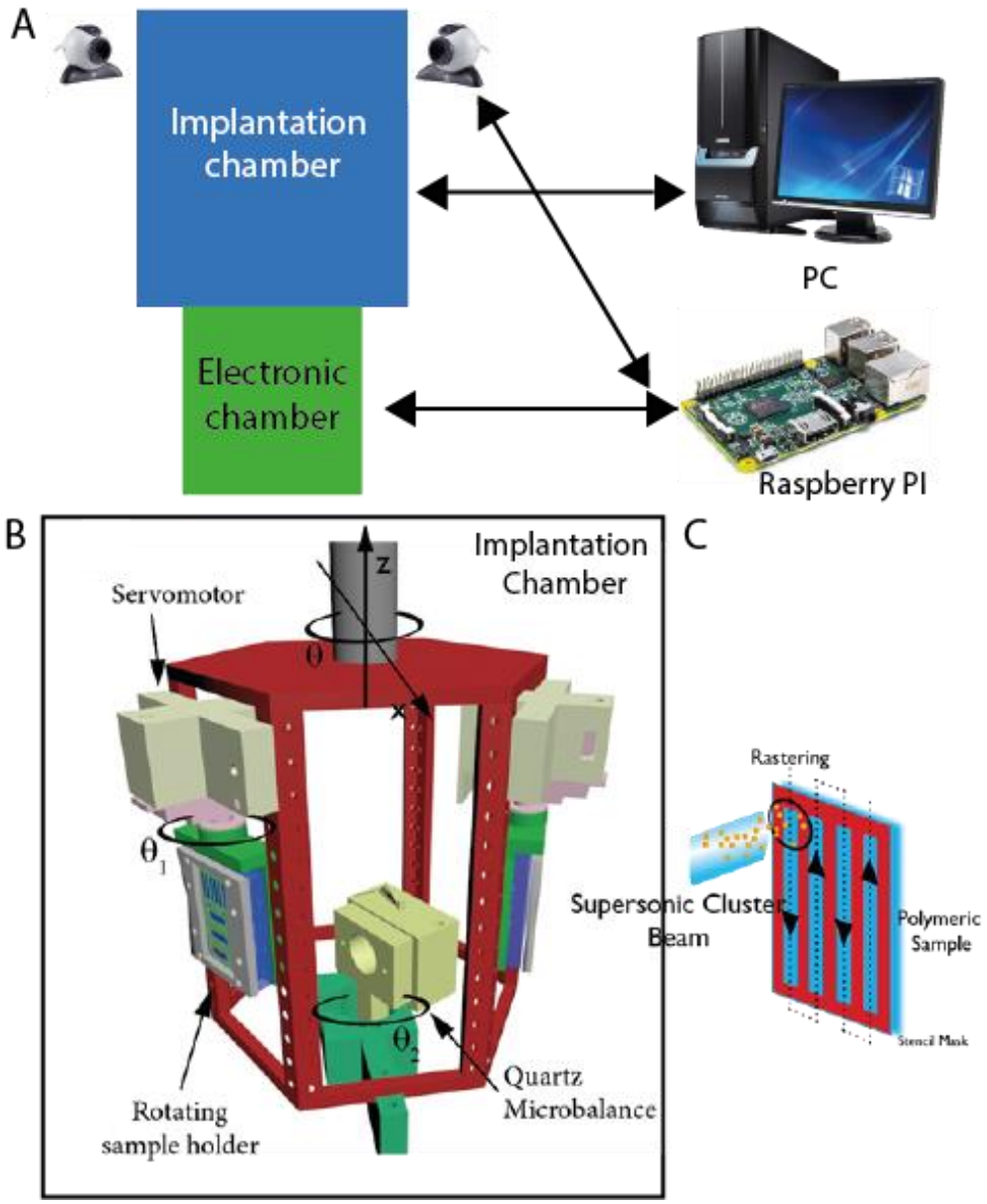

***Figure 16**: A) Controlling system scheme B) 3D model of the rotating sample holder. Several samples can be loaded during the implantation process because of the hexagonal shape of the sample holder. It is provided with two step motors to move the samples along the Z and X axis and one step motor to rotate the sample holder along the Z axis in order to select the sample target. Every side of*

the sample holder can be equipped with a servomotor that is exploited to rotate the samples. It permits to target different sides of the same sample with the nanoparticles beam, within the same implantation process. An electronic board drives all the system and custom software developed during this work. C) The step motors that move the sample holder are exploited to implant nanoparticles on large area samples (raster scanning) or on specimens with complex geometries. They are driven by custom software developed with LabView, purposely for this thesis

3.2 Electrical characterization

3.2.1 Percolation

The setup developed to characterize the evolution of the nanocomposite electrical properties during the implantation process is hereafter described (Figure 17). The samples and electrodes geometries are adapted on a case by case basis. A sample of the polymer substrate having length L, width W and thicknesses T is prepared and framed to a sample holder in the implantation chamber. Two conductive electrodes having length L_{el}, width W_{el} and spaced by a distance d are deposited onto the substrate with the assistance of a stencil mask.

The equivalent thickness of the electrodes is chosen to guarantee an Ohmic conduction. Usually this is achieved using an equivalent thickness greater than 100nm for rigid or flexible substrate and an equivalent thickness greater than 150nm for soft substrate. Here, a second stencil mask, provided with two conductive electrodes made of copper conductive tape, is superimposed on the two deposited electrodes. The stencil mask is designed to allow the clusters implantation between the two electrodes, partially overlapping on them.

The copper tape electrodes are hard wired to an external electronic circuit through electrical feedthroughs. The electronic circuit supports up to eight channels to characterize several samples at the same time. It is constituted by an Arduino board that controls up to eight relays. Every single relay is connected to an Agilent 34410A multimeter used to measure the samples electrical resistance as a function of the time. LabVIEW software running on a PC was developed to select a particular channel of the electronic circuit turning on the corresponding relay and acquire the resistance signal during the implantation process from the Agilent multimeter.

The Agilent multimeter and the electronic circuit are connected to the PC through USB channels. A schematic of the whole system implemented is showed in Figure 18.

A typical electrical characterization trial is showed in Figure 18 and it is described as follows: few samples are arranged on a vertical column, having the conductive electrodes to the side, and framed to a sample holder. One electrode for every sample is short circuit to ground. The other is connected to a channel in the electronic switch. The raster scanning path for the implantation is defined along the vertical column and is chosen to be 4 cm wider (2 cm for side) than the area occupied by the samples in order to obtain a homogenous implantation. The evolution of electrical resistance for every sample is recorded during the implantation process.

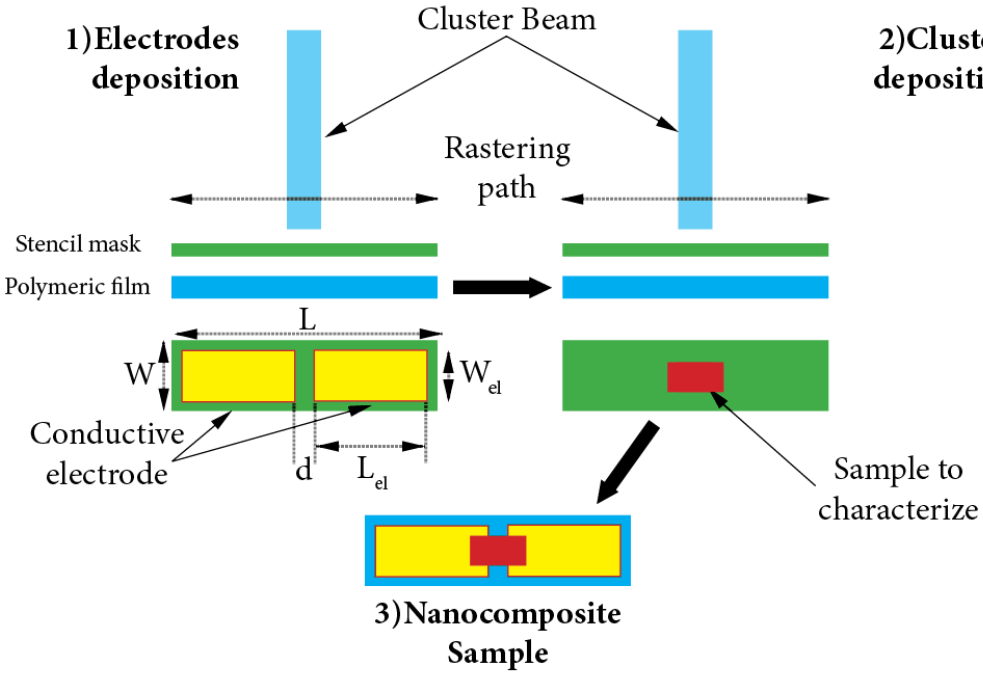

Figure 17: Scheme of the steps required to prepare a nanocomposite sample for percolation measurements: first two conductive electrodes are made implanting a large amount of nanoparticles (usually Teq > 100). The electrodes are separated by a small gap. These electrodes are used as a base to contact the nanocomposite with a multimeter. Then the gap is filled with nanoparticles, while a multimeter record the change in resistance of the gap.

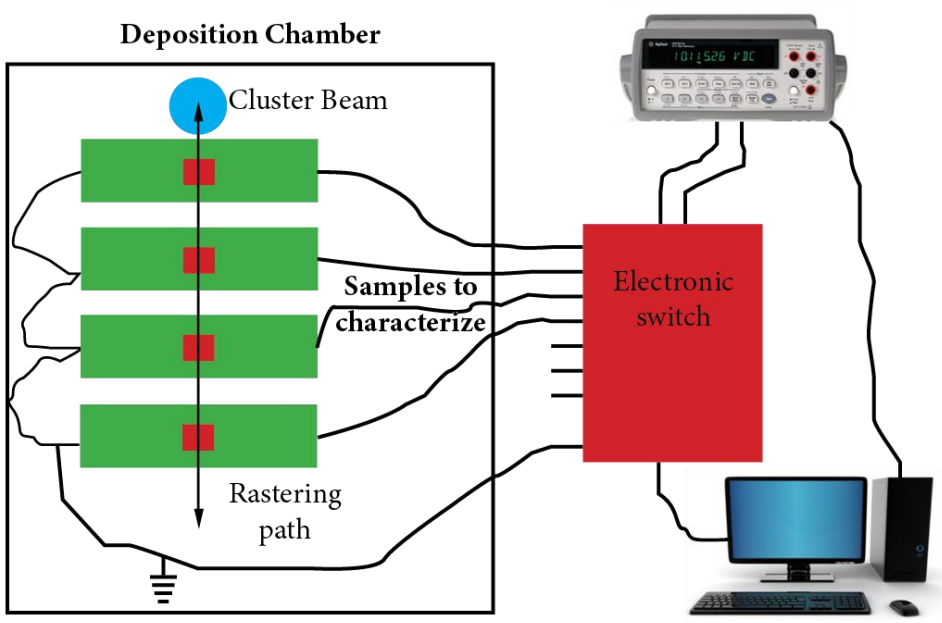

***Figure 18**: Schematic view of the setup used to characterize the electrical properties evolution of several nanocomposites at the same time. The samples are organized as showed and the implanted electrodes of every sample are connected with an electronic switch placed outside the implantation chamber and connected with a multimeter. Custom software developed on purpose during this work, select one channel at a time, bridging the multimeter with one of the several samples inside the implantation chamber. During the implantation process (usually with raster scanning to cover all the samples surface), the electronic switch switches between channels. Software developed on purpose with LabView records all the data about the resistance values measured by the multimeter.*

3.2.2 Polymeric thin film breakdown

Circular polymeric thin films having radius of 2.5 cm are prepared and tested for dielectric breakdown. A flat metal plate is used as a ground electrode.

The thin films are laid down on the ground electrode. A rounded metal electrode acting as the active electrode is arranged above the thin film (Figure 19).

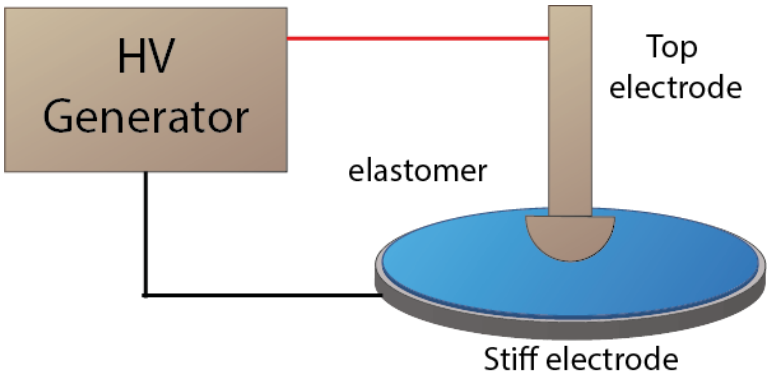

Figure 19*: Breakdown test set up: the polymeric thin film is eased down on a flat stiff electrode. A rounded electrode is superimposed on the top surface of the substrate. A high voltage generator applies a voltage ramp with increasing tension values up to the breakdown limit value [11].*

A voltage ramp is applied and the voltage is increased until electrical breakdown takes place. The electrical breakdown occurs when the voltage power supply experienced a sudden decrease in the voltage supplied because of the high amount of current instantaneously flew into the sample.

3.2.3 Electrical resistance

The resistance of conductive electrodes deposited onto polymeric substrate is measured using an Agilent 34410A multimeter with two-points methods.

3.3 Electro-mechanical characterization

The mechanical properties and electrical properties under stress conditions of thin polymeric or metal-polymer nanocomposites samples are characterized at the same time by performing uniaxial stress test with a slit

connected to a force gauge model that measured the force applied during the elongation performed with a set-up described elsewhere [121]. The samples are clamped along the shortest ends with two clamps provided with conductive copper tape wired to a model multimeter that record the electrical resistance. Then, they are elongated along the longest dimension at a constant rate (50 μs s^{-1}) while measuring the resultant elongation. At the same time, the nanocomposite electrical resistance is recorded.

3.4 Structural and morphology characterization

3.4.1 Thin films thickness

Polymeric thin films thickness is measured using a non-contact optical profilometer (Leica DCM 3D, Leica Microsystems, Germany) on polymer strips on PDMS strips peeled off from Si substrate prior to the implantation and recollected onto a clean Si wafer.

3.4.2 Equivalent thickness

The amount of nanoparticles deposited on a soft substrate is measured in term of equivalent thickness (t_{eq}), defined as previously said as the thickness of a metallic film simultaneously deposited onto a rigid substrate during the implantation process. For this purpose, a partially masked Si wafer is placed close to the polymeric sample. Then the mask is removed and the step between the masked (bare Si) and unmasked (metallic film) area is measured using a P-6 stylus profilometer (KLA Tencor USA).

3.4.3 Surface morphology

SEM images of the surface and of the cross section of polymeric thin film are obtained with a Helios NanoLab 600i Dual Beam SEM instrument (FEI, USA). In order to obtain the cross-section images, a protective 1 μm Pt layer is deposited (FIB-assisted deposition) over the area before the milling process.

3.5 Actuation

The performances of the actuators were characterized in pure shear configuration with an isotonic test [11] on freestanding actuators clamped along the shortest side and with applied uniaxial pre-strain (Figure 20). The electromechanical transduction of the actuators was investigated by recording the responses of the actuators to different step voltages with a digital optical microscope. Videos and images of the samples during the experiments were recorded with a uEye UI-2250-MM CCD camera (Imaging Development Systems, Obersulm, Germany) equipped with a Zoom 6000 zoom lens (Navitar, Rochester, NY). A graph paper placed next to the actuator is used as a reference system. Elongation along the axial direction upon electrical activation was measured by processing videos and images of the activated samples with respect the graph paper. The tests were performed for different pre-stretching values, applying some weights to the sample.

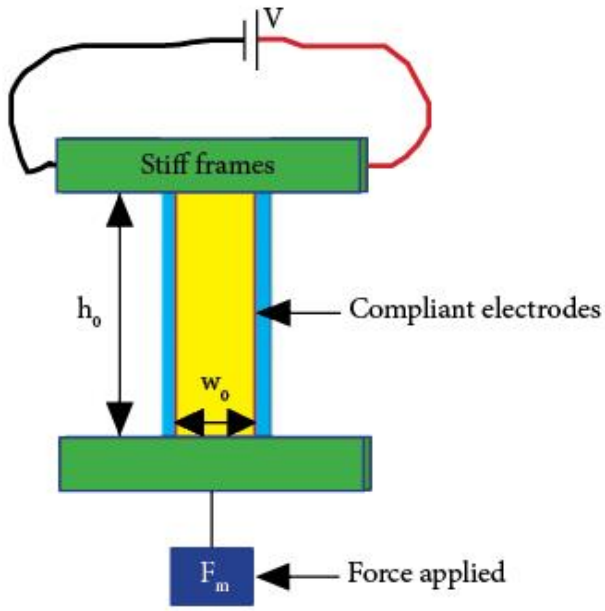

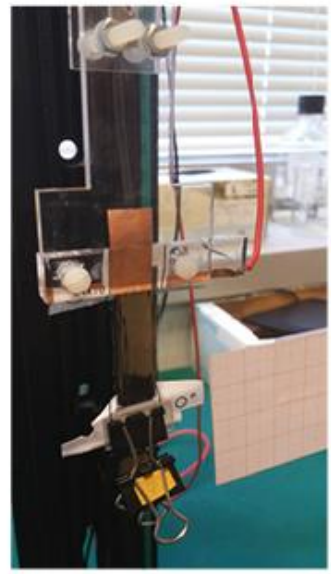

***Figure 20**: Set-up for actuation characterization of polymeric thin film in pure shear configuration: the actuator is framed between two rigid frames and suspended. The sample is pre-stretched applying some weight to the actuator. A graph paper placed next to the actuator is used as a reference system. A camera records the elongation.*

4 Soft actuators

4.1 Introduction

Electro-active polymers (EAPs) are polymers that respond mechanically to electrical stimulation. They show large strains when subjected to electric field or current. These materials are very attractive because they can be exploited to mimic the movements of living beings to make bioinspired mechanisms. In fact, they can be configured into any shape and their properties can be tailored to suit a broad range of requirements. Moreover, they can also be used as sensors or power generators if a change in their shape induce a variation in their electrical properties. EAPs are divided into two groups [122]: field-activated and ionic EAPs. A field-activated EAP is typical composed by a thin polymeric film sandwiched by two conductive electrodes. When a voltage is applied between the two electrodes, the Coulomb interaction produced by the electric field created tends to squeeze the polymer along the electric field direction (Maxwell stress) that results in a stretching along the plane perpendicular to the electric field (Figure 21). On the contrary, ionic EAPs are made by an electrolyte between two electrodes. The actuation mechanism relies on ions drifting or diffusion.

This work has dealt with field-activate EAPs that use elastomeric polymers as the active component (dielectric elastomer actuators, or DEAs). The reasons behind this choice are that first of all DEAs are very responsive ($<10^{-3}$ s) because the actuation does not involve diffusion of charge. They can store a large amount of mechanical energy and also they can be made to hold the induced displacement without consuming electrical energy. The major drawback is that they require a high activation field, typical 100V/μm or more, which may be close to the electric breakdown level. This means that high voltage values (1kV~10kV) are required to drive a DEA. It can be avoided using micrometric layers of polymers in a stack configuration, to generate high field with low voltage.

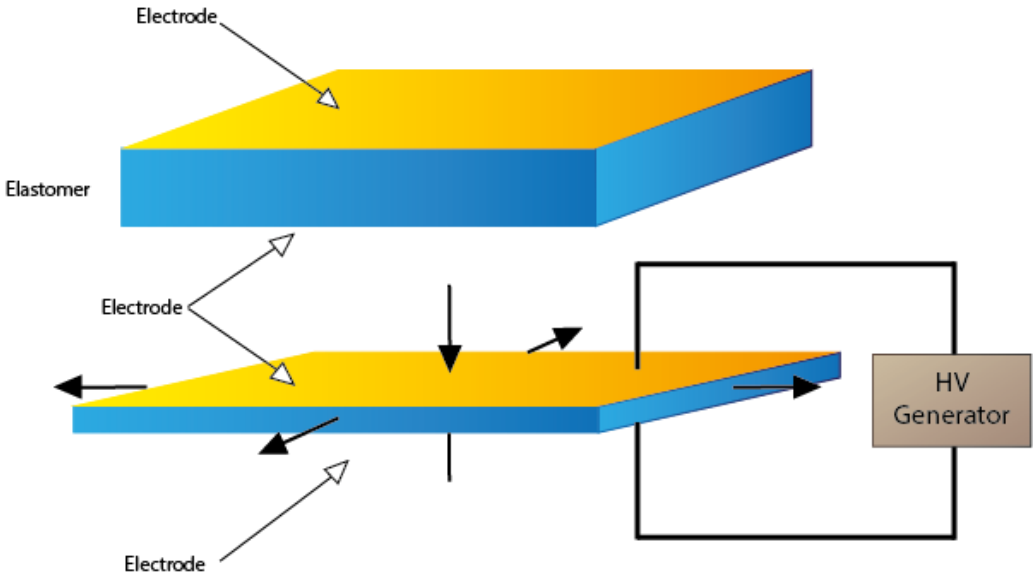

Figure 21: *A typical DEA is composed by an elastomer sandwiched between two compliant conductive electrodes. When a potential is applied between, the electrodes, the Maxwell stress exert a compressive force along the electric field direction, squeezing the polymer. In turn, this results in an expansion of the polymer along the plane perpendicular to the electric field*

The electrodes of a DEA are at the core of the actuator performance: they must sustain repeated large deformations (millions of cycles) while remain conductive [83]. At the same time, electrodes must not increase the polymer stiffness to preserve its mechanical properties. Several approaches have been used to fabricate compliant electrodes on polymer surface: carbon electrodes, metallic thin-film electrodes, single-walled carbon nanotubes electrodes, ion implanted electrodes [83]. But these techniques are not compatible with miniaturization because the low maximum lateral resolution achievable, because the poor adhesion to the substrate or because of the increase caused in elastomer stiffness that is dramatic for micrometric thin polymer films [83].

4.2 Soft actuators using SCBI

SCBI is an effective method to fabricate compliant conductive electrodes on a polymer surface [88] [105]. The low energy owned by the clusters allows a soft implantation in the polymeric matrix avoiding charging and carbonization phenomena. This is crucial to preserve the substrate mechanical properties [89]. In this chapter, the physical characterization of actuators based on silver-poly(dimethyl-siloxane) (Ag/PDMS) with SCBI will be presented.

4.2.1 Basic properties of PDMS

Poly(dimethyl-siloxane) (PDMS) is one of the most versatile biocompatible silicon elastomers used as matrix for metal/polymers nanocomposites. Its physical properties, its competitive cost and the possibility to be processed with standard microfabrication and molding techniques, make him a perfect candidate for several applications, including stretchable electronics, microfluidic and biomedical devices, prostheses and so on.

PDMS has a repeated Si-O bonds structure linked to CH_3 functional groups as showed in Figure 22. It is possible to obtain PDMS in fluid, gel or elastomer state changing the degree of crosslinking, without altering the chemical composition. The PDMS chains can arrange themselves in a crystalline and in an amorphous form. The two types of structures usually co-exist within the same polymeric sample and their ratio influences its stiffness. PDMS is stiffer when the crystalline form prevails over the amorphous one. The phase's ratio strongly depends by the temperature: an increase in the temperature causes an increase of the amorphous state.

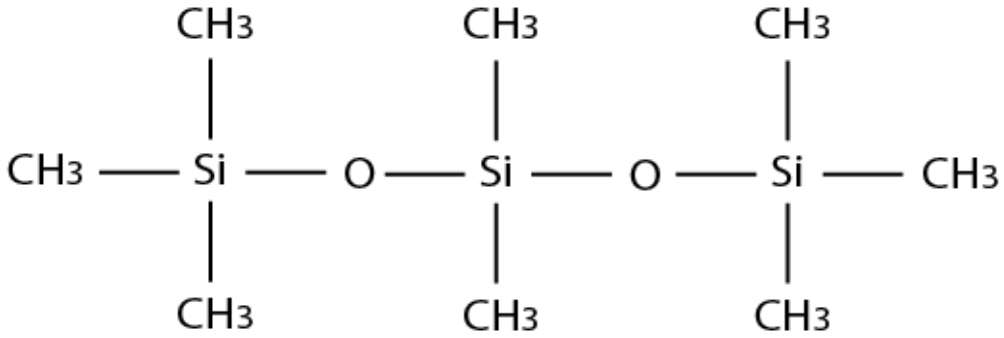

Figure 22: Two-dimensional structure of a short chain of PDMS

PDMS has a critical temperature value named the glass transition. The glass transition (-130°C) indicates the transition point where the chains that are unable to move (below the critical point), gain a great mobility and become able to slide between each other (above the critical point).

PDMS is highly hydrophobic forming more than 100 degrees contact angle with water drops or organic solvents [123]. Anyway, an oxygen plasma treatment makes the PDMS hydrophilic for a short amount of time. PDMS also resists to several chemical solvents [123] but the absorption of most of them causes the PDMS to swell [124]. PDMS has good insulator behavior, withstanding electric fields from 250 to 635 kV mm^{-1} depending on electrodes shape and geometry [125].

From these perspectives, it is clear why PDMS can be exploited as the structural constituent of DEAs.

4.2.2 Low-voltage driven soft actuators via Ag implanted nanocomposite stretchable electrodes

Draft to be submitted to: Advanced Materials

1.1.1 Low-voltage driven soft actuators via Ag implanted nanocomposite stretchable electrodes

Authors: Andrea Bellacicca (1), Silvia Taccola (2), Paolo Milani (1), Lucia Beccai (2), Francesco Greco (2),

(1) Università Degli Studi Di Milano, Department of Physics, Milano, Italy

(2) Istituto Italiano Di Tecnologia, Center For Micro-BioRobotics, Pontedera, Italy

Introduction

In the last years, dielectric elastomer actuators (DEAs) have attracted increasing interest as soft and lightweight electromechanical transducers for the fabrication of smart actuators, strain sensors, soft robots, haptic interfaces, and energy harvesting systems [REF1-6]. DEAs are based on thin electrically insulating elastomeric films sandwiched between two compliant electrodes. When a voltage is applied to the electrodes, the electrostatic pressure acting on the film squeezes the elastomer in thickness and, as the elastomer is incompressible, it consequently deforms in-plane or out-of plane depending on the design. In order to enable the widespread use of DEAs and their integration in devices, a number of key technological challenges have yet to be solved: operation at low voltage, miniaturization, large-scale manufacturability, stable operation, reliability and fabrication of optimized compliant electrodes.

As regards electrodes, ideally they would be highly conductive, perfectly compliant and would adhere well to the soft elastomer; at the same time, electrodes should not affect significantly the elastomer stiffness and they should be able to sustain repeated deformations (millions of cycles) while retaining their integrity and electrical properties. An exhaustive review on electrode materials for DE transducers was recently proposed by Rosset and Shea [REF7]. Traditional carbon-based electrodes such as carbon grease or carbon powder, although their low stiffness and ability to remain conductive at large strains, show many limitations in terms of miniaturization, patternability, and compatibility with clean-room processes [REF7,8]. Thin film metal electrodes deposited by sputtering or evaporation are not intrinsically stretchable beyond a few percent strain, show poor adhesion onto elastomers,

deterioration (i.e. cracking), and delamination after few deformation cycles [REF7]. Recently, many research groups have worked towards developing new types of compliant electrodes for DEAs, in order to overcome the aforementioned limitations. To this aim, two different implantation methods have been presented in the literature: Filtered Cathodic Vacuum Arc (FCVA) metal ion implantation [REF9,10] and Supersonic Cluster Beam Implantation (SCBI) [REF11-14]. Implantation methods lead to the formation of metal–polymer nanocomposite with metal nanoclusters embedded into the elastomeric matrix, forming a conductive layer below the substrate surface. As implantation dose increases, the individual metallic clusters contact each other (thus providing a percolative conducting path); nevertheless, the absence of a strong bond between clusters allows their relative displacement upon the application of stretching to the elastomeric matrix, thus forming an electrode with a high degree of compliance. Moreover, because they are partially buried inside the elastomer matrix, the adhesion of these electrodes is excellent. In particular, SCBI approach consists in directing a highly collimated beam of neutral metal clusters accelerated in a supersonic expansion towards a polymeric substrate, with the advantages of avoiding any charging or carbonization of the polymeric substrate and being fully compatible with stencil mask micropatterning and liftoff technology [REF11]. Recently, stretchable patterned Au-PDMS nanocomposites able to withstand very large deformation while preserving finite and reproducible electrical resistance were fabricated by SCBI of neutral Au nanoparticles in PDMS through stencil masks [REF14]. At the same time, SCBI paves the way to engineer a priori the elastic properties of the polymeric substrate by finely tuning the amount of implanted NPs. In fact, it has been experimentally demonstrated that the mechanical properties of the metal/polymer nanocomposite can be maintained close to that of the bare polymer for significant metal volume concentration [REF14]]. Furthermore, the elastic properties of the nanocomposites only depend by the amount, the concentration and the aspect-ratio of the metallic NPs fillers and not on the physical and chemical modification of the polymeric matrix.

The other essential component of a DEA is the elastomer. Silicone elastomers are one of the most suitable and promising materials for DEAs due to their superior properties such as high efficiency, reliability, reproducible actuation and fast response times upon activation [REF15]. Moreover, silicones show little ageing effects, chemical and humidity inertness, and can be operated at a wide temperature range (from -100 to 260°C). On the other hand, silicone elastomers have a relatively low dielectric permittivity when compared with acrylic elastomers. Nevertheless, they have the advantage of a lower viscoelasticity than acrylics, indicating that they can be operated at higher frequencies with lower losses and less heat generation. In this regard, the approaches in order to maximize the attained actuation strain of a DEA are by reducing the thickness of the elastomeric membrane, reducing the elastomer mechanical stiffness, and/or increasing the elastomer permittivity.

In this work, we present dielectric elastomer actuators based on thin films of polydimethylsiloxane (PDMS) by the use of silver compliant electrodes fabricated by Supersonic Cluster Beam Implantation.

Experimental Section

Fabrication of PDMS/Ag actuators

PDMS thin films: silicon wafers (400 μm thick, p-type, boron doped, <100>, Si-Mat Silicon Materials) were silanized by placing them in a desiccator for 30 min along with a vial that contained a few drops of silanizing agent (chlorotrimethylsilane, Sigma–Aldrich). PDMS thin films were prepared by mixing the pre-polymer solution and curing agent (Sylgard 184, Dow Corning Corp.) in a 10:1 ratio (w/w), and then degassing the mixture in a vacuum desiccator for 20 minutes to remove air bubbles. The mixture was then spin coated onto the silanized silicon wafers for 30 s at a speed of 5000 rpm and cured at T = 80 °C for 60 min in an oven. PDMS thin films were then cut with a razor blade, submerged in ethanol and peeled off from the Si substrate.

Electrodes Fabrication: conductive electrodes were realized onto the freestanding PDMS thin films exploiting the Supersonic Cluster Beam Implantation (SCBI) apparatus equipped with a Pulsed Microplasma Cluster Source (PMCS). PMCS consists in a ceramic body with a cavity in which a silver rod target is vaporized by a localized electrical discharge supported by a pulsed injection of an inert gas (Ar) at high-pressure (40 bar). The sputtered silver atoms aggregate in the source cavity forming metal nanoparticles. The mixture of nanoparticles and inert gas expands through a nozzle toward the next chamber (expansion chamber) forming a supersonic beam of neutral clusters. The clusters are focused through a system of aerodynamic lens resulting in highly collimated beam with divergence lower than 1° and with a kinetic energy of approximately 0.5 eV·atom-1. The beam is further size selected passing through a skimmer that connects the expansion chamber with a second chamber (deposition chamber) where the polymeric film is held by a sample holder. Finally, the beam intercepts the polymeric targets. A set of stepper motors moves the samples to allow a homogenous deposition of metallic clusters all over the surface using a raster scanning process. In order to implant silver nanoparticles on both sides

of the PDMS samples in a single implantation process we developed and realized a motorized samples holder with 3D printing technology able to rotate the polymeric target. The conductive paths were patterned onto the target by means of two stencil masks combined with substrate raster scanning. In a single implantation process, we were able to produce up to 4 rectangular shaped PDMS/Ag actuators with dimensions of 14 × 50 mm and a centered implanted area of 10 × 34 mm on both sides.

Morphology of PDMS and Actuators

PDMS thin films thickness was measured by using a non-contact optical profilometer (Leica DCM 3D, Leica Microsystems, Germany) on PDMS strips peeled off from Si substrate prior to the implantation and recollected onto a clean Si wafer. The amount of nanoparticles implanted was measured in term of equivalent thickness (t_{eq}), defined as the thickness of a Ag film simultaneously deposited onto a rigid substrate (partially masked Si wafer) during the implantation process. Then the mask was removed and the step between the masked (bare Si) and unmasked (Ag film) area was measured using a P-6 stylus profilometer (KLA Tencor, USA).

SEM images of the surface and of the cross section (52° tilted view) were obtained with a Helios NanoLab 600i Dual Beam FIB/SEM instrument (FEI, USA). In order to obtain the cross-section images, a protective 1 μm Pt layer was deposited (FIB-assisted deposition) over the area before the milling process.

Force Microscope (AFM) imaging were performed using a Veeco Innova Scanning Probe Microscope (Veeco Instruments Inc., Santa Barbara, CA) operating in tapping mode, with a RTESPA Al coated silicon probe (Veeco Instruments Inc.).

PDMS and actuators mechanical and electro-mechanical characterization

The mechanical and electro-mechanical properties of 3 PDMS thin films samples and 3 PDMS/Ag actuators samples were characterized by performing uniaxial tensile test. Stress/strain measurements and electrical resistance variation of PDMS/Ag actuators during the stretching were performed with up to a 20% applied strain using a custom dedicated set-up described elsewhere. [REF16] Both the PDMS thin films and actuators were clamped at the shortest ends and elongated perpendicularly at a constant rate (50 μm s^{-1}) while measuring the resultant elongation. Each mechanical test was repeated ten times in order to take into account the stretch-induced softening called Mullins effect [REF17].

PDMS dielectric strength

PDMS circular samples, with a diameter of 2.5 cm, were placed down on a flat metal plate, used as the ground electrode. The active electrode is a rounded metal electrode, polished and free from irregularities. The active electrode rests on top of the sample, ensuring contact but limiting the compression in order to avoid alteration of film thickness. The PDMS dielectric strength was characterized by applying to a PDMS thin film a voltage ramp, increasing the tension value until electrical breakdown occurs, as detected by a sudden raise of current, which usually causes the voltage to drop down

Electromechanical transduction

The performances of the actuators were characterized in pure shear configuration with an isotonic test on freestanding actuators clamped along the shortest side and with applied uniaxial pre-strain. Actuators were tested with different applied uniaxial load (1.36, 2.39, 3.65, and 4.91 g) and the corresponding pre-strain were measured by images analysis. The electromechanical transduction of the actuators was investigated by recording the responses of the actuators to different step voltages with a

digital optical microscope (applied voltages: 411, 511, 614, 715, and 765 V). The voltage is applied for fifteen seconds, in order to allow the sample to reach its maximum strain. Videos and images of the samples during the experiments were recorded with a uEye UI-2250-MM CCD camera (Imaging Development Systems, Obersulm, Germany) equipped with a Zoom 6000 zoom lens (Navitar, Rochester, NY). A graph paper placed next to the actuator was used as reference system. Elongation along the axial direction upon electrical activation was measured by processing videos and images of the activated samples.

Lifetime of DET

The lifetime of the actuator was assessed repeating the isotonic test in pure shear configuration applying a uniaxial load of 4.91g and a voltage of 765V for ten thousand cycles and measuring the maximum actuation strain every thousand cycles. Measurements were performed using the same setup described in the electromechanical transduction measurements section.

Results and discussion

Morphology of PDMS and Actuators

One of the main scopes of this study was to prepare and test thin film DEAs verifying the hypothesis that SCBI can provide sufficiently compliant electrodes to work onto very thin silicone films. While decreasing the thickness of DEA is envisioned as one of the main strategies for permitting their actuation at low applied voltage, from a practical point of view the use of very thin elastomeric films in fact limit this approach, because of the relevant difficulties in film preparation, manipulation, processing and in building up of more complex and robust DEAs. These practical challenges can be faced by using appropriate and *ad hoc* release and manipulation techniques. PDMS thin films are very fragile and easily tend to fold on it because of electrostatic forces. To avoid these issues, PDMS thin films were released from silanized Si substrate after immersion in ethanol. Due to the silanization of the silicon wafers, the PDMS structures could be easily peeled off from the substrate and the resulting free-standing films could be gently manipulated in ethanol with metal tweezers and transferred and dried onto a clean silicon wafer for thickness measurements or onto the stencil masks for implantation. The prepared PDMS thin films had a thickness of 17 ± 0.8 μm.

Supersonic Cluster Beam Implantation (SCBI), described in details in the Experimental Section, is illustrated in Figure 1.A.B.C. For each actuator, the implantation process required around half an hour. The equivalent thickness of implanted Ag electrodes, defined as the thickness of an Ag film simultaneously deposited onto a rigid substrate (partially masked Si wafer) during the implantation process, was measured as 103 ± 7 nm.

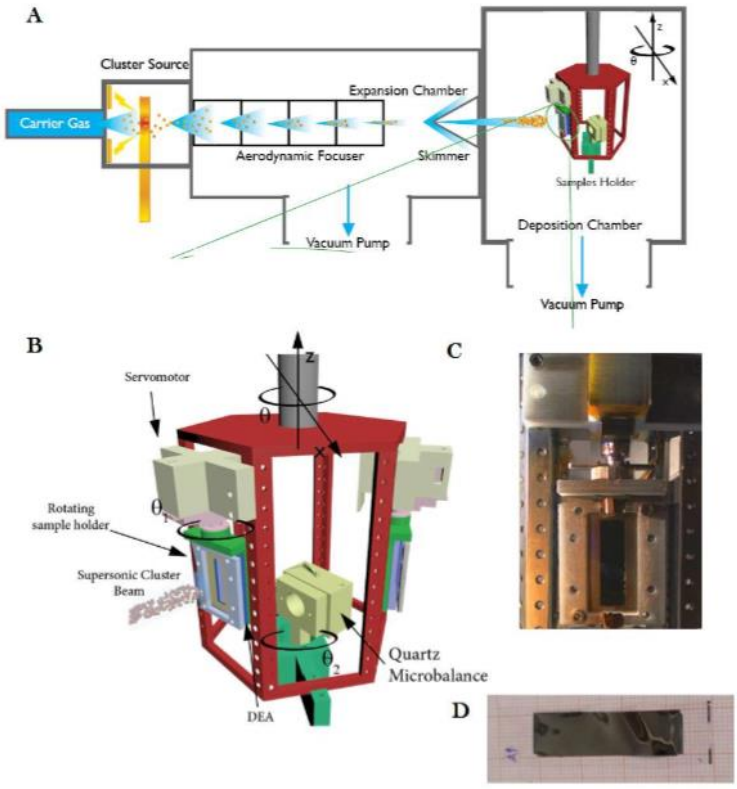

***Figure 1**:A) Schematic view of the SCBI apparatus B) 3D model of the rotating sample holder. Several samples can be loaded during the implantation process because of the hexagonal shape of the sample holder. It is provided with two step motors to move the samples along the Z and X axis and one step motor to rotate the sample holder along the Z axis in order to select the sample target. Every side of the sample holder can be equipped with a servomotor that is exploited to rotate the samples and implant both sides of the sample within the same process. C) A picture of an actuator loaded on the rotating sample holder. D) An actuator with implanted silver electrodes.*

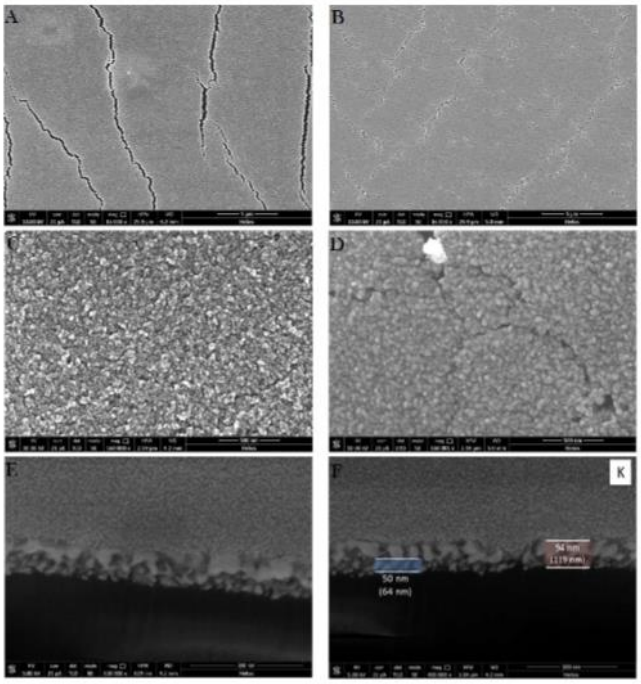

***Figure 2**: A-B) SEM images of the SCBI-implanted electrodes surface before and after the actuations. The surface of the actuator after actuation shows a higher number of cracks. C-D) The Ag clusters of the electrode surface are bigger in D picture (after actuation) than in the C picture (before actuation). This could be caused by the reorganization that nanoparticles undergo during actuation* [REF11]. *E-F) Ag/PDMS cross section: the electrode shows a two-layered structure with different morphologies: the top layer is made by large clusters and it has an estimated height of 55 nm. The bottom layer is composed by smaller nanoparticles implanted in the PDMS matrix and it has an estimated height of 64 nm. The height values in parenthesis are obtained measuring the layer height directly from the picture and applying to them the correction due to the tilted view.*

The surface of the SCBI-implanted electrodes was investigated with SEM and AFM to verify the successful implantation and assess their integrity and topography. Figure 2 shows the scanning electron microscopy (SEM) images of Ag/PDMS electrode surface before (Figure 2.A-C-E) and after (Figure 2.B-D-F) actuation. First of all, it is possible to notice that the electrode surface after actuation (Figure 2.B) shows a higher number of cracks than the electrode surface before actuation (Figure 2.A), but in both cases, the surface is still electrically conductive. Figure 2.C shows that the surface of the Ag electrode before actuation is composed by Ag clusters smaller than the clusters of the electrode surface after actuations (Figure 2.D). This is due to the reorganization that Ag clusters undergo during the actuation [REF11].

Inspection of the implanted portion of the electrodes is not possible with surface microscopy techniques (SEM and AFM) as the implanted portion is covered with a granular film made up of individual Ag clusters and practically forming a "skin". Nevertheless, the implanted portion clearly emerges in SEM images of an Ag/Pdms electrode cross section (Figure 2.E-F). It is possible to distinguish a bottom and a top ("skin") layer with different morphologies within the electrode. The bottom layer is principally composed by small nanoparticles implanted in the PDMS matrix and has an estimated height of 64 nm. The top layer is made by bigger nanoparticle clusters deposited onto the polymeric matrix with denser arrangement and has an estimated height of 55 nm.

Mechanical Properties

Reducing the thickness of the membranes is an effective strategy to decrease the voltage needed to actuate DEAs. Though the thinner the membrane, the higher the stiffening effect because the impact of the electrodes becomes more dominant [REF7]. These requirements set strict limitations to the available electrode fabrication processes when working on thin polymer films. Thus, SCBI was envisioned as a feasible electrode fabrication process, as it is a finely tunable process, known to not

dramatically alter the mechanical properties of implanted surfaces [REF 14] To verify this hypothesis we characterized the mechanical properties of double-sided electrodes, Ag/PDMS/Ag, obtained with SCBI by evaluating their stress-strain behavior.

The nominal stress VS nominal strain plot for bare PDMS and double-sided Ag/PDMS electrodes are compared (Figure 3.A). Nominal strain is defined as

$$Sm = (L - L_0)/L_0,$$

where Sm is the nominal strain, L is the length of the film and L_0 is the initial length of the film.

The nominal stress is defined as

$$Tm = Fm/A_0,$$

where Tm is the nominal stress, Fm is the force applied and A_0 is the initial cross-section of the film.

The Young's modulus is identified as the slope of the linear portion (purely elastic behavior) in a stress vs strain curve.

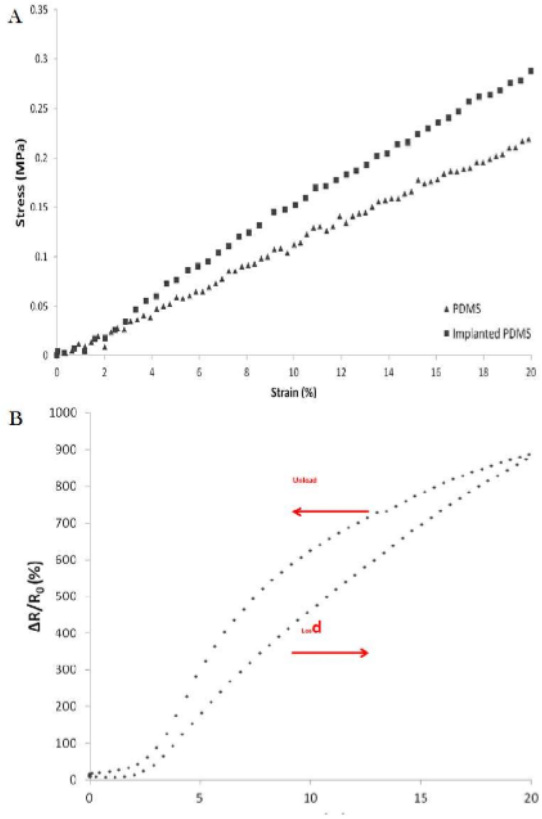

Figure 3: A) Stress-strain plot comparison between a pristine PDMS specimen and an Ag/PDMS actuators. The actuator has a Young's modulus only 25% larger than the bare PDMS Young's modulus. B) Resistance variation as a function of strain for an Ag/PDMS actuator. The initial resistance value is recovered when the stress is removed.

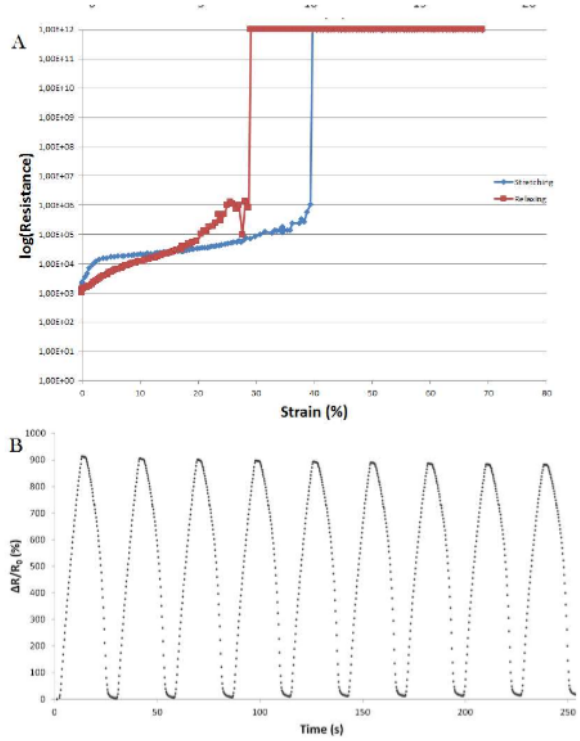

Figure 4: A) Large values of strain cause a temporary open circuit, that is fully recovered when the stress is removed. B) The electrodes electrical properties are constant within different stretching cycles

Notably, the Ag/PDMS/Ag samples retained a linear elastic behavior over the full range of strain; moreover, they had a Young's modulus of 1.41±0.09 MPa, that is, only 25% larger than the bare PDMS Young's modulus (1.13±0.11 MPa), thus proving that the electrodes don't significantly increase

the stiffness of the elastomer. This remarkable result is mostly due to the implantation process (low energy involved ~0.5 eV/atom) that avoids carbonization or others chemical modification of the substrate surface, as observed in other deposition/implantation techniques.

PDMS thin films electrical properties

Maximum strain attainable by an actuator is limited by the electrical breakdown strength of the polymer. When the voltage limit is reached, a conductive path is created causing a sudden increase in the current that flows within the polymer. This electrical discharge causes permanent damages to the actuator, breaking it. Thus, is crucial to characterize the ultimate limit voltage that the thin elastomeric film can sustain without it suffers from physical damages. The breakdown voltage value strongly depends by the polymer inhomogeneities caused by differences both in film thickness or density along the thin films, or by the presence of defects, for example micrometric air bubbles. These factors make the actual breakdown voltage value heterogeneous within the same film. We report an inferior value for the electrical breakdown attested around 1.7 kV.

Electrodes

Stretchable conductive electrodes able to sustain large deformations without loss in conductivity or mechanical integrity are essential for DEAs. Moreover, the possibility to link the electrical properties of the electrodes to the deformation applied in a reproducible fashion can enable those applications that require to sense the mechanical status of DEAs, e.g. by a resistive measurement along electrode. Common processes involved in electrodes fabrication exploit conductive greases or metal deposition technique but neither are truly effective for DEAs made of micrometric elastomer films [REF7].

SCBI-implanted Ag/PDMS electrodes were tested to assess how their electrical resistance changed as a function of the PDMS strain (Figure 3.B). The initial resistance of tested samples (same equivalent thickness) was found to be 622 ± 162 Ω. All the samples showed an analogous resistance variation during the strain cycle imposed (0 – 20 - 0%), recovering their initial value when the strain is released. This is true also for bigger strain (up to 70%) that induce a temporary open circuit above a threshold strain value (4.C). This can be explained because of the nanocomposite nature of the Ag/PDMS thin film. In fact, the electrical conduction is due to the percolation paths across the metal nanoparticles. During the elongation, the mean distance between the nanoparticles increase leading to a resistance increase and eventually resulting in an open circuit. Nevertheless, when strain is released the percolating paths are restored and the electric conductivity is fully recovered [REF11]. In 4.B it is showed how the electrodes electrical properties are constant within different stretching cycles assuring the actuator will behave uniformly during actuation.

Actuation Tests

One of the typical demonstration experiments for the dielectric elastomer actuators is the isotonic test in a pure-shear configuration. Samples for pure shear testing were prepared by fixing rigid clamps to the edges of the free-standing Ag/PDMS/Ag DEA prepared in form of stripes and fixed at one side. Planar electrical contacts were realized at the fixed edge through copper tape on the rigid clamps. During the isotonic test the DEA is vertically suspended and a load is suspended from the free end of the actuator; the voltage is increased causing the actuator to stretch. The sample geometry and our notation are presented in Fig. 5.a. The geometry of electrodes on actuators surface was chosen in order to avoid electrical discharge between the two sides through air. For this reason, a free area of not-implanted PDMS was left at the edges of actuators

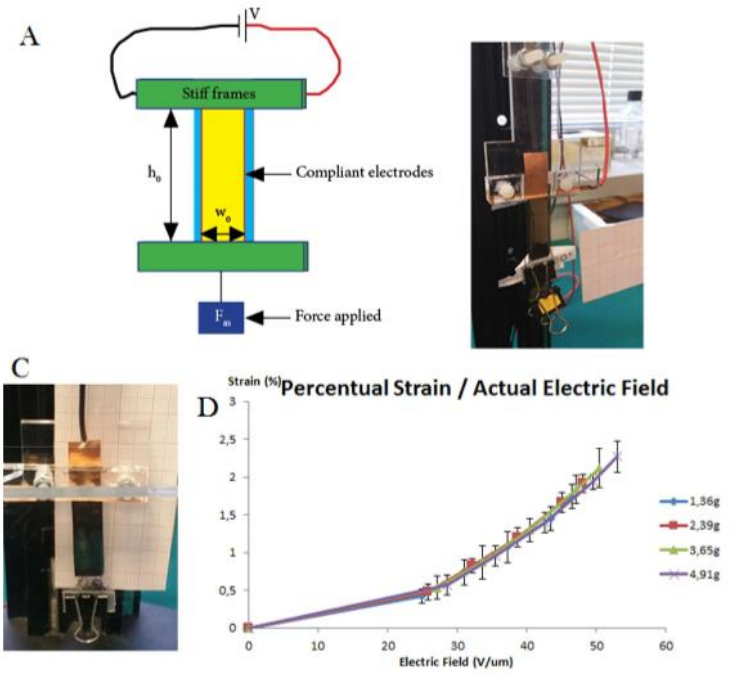

Figure 5: A) Schematic of the actuation test set up for an isotonic test in a pure-shear configuration. w_0 is the electrode width; h_0 is the electrode height. B-C) Pictures of the set-up used. D) The actuation behavior of the tested actuators is uniform for different pre-stretching values

As reported in the experimental section, actuators were tested with different applied uniaxial load, and the resulting electrical strains at different step voltages were recorded using a digital camera.

The electrical strain S_e, measured by processing the images collected upon electrical driving, was defined as:

$$S_e = (x_e - x_0) / x_0$$

with x_e, x_0 the length under electrical activation and at rest (no electrical activation) along x axis (vertical direction, Fig. 4.a.b.c), respectively.

The principal stretch ratios α_x, α_y, α_d are calculated from:

$\alpha_x = x_e / x_0$; $\alpha_y = y_e / y_0$; $\alpha_d = d_e / d_0$,

with $y_{e,0}$ and $d_{e,0}$ the corresponding lengths along y (horizontal direction) and z (thickness of the actuator), respectively.

The assumption that the elastomer is incompressible [126] and isotropic gives rise to the constraint that

$\alpha_x \alpha_y \alpha_d = 1$

If we assume that the width of the actuator is fixed because the stretching in the width (y axis) is negligible with respect to the stretching along the length (x axis), therefore

$\alpha_y = 1$

$\alpha_x = 1/ \alpha_d$

$x_e / x_0 = d_0 / d_e$

$d_e = d_0 x_0 / x_e$.

In this way it is possible to take into account the intrinsic decrease in thickness ("squeezing") associated with elongation along the plane of the actuator.

This allows for a calculation of the true electric field E_t:

$Et = V/d_e = V x_e / d_0 x_0$,

These equations enable simple analyses, under the assumption that the stress, strain and applied electric fields are uniform throughout the specimen (REF18).

As described in the Experimental Section, actuators were tested with different applied uniaxial load (1.36, 2.39, 3.65, and 4.91 g). The corresponding pre-strain, measured by images analysis, was respectively 3.33 ± 0.6 %, 7.03 ± 1.21 %, 12.1 ± 1.25% and 18.0 ± 1.67%.

Figure 5.d reports the measured electrical strain S_e versus the true electrical field E_t. As expected, all the actuators showed a quadratic elongation as a function of the electric field (and hence of the applied voltage).

Lifetime of DEA

From the point of view of industrial application, assessing DEAs lifetime is crucial to define how the repeated mechanical deformations influence and degrade DEAs performances. In fact, reiterated electrically induced stretching and relaxing cycles can lead to electrodes loss in conductivity, due to delamination or breaks. Moreover, DEAs are usually operated near the electrical breakdown limit, thus a long-term stability characterization is required. It has already been proved that SCBI technique is an effective fabrication process to realize compliant gold electrodes on PDMS with long life-time [REF11, REF12, REF14]. As showed in 6, the actuator tested showed an initial degradation in maximum strain attainable reaching its lowest value around cycle 6000 (around 28% of the initial value). After that, the maximum strain achievable remains stable to that value. The initial degradation can be explained as follow: the electrical induced strain drives a reorganization in the metallic clusters network structure [REF11], that, in turn, cause a change in the electrical properties of the Ag/PDMS nanocomposite. The new network structure tends to be less sensitive to mechanical deformation at every cycle, reaching a better stability after few thousand cycles.

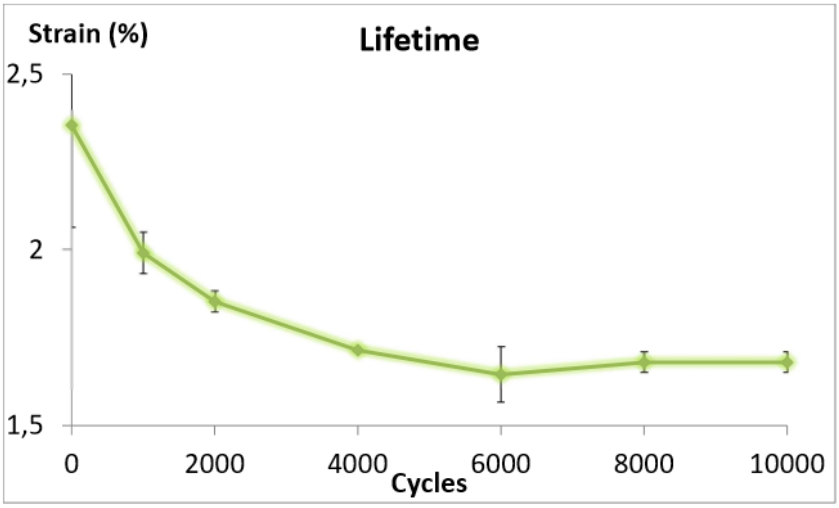

Figure 6: The actuator performance as a function of the actuation cycle. The initial degradation and subsequently stabilization can be explained considering the initial reorganization of the network constituted by metallic clusters within the polymer matrix. After few thousand cycles network structure tends to be less sensitive to mechanical deformation

Conclusions

We have developed a protocol to manipulate micrometric PDMS thin (17μm) films, characterizing their mechanical and electrical properties. We fabricated micrometric Ag/PDMS DEAs exploiting SCBI and we characterized their mechanical and electrical properties. The low energy owned by the clusters permits a soft implantation inside the polymeric matrix without damaging it. In fact, comparing the results from pristine PDMS mechanical characterization with DEAs results we have observed a small increment (30%) in the Young's modulus. The electrical characterization of DEAs electrodes under mechanical stress, showed that electrodes could easily sustain large stretching deformations maintaining good electrical properties also for repeated stress strain cycles. During the actuations tests, we have observed an electrically induced strain up to 2.5%. This value stabilized to 1.7% after ten thousand actuation cycles, demonstrating the reliability of the electrodes. Therefore,

SCBI is an effective technique that can be exploited to fabricate long-life compliant electrodes for micrometric thin DEAs, preserving the polymer mechanical properties.

References

[REF1] Federico Carpi, Siegfried Bauer, Danilo De Rossi, "Stretching Dielectric Elastomer Performance", SCIENCE VOL 330, Issue 6012, 24 DECEMBER 2010.

[REF2] Federico Carpi, Danilo De Rossi, Roy Kornbluh, Ronald Edward Pelrine, Peter Sommer-Larsen, "Dielectric Elastomers as Electromechanical Transducers: Fundamentals, Materials, Devices, Models and Applications of an Emerging Electroactive Polymer Technology", Elsevier, 2011.

[REF3] Brochu, P. and Pei, Q. (2010),"Advances in Dielectric Elastomers for Actuators and Artificial Muscles". Macromol. Rapid Commun., 31: 10–36. doi: 10.1002/marc.200900425

[REF4] Biggs et al "Electroactive Polymers: Developments of and Perspectives for Dielectric Elastomers", Angew. Chem. Int. Ed., 52: 9409–9421. doi:10.1002/anie.201301918.

[REF5] I. A. Anderson, T. A. Gisby, T. G. McKay, B. M. O'Brien, and E. P. Calius, "Multi-functional dielectric elastomer artificial muscles for soft and smart machines", J. Appl. Phys. 112, 041101 (2012).

[REF6] Roy D. Kornbluh, Ron Pelrine, Harsha Prahlad, Annjoe Wong-Foy, Brian McCoy, Susan Kim, Joseph Eckerle and Tom Low (2012). Dielectric elastomers: Stretching the capabilities of energy harvesting. MRS Bulletin, 37, pp 246-253.

[REF7] Samuel Rosset, Herbert R. Shea, Appl Phys A (2013) 110:281–307.

[REF8] Federico Carpi, Piero Chiarelli, Alberto Mazzoldi, and Danilo De Rossi. A: Physical, 107(1):85–95, 2003.

[REF9] S. Rosset, M. Niklaus, P. Dubois, and H. R. Shea, Adv. Funct. Mater. 19, 470 (2009).

[REF10] M. Niklaus and H. R. Shea, Acta Mater. 59, 830–840 (2011).

[REF11] G. Corbelli, C. Ghisleri, M. Marelli, P. Milani, and L. Ravagnan, Adv. Mater. 23, 4504 (2011).

[REF12] C. Ghisleri, F. Borghi, L. Ravagnan, A. Podesta, C. Melis, L. Colombo, and P. Milani, J. Phys. D: Appl. Phys. 47, 015301 (2014).

[REF13] M. Marelli, G. Divitini, C. Collini, L. Ravagnan, G. Corbelli, C. Ghisleri, A. Gianfelice, C. Lenardi, P. Milani, and L. Lorenzelli, J. Micromech. Microeng. 21, 045013 (2011).

[REF14] F. Borghi, C. Melis, C. Ghisleri, A. Podestà, L. Ravagnan, L. Colombo, and P. Milani, Applied Physics Letters 106, 121902 (2015); doi: 10.1063/1.4916350.

[REF15] Frederikke B. Madsen, Anders E. Daugaard, Søren Hvilsted, Anne L. Skov, "The Current State of Silicone-Based Dielectric Elastomer Transducers", Macromol. Rapid Commun. 2016, DOI: 10.1002/marc.201500576.

[REF16] F. Greco, V. Domenici, A. Desii, E. Sinibaldi, B. Zupančič, B. Zalar, B. Mazzolai, V. Mattoli, Soft Matter 2013, 9, 11405.
[REF17] F. Carpi, I. Anderson, S. Bauer, G. Frediani, G. Gallone, M. Gei, C. Graaf, C. Jean-Mistral, W. Kaal, G. Kofod, M. Kollosche, R. Kornbluh, B. Lassen, M. Matysek, S. Michel, S. Nowak, B. O'Brien, Q. Pei, R. Pelrine, B. Rechenbach, S. Rosset and H. Shea, Smart Materials and Structure, vol. 24, no. 10, p. 105025, 2015.
[REF18] I. Krakovsky´,a) T. Romijn, and A. Posthuma de Boer , JOURNAL OF APPLIED PHYSICS vol.85, no 1, p 628 1999

4.3 Conclusions

SCBI has been used to fabricate compliant electrode on 17 μm thick PDMS based soft actuators. The mechanical characterization of these actuators shows that there is a little increase in stiffness due to the metal electrodes, with respect to the pristine polymer. The electrodes are able to sustain large deformations preserving good conductivity, restoring also the initial resistivity when the deformation is removed. The micrometric actuator thickness assures that lower voltage values (< 1kV) are needed to observe actuation. The actuation was characterized for several pre-strains. An actuator has been subjected to ten thousand voltage-driven stretch-relax cycles to demonstrate that the electrodes can sustain repeated large deformations remaining conductive. All the samples fabricated have similar mechanical, electrical and actuation characteristics. The good physical properties showed by the actuators demonstrates that SCBI is a promising technique for the fabrication of DEAs with well-defined physical characteristics, overcoming all the issues related with the fabrication of compliant electrodes that are typical observed when other techniques are used.

5 Paper Electronics

5.1 Introduction

Standard electronic components can be divided in two types: passive and active. Passive components include conductive wires, resistor, capacitors, inductors and antennas. Transistors, diodes, memories and batteries are active components. Several fast and low-cost printing techniques have been developed to fabricate both passive and active electronic components on paper [40]: flexographic printing, gravure printing, offset printing and screen printing. All these techniques rely on conductive liquid inks deposited on the paper substrate. These inks contain nanoparticles made by conductive or semi-conductive materials. The ink is adsorbed by the paper resulting in a homogeneous printed film. Nevertheless, adsorption is considered a big disadvantage [40], because the paper fibers are hygroscopic and swell during the printing process. This, combined with capillarity, greatly reduces the maximum resolution achievable. Furthermore, the inks contain many different components, such as solvents, pigments, binder and additives. The choice of the solvents and the ink concentration is limited by the electronic component that is being printed. Binders and additives worsen the electrical performances.

Here I present electronic components printed on paper with solvent-free conductive ink (dry ink) made by gold nanoparticles produced with supersonic cluster beam deposition (SBCD) apparatus. Conductive paths, resistors and capacitors have been printed on paper. Resistors and capacitors have been printed in order to realize low-pass and high-pass RC filters. Ionic liquid has been incorporated between two planar conductive electrodes made of gold and carbon to obtain super capacitors that have been exploited to fabricate a wireless rechargeable device to store high quantity of power. These super capacitors have been used to power a temperature sensor.

5.2 Supersonic cluster beam deposition to print electronic components on paper

5.2.1 High-throughput shadow mask printing of passive electrical components on paper by supersonic cluster beam deposition

APPLIED PHYSICS LETTERS **108**, 163501 (2016)

High-throughput shadow mask printing of passive electrical components on paper by supersonic cluster beam deposition

Francesco Caruso, Andrea Bellacicca, and Paolo Milani[a)]
CIMaINa and Dipartimento di Fisica, Università degli Studi di Milano, Via Celoria 16, 20133 Milano, Italy

(Received 16 February 2016; accepted 8 April 2016; published online 20 April 2016)

We report the rapid prototyping of passive electrical components (resistors and capacitors) on plain paper by an additive and parallel technology consisting of supersonic cluster beam deposition (SCBD) coupled with shadow mask printing. Cluster-assembled films have a growth mechanism substantially different from that of atom-assembled ones providing the possibility of a fine tuning of their electrical conduction properties around the percolative conduction threshold. Exploiting the precise control on cluster beam intensity and shape typical of SCBD, we produced, in a one-step process, batches of resistors with resistance values spanning a range of two orders of magnitude. Parallel plate capacitors with paper as the dielectric medium were also produced with capacitance in the range of tens of picofarads. Compared to standard deposition technologies, SCBD allows for a very efficient use of raw materials and the rapid production of components with different shape and dimensions while controlling independently the electrical characteristics. Discrete electrical components produced by SCBD are very robust against deformation and bending, and they can be easily assembled to build circuits with desired characteristics. The availability of large batches of these components enables the rapid and cheap prototyping and integration of electrical components on paper as building blocks of more complex systems. *Published by AIP Publishing.*
[http://dx.doi.org/10.1063/1.4947281]

The fabrication of electronic circuits and microfluidic devices on paper is considered a very promising solution for the realization of low-cost disposable analytical devices and biodegradable green electronics.[1–3] Recently, the interest for the use of paper as a substrate for foldable electronic components such as antennas and actuators has substantially increased in view of the realization of the so-called origami electronics,[4,5] self-foldable kirigami soft robots,[6] and power portable emergency locator transmitters based on origami microbial fuel cells.[3]

These applications rely on the so-called "chip-on-flex technologies" where electronic components have typical dimension of tens or hundreds of microns so miniaturization is not a critical issue.[1] In this case, substrates must be flexible and foldable, and manufacturing methods should be cheap, easily scalable, compatible with rapid prototyping in order to produce batches of components to be integrated in functional systems.[1,2]

The use of paper as a substrate is thus very effective for the fabrication of flexible and foldable electronic circuits. Its low cost and availability is ideal for rapid prototyping, it can be easily shaped and trimmed with scissors or cutters, and it can be used for complex self-standing 3D structures, fluidics, and electrochemical applications.[3–7]

Printing on paper relies on a technological tradition dating back from almost two thousand years and originating from China; it became a mass-producing technology in Europe from the fifteenth century.[7] The direct printing of electronic components with various degrees of complexity on paper has taken inspiration from this tradition, and it is based on techniques such as flexography, offset, and screen printing.[7] The fabrication of elements such as transistors,[8] solar cells,[9] and diodes; and devices such as displays, Radio-Frequency IDentification (RFID) tags, and sensors is highly demanding in terms of the characteristics of the substrate. For a large number of applications plastic-covered paper is used and traditional solid-state circuital elements are glued on paper substrates.[7] The printing of passive circuital elements on plain paper, such as resistors and capacitors, is less demanding; however, chip-on-flex and soft robotics technologies require the production of large batches of components to be subsequently assembled in 2D or 3D configurations, with different electrical and geometrical characteristics.[1,6,10]

Among different approaches, ink-jet printing is considered a technique of choice for the printing of simple electronic circuits on paper with the use of conductive inks and for the fabrication of passive and active elements.[11] The use of ink-jet printing is limited by the availability of conducting inks with suitable properties (surface tension, viscosity) able to match the roughness, porosity, and wettability of the paper substrates; moreover, the post-printing ink drying process is difficult to control, and it can lead to unwanted variations of the electrical properties of the components.[7]

An alternative to the use of liquid inks has been developed in the last decade consisting in the direct writing with gas-phase coating techniques where an atomic vapor or nanoparticles dispersed in a carrier gas are deposited directly or through a shadow mask.[12] Direct writing from the gas phase is a low-cost and high-throughput technology suitable also for 3D substrates;[13] its widespread application is, however, hampered by the lack of acceptable adhesiveness on the substrate and electrical conductivity of the deposited species.[14]

[a)]Author to whom correspondence should be addressed. Electronic mail: pmilani@mi.infn.it

In general, traditional printing techniques have only a partial control on the amount of deposited conductive material; hence, as in the case of resistors, the value for the resistance is determined only by the length and the lateral dimension of the printed trace.

In the case of capacitors, the literature reports about interdigitated capacitors printed on plastic foils or photographic paper in a narrow range of low-capacitance values.[7] The use of paper as dielectric layer between two printed metallic layers is an alternative solution as the rolling of metallized paper foils into cylinders is widespread for the fabrication of standard capacitors; however, no reports about this fabrication strategy are available.

We have demonstrated that the use of intense and highly collimated neutral nanoparticle beams produced in a supersonic expansion is an enabling tool for the large-scale integration of nanoparticles and nanostructured films on microfabricated platforms and smart nanocomposites.[15–17] In particular, we have shown that this approach called supersonic cluster beam deposition (SCBD) can be efficiently used for the fabrication of electrically conductive patterned structures and devices on a wide variety of substrates, including polymers.[18,19]

Here we present the rapid and reproducible parallel fabrication of sets of resistors and capacitors on paper by using SCBD and a shadow mask. Our approach relies on the fact that the electrical properties of cluster-assembled films grown from the gas phase evolve in a significantly different way compared to atom-assembled films.[20] In particular, in the percolative regime, electrical conduction can be precisely controlled by SCBD,[21] thus allowing the tuning of the resistance while keeping constant the dimensions of the resistors and optimizing the use of raw material.

Figure 1(a) shows a schematic representation of the SCBD deposition apparatus equipped with a Pulsed Microplasma Cluster Source (PMCS).[22] A PMCS consists in a ceramic body with a cavity where a metallic target (Au in the present case) is sputtered by a localized electrical discharge ignited during the pulsed injection of Ar gas at high pressure (40 bar). The sputtered metal atoms from the target thermalize with the carrier gas and aggregate in the cavity forming metal clusters. The carrier gas-cluster mixture expands out of the PMCS through a nozzle into a low pressure (10^{-6} mbar) expansion chamber (Fig. 1(a)). The supersonic expansion originating from the high pressure difference between the PMCS and the expansion chamber results in highly collimated supersonic beam: a divergence lower than 1° is obtained by using aerodynamic focusing nozzles.[22]

The central part of the cluster beam enters a second vacuum chamber (deposition chamber, at a pressure of about 10^{-5} mbar), and it impinges on the shadow mask-substrate paper system supported by a motorized substrate holder. During deposition, the holder displaces the mask and the substrate in the vertical direction orthogonal to the cluster beam axis (Fig. 1(b)). Since the cluster density distribution in the beam is bell-shaped (as characterized in detail in Ref. 23), this results in a homogeneous metallization in the direction parallel to the raster with a gradient in the dose of nanoparticle in the direction perpendicular to the raster. This allows the one-step fabrication of components with different resistances in a controlled range of values. As a substrate, we used commercial plain white paper for ink-jet and laser printer (Xerox Digital, 75 g/m^2, roughness: 170 ml/min) and the shadow mask was cut from another sheet of paper. The deposition area was of 50 cm^2.

Figure 1(c) shows a photograph of a set of resistors printed on paper: the lateral dimensions of the resistors and their resistance are independent since the amount of clusters deposited to form each individual component can be controlled independently in an interval determined by the beam shape and the number of rastering cycles.

Figure 2(a) reports a scanning electron microscope (SEM) micrograph of the border region between metallized and pristine paper: the fibrous structure of the paper is evident. Figure 2(b) shows the border of a resistor deposited by SCBD with a step lateral resolution below 1 μm.

The typical deposition process for the production of twenty-seven resistors as shown in Fig. 1(c) takes roughly

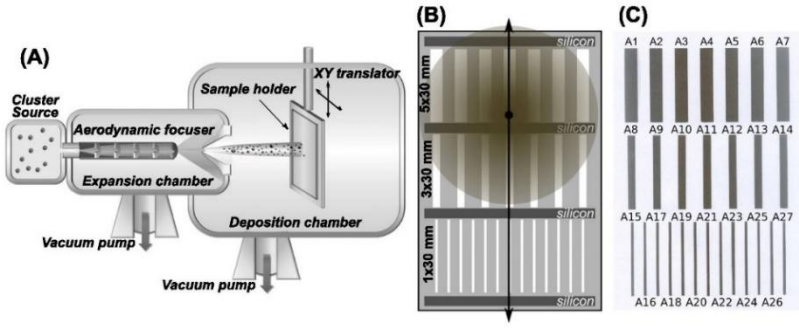

FIG. 1. (a) Schematic representation (not to scale) of a supersonic cluster beam deposition apparatus. (b) Shadow mask for resistor printing, the dark spherical area is the cluster beam deposition spot. The substrate and the mask are displaced along the vertical direction during deposition. (c) Photograph of a set of resistors printed in a one-step process with gold nanoparticles on plain paper.

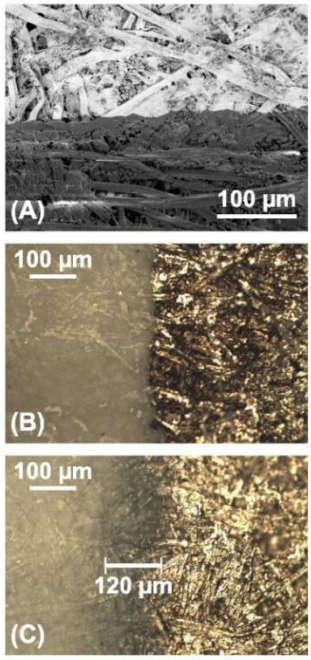

FIG. 2. (a) SEM micrograph of the border between plain paper (dark region) and the metallized one (white region). (b) Optical microscope micrograph of a border of a SCBD printed resistor. The step lateral resolution is below 1 μm. (c) Optical microscope micrograph of a border of evaporated resistor. The step lateral resolution is about 120 μm.

30 min, as a proof of principle we printed two sets of resistors ranging from 100 Ω to 28 kΩ and 270 Ω to 160 kΩ, respectively. The resistance measurement was performed using a digital ohmmeter pressing two flat probes on the resistor short edges.

For the sake of comparison, we produced, using the same shadow mask, a set of resistors using gold evaporated by joule heating in a standard metallization apparatus. Gold was evaporated for about 10 min from a molybdenum crucible placed at a distance of roughly 30 cm from the substrate within a chamber at a pressure of about 5×10^{-5} mbar.

The effusion rate from the crucible is angle dependent,[24] and this, in principle, can be used to produce resistors with a different amount of material and hence different resistances. With this method, we obtained a set of resistors similar to that produced by SCBD, while in a considerably narrower resistance interval from 23 to 470 Ω. The use of a standard evaporator results also in lower lateral resolution: Fig. 2(c) shows the border of a resistor placed near the shadow mask margin (where the mask-substrate separation is lower), the measured lateral resolution is about 120 μm, and for a resistor in the middle of the shadow mask the resolution is over 300 μm. Another disadvantage is that in the evaporative deposition method, a large quantity of gold is wasted in the chamber.

The growth mechanisms and the subsequent evolution of the electrical properties of cluster-assembled films are different from those of atom-assembled films.[20,21] This indicates that the capability of SCBD of producing in one step resistors with different dimensions in a wide range of resistance values, is due to the capability of working in a well determined region of the electrical percolation curve of the cluster-assembled films.[21,23]

In order to quantify the amount of clusters deposited on the substrate, we use a quantity called equivalent thickness (t_{eq}) defined as the thickness of a film produced by an equivalent amount of nanoparticles deposited onto a rigid flat substrate.[23] The equivalent thickness is obtained in real time, during the deposition process, by the use of a quartz crystal microbalance placed near the sample, allowing us to stop the deposition at the achievement of the required thickness and hence resistance. We checked t_{eq} by measuring with an atomic force microscope the thickness of the cluster-assembled film grown on a silicon substrate mounted aside the paper substrate during deposition.

In order to compare the electrical properties of different components of the batches, the electrical sheet resistance (R_s) can be calculated for each resistor knowing its resistance and dimensions ($R_s = R \cdot$ width/length); this quantity is independent of the resistor geometry and only varies with the amount of deposited clusters. Fig. 3(a) reports the electrical sheet resistances obtained for the two sets of resistors produced by SCBD, as a function of equivalent thickness of the cluster-assembled films. According to the percolation theory,[25] we found that the trend is a power law $R_s \propto (t_{eq} - t_c)^{-t}$. Curve fitting was performed by weighted least square linear regression of $\ln(t_{eq} - t_c)$ on $\ln R_s$, where t_c was manually changed

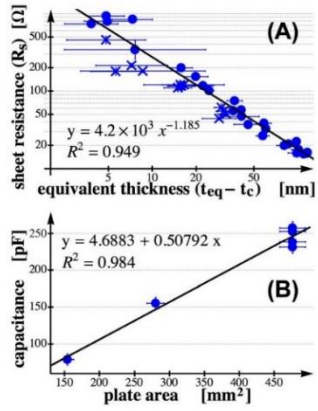

FIG. 3. (a) Electrical sheet resistance of cluster-assembled resistors on paper as a function of equivalent thickness. Curve fitting was performed by weighted least square linear regression of $\ln(t_{eq} - t_c)$ on $\ln R_s$. (b) Electrical capacitance of paper capacitors as a function of plate area.

to maximize the coefficient of determination R^2 (the uncertainty on t_c was estimate considering the interval in which the R^2 does not change appreciably). The critical thickness (t_c) of the cluster-assembled film above which we observe electrical conductance is $t_c = 18 \pm 1$ nm, and the critical exponent of the percolation curve is $t = 1.185 \pm 0.043$ in good agreement with the theory ($1 < t < 1.3$).

Using this percolation curve, we are thus able to print a set of resistors around the exact value of any required resistance, keeping constant the dimensions of the single element. It should be noted that we are working in a percolative regime so the amount of raw material used to fabricate the resistors does not scale with the resistance values. This is very important since it shows that working in this regime with SCBD allows to minimize the amount of raw material while covering a wide range of resistance values for any resistor shape it may be useful for further applications.

With SCBD and a rectangular stencil mask, we also produced different capacitors printing the gold layer on both sides of the paper, thus obtaining a parallel plate capacitor with paper as the dielectric medium. We printed several capacitors varying the amount of deposited gold and the geometrical dimensions of the plates. As expected, the capacitance was independent of the quantity of deposited gold, and it was linear on the area of the conductive plate. From the trend line in the capacitance versus area plot, we obtain that the printed capacitance is of 50 pF cm^{-2} (Fig. 3(b)). Knowing the thickness of the paper used (94 ± 1 μm), we get a relative dielectric constant of 5.53 ± 0.16, close to the dielectric constant value of paper found in literature.[26]

Resistors and capacitors printed on paper by SCBD are very robust, and they are not affected by film delamination of cracking even under substantial bending and deformations. As a proof of principle of the easiness of combination of different paper components, we trimmed by scissors various resistors and capacitors, and we used them to assemble simple circuits such as RC frequency filters. We used clips to connect the different components.

In order to characterize the frequency response of a typical RC filter, we used a waveform generator to send a pure harmonic wave on the filter input and a digital oscilloscope to measure the amplitude of the input and output waveform. In Fig. 4, we report the Bode plots for a low pass and high pass typical RC filters obtained by using a resistor of 16.5 kΩ and a capacitor of 231 pF. Experimental data show that the RC circuit is stable and reliable over a wide range of frequencies.

In summary, we demonstrated the parallel fabrication of batches of passive electrical components (resistors and capacitors) on plain paper by supersonic cluster beam deposition. SCBD is an additive technique allowing the deposition of neutral metal nanoparticles with a high degree of collimation and low kinetic energy. Compared with traditional direct writing techniques, SCBD can be efficiently coupled with a shadow mask for the deposition of components with controlled structure, dimensions, and electrical properties on thermolabile substrates, while maintaining a high throughput production and a low raw metal consumption. Thanks to the fine control on the amount of deposited clusters, the resistance of the components produced by SCBD can be tuned working in a suitable region of the percolation curve so that the dimension and the geometry of the resistor can be varied at will. This constitutes a substantial advantage compared to other deposition techniques such as thermal evaporation, ink jet printing and aerosol direct printing in terms of flexibility, rapidity of fabrication, optimization of the use of raw materials, and decoupling of components shape from electrical performances.

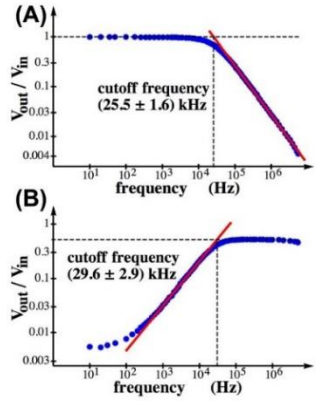

FIG. 4. Bode plots for RC filters using paper resistors and capacitors ($R = 16.5 \pm 0.2$ kΩ, $C = 231 \pm 8$ pF).

Simple circuits on paper can be easily assembled using the elements produced by SCBD; this opens the way to the rapid and cheap prototyping and integration of electrical components on paper as building blocks of more sophisticated systems for paper-based mechatronics.

[1]A. C. Siegel, S. T. Phillips, M. D. Dickey, N. Lu, Z. Suo, and G. M. Whitesides, Adv. Funct. Mater. **20**, 28 (2010).
[2]R. F. P. Martins, I. M. M. Ferreira, and E. E. M. C. Fortunato, Phys. Status Solidi RRL **5**, 332 (2011).
[3]J. Winfield, L. D. Chambers, J. Rossiter, J. Greenmanc, and I. Ieropoulos, J. Mater. Chem. A **3**, 7058 (2015).
[4]M. Nogi, N. Komoda, K. Otsuka, and K. Suganuma, Nanoscale **5**, 4395 (2013).
[5]P. K. Yang, Z. H. Lin, K. C. Pradel, L. Lin, X. Li, X. Wen, J. H. He, and Z. L. Wang, ACS Nano **9**, 901 (2015).
[6]H. Shigemune, S. Maeda, Y. Hara, U. Koike, and S. Hashimoto, in *Proceedings of the IEEE/RSJ Int. Conf. on Intelligent Robots and Systems (IROS)* (2015), p. 1091.
[7]D. Tobjörk and R. Österbacka, Adv. Mater. **23**, 1935 (2011).
[8]R. F. P. Martins, A. Ahnood, N. Correia, L. M. N. P. Pereira, R. Barros, P. M. C. B. Barquinha, R. Costa, I. M. M. Ferreira, A. Nathan, and E. E. M. C. Fortunato, Adv. Funct. Mater. **23**, 2153 (2013).
[9]H. Águas, T. Mateus, A. Vicente, D. Gaspar, M. J. Mendes, W. A. Schmidt, L. Pereira, E. E. M. C. Fortunato, and R. F. P. Martins, Adv. Funct. Mater. **25**, 3592 (2015).
[10]X. Liao, Q. Liao, X. Yan, Q. Liang, H. Si, M. Li, H. Wu, S. Cao, and Y. Zhang, Adv. Funct. Mater. **25**, 2395 (2015).
[11]Y. Zheng, Z. He, Y. Gao, and J. Liu, Sci. Rep. **3**, 1786 (2013).
[12]J. M. Hoey, A. Lutfurakhmanov, D. L. Schulz, and I. S. Akhatov, J. Nanotechnol. **2012**, 324380 (2012).
[13]A. Mahajan, C. D. Frisbie, and L. F. Francis, ACS Appl. Mater. Interfaces **5**, 4856 (2013).

[14]N. S. Kim and K. N. Han, J. Appl. Phys. **108**, 102801 (2010).
[15]E. Barborini, S. Vinati, M. Leccardi, P. Repetto, G. Bertolini, O. Rorato, L. Lorenzelli, M. Decarli, V. Guarnieri, C. Ducati, and P. Milani, J. Micromech. Microeng. **18**, 055015 (2008).
[16]M. Marelli, G. Divitini, C. Collini, L. Ravagnan, G. Corbelli, C. Ghisleri, A. Gianfelice, C. Lenardi, P. Milani, and L. Lorenzelli, J. Micromech. Microeng. **21**, 045013 (2011).
[17]T. Mazza, E. Barborini, I. N. Kholmanov, P. Piseri, G. Bongiorno, S. Vinati, P. Milani, C. Ducati, D. Cattaneo, A. Li Bassi, C. E. Bottani, A. M. Taurino, and P. Siciliano, Appl. Phys. Lett. **87**, 103108 (2005).
[18]G. Corbelli, C. Ghisleri, M. Marelli, P. Milani, and L. Ravagnan, Adv. Mater. **23**, 4504 (2011).
[19]C. Minnai and P. Milani, Appl. Phys. Lett. **107**, 073106 (2015).
[20]J. Schmelzer, Jr., S. A. Brown, A. Wurl, M. Hyslop, and R. J. Blaikie, Phys. Rev. Lett. **88**, 226802 (2002).
[21]E. Barborini, G. Corbelli, G. Bertolini, P. Repetto, M. Leccardi, S. Vinati, and P. Milani, New J. Phys. **12**, 073001 (2010).
[22]P. Piseri, H. V. Tafreshi, and P. Milani, Curr. Opin. Solid State Mater. Sci. **8**, 195 (2004).
[23]C. Ghisleri, F. Borghi, L. Ravagnan, A. Podestà, C. Melis, L. Colombo, and P. Milani, J. Phys. D: Appl. Phys. **47**, 015301 (2014).
[24]M. Ohring, *Materials Science of Thin Films*, 2nd ed. (Academic Press, New York, 2002).
[25]S. Kirkpatrick, Rev. Mod. Phys. **45**, 574 (1973).
[26]S. Simula, S. Ikäläinen, K. Niskanen, T. Varpula, H. Seppä, and A. Paukku, J. Imaging Sci. Technol. **43**, 472 (1999).

5.2.2 Supersonic cluster beam printing of carbon microsupercapacitors on paper

Status: Submitted to Flexible and Printed Electronics

Supersonic Cluster Beam Printing of Carbon Microsupercapacitors on Paper

Luca Giacomo Bettini*, Andrea Bellacicca, Paolo Piseri, Paolo Milani**

Cimaina and Physics Department, University of Milano, via Celoria 16, 20133 Milano, Italy

E-mail: * lucagiacomo.bettini@unimi.it, ** pmilani@mi.infn.it

Keywords: microsupercapacitors, paper, carbon, ionic liquids, supersonic cluster beam deposition

Abstract. Paper is a cheap, lightweight and renewable material with increasing applicative interest as a substrate for disposable and flexible electronics. The integration of planar energy storage devices on paper is a necessary and challenging step for the development of smart and autonomous flexible electronic platforms. Here we report the one-step, room temperature, fabrication of planar microsupercapacitors where nanostructured current collectors and carbon electrodes are deposited by Supersonic Cluster Beam Deposition (SCBD) on plain paper sheets and 1-Ethyl-3-methylimidazolium bis(trifluoromethanesulfonyl) imide ([Emim][NTf2]) is used as ionic liquid electrolyte. As prepared microsupercapacitors showed a high capacitance density of about 7 F cm^{-3} and good capacity retention upon prolonged cycling. The encapsulation of SCBD-made microsupercapacitors by means of a polydimethylsiloxane (PDMS) layer and their usability in driving a low power temperature sensor are demonstrated.

1. Introduction

The rapid obsolescence of electronic devices and the consequent growth of electronic waste is a major consequence of a linear economy approach where waste production is the endpoint of any manufacturing process [1]. A circular economy, based on the efficient recycling of goods, produced by natural and renewable resources, is emerging as a sustainable alternative [2].

Paper is the cheapest, most efficient and renewable material with widespread use in information registration and storage and packaging; cellulose, its main component, is the Earth's most abundant biopolymer [3]. Along with its abundance and low cost, paper is a lightweight and flexible/foldable material. Paper is rapidly being recognized as a key element for the development of novel electronic components and devices as a substrate and/or as an active component [4, 5]. Paper electronics is a field encompassing the fabrication of recyclable, disposable, portable and cheap devices like sensors, displays, RFID tags, bioassays and point-of-care diagnostics [5, 6]. Lab-on-paper, paper based sensing devices and printed circuit boards integrating different electronic components have been recently demonstrated [5-8]. The development and the practical use of paper-based electronic platforms require the integration of energy storage and energy harvesting capabilities [7].

Microsupercapacitors are energy storage devices with several very attractive features, such as long service life, fast charge/discharge rates and safety reliability, that well meet the requirements of self- and low-power components [9, 10]. Their integration in paper-based complex systems including energy harvesters and functional devices is an enabling strategy toward the development of autonomous flexible systems [10]. Supercapacitors store electric charges in the electric double layer formed at the interface between a polarizable electrode and an ion-conducting electrolyte. Their performances are typically enhanced through the enlargement of the interface area via nanostructuring of electrodes [11]. Nanostructured carbons with high surface-to-volume ratio are among the most employed electrode materials since they

can provide high electrical conductivity, chemical inertness, large gravimetric capacitance and low cost [12, 13].

To date the fabrication of carbon microsupercapacitors on paper by direct printing techniques ensuring substrate compatibility and control of electrode design and structure remains a major challenge. Carbon-based materials with high electrochemical capacitance can be deposited by several techniques, such as drop-casting, magnetron sputtering, electrostatic spray and electrophoresis [14-17]. These methods are promising for the integration of porous carbons onto the standard substrates commonly employed by the semiconductor industry (e.g. silicon) but typically involve aggressive thermal or chemical fabrication steps that are not suitable when unconventional and fragile substrates as paper are employed.

Recently attempts of printing carbon electrodes on paper to produce microsupercapacitors have been made by drawing with graphite pencils and by depositing inks containing carbon nanoparticles via solution-based processes [18, 21]. These approaches allow the fabrication of devices with excellent storage performances. However the use of solvents causes problems of cleanliness and adhesion to the substrate. Moreover, the lack of micrometric and submicrometric control over carbon layer properties such thickness, shape and lateral resolution is a severe limitation toward the micro- and nano-integration of supercapacitors on paper.

Supersonic Cluster Beam Deposition (SCBD) is an additive technology based on the production of intense and highly collimated nanoparticle beams that enables the large-scale and high throughput integration of nanostructured functional materials on a wide variety of substrates, including microfabricated platforms, smart nanocomposites and fragile materials [22-27]. The assembling of carbon nanoparticles via SCBD is a suitable approach for the production of porous carbon thin films with structural and morphological properties that are beneficial for electrochemical applications [28, 29]. The use of SCBD for the integration of carbon electrodes into conventional flexible substrates (e.g. Mylar) for

the fabrication miniaturized devices, such as supercapacitors and electrolyte gated transistors, has been recently reported [30, 31].

Here we demonstrate that paper-based microsupercapacitors can be efficiently fabricated, in a single-step process and without employing any pre- or post-deposition treatment of the substrates, by the deposition on plain paper sheets of neutral carbon clusters aerodynamically accelerated in vacuum by a supersonic expansion.

2. Experimental

2.1 Fabrication of microsupercapacitors

NsC electrodes of thickness of 200 nm and area of 0.24 cm^2, separated by a 0.5 mm gap, were deposited in high-vacuum (~10^{-5} Torr) by SCBD over a commercial plain white paper for ink-jet and laser printer (Xerox Digital, 75 g m^{-2}, roughness: 170 ml min^{-1}) previously coated by a cluster-assembled Au film (with 100 nm thickness) deposited by the same technique and serving as current collector. The electrode design and geometry was controlled using shadow masks cut from another sheet of paper. The carbon and gold clusters deposited on the top of the paper substrate were produced in a Pulsed Microplasma Cluster Source (PMCS) by the ablation of a graphite and gold target, respectively. As previously reported, the mixture of clusters and inert gas present in the PMCS leaves the internal cavity of the source by expanding through a nozzle, thus forming a seeded supersonic beam of aerodynamically accelerated nanoparticles that are finally collected on the substrate located on the beam trajectory (figure 1(a)) [22, 23]. Nanoparticles impinging on the substrate form a cluster-assembled film. As the cluster kinetic energy is low enough to avoid fragmentation upon landing, a nanostructured film of relatively soft-landing particles retaining the structural properties of the gas-phase aggregates is grown. As prepared NsC electrodes were, then, soaked with the 1-Ethyl-3-methylimidazolium bis(trifluoromethanesulfonyl)imide ([Emim][NTf2]) ionic liquid with no need of any post-deposition treatments. In the case of encapsulated device a thin layer of polydimethylsiloxane (PDMS) was applied on top of the electrolyte soaked

electrode by blade coating and curing in oven at 80°C for 60 minutes. Each nsC electrode in the series connection of three or two microsupercapacitors has an area of 0.24 cm^2 and a thickness of 200 nm.

2.2 Electrochemical characterization

The electrochemical impedance spectroscopy (EIS), cyclic voltammetries (CV) and galvanostatic charge/discharges (GLV) were performed using Gamry Ref600 potentiostat/galvanostat. Impedance spectra were acquired in the frequency range from 10^{-2} to 10^5 Hz, under open circuit potential condition at AC perturbation amplitude of 5mV rms. Cyclic voltammetry curves were acquired at 0.1, 0.5, 1 V s^{-1} scan rate in the potential range 0÷1.8 V and 0÷5.4 V for the single microscupercapacitor and the series connection of three microsupercapacitors, respectively. Galvanostatic charge/discharge analysis was performed at 20, 40, 80, 200, 400 and 800 µA cm^{-2}. The energy (E) and power (P) densities reported in the Ragone plot were calculated from the galvanostatic discharge using the following equations:

$$E = I\int Vdt / 3.6$$

$$P = E/(t_{0V} - t_{1.8V})$$

where I is the current density (in A cm^{-3}) and t0V and t1.8V are the times at the end (0 V) and beginning (1.8 V) of the discharge. The volumetric densities of capacitance, energy and power were calculated by considering a volume of $9.6 * 10^{-6}$ cm^3 which only take into account the area and the thickness of the two nsC electrodes. The areal densities refer to the area of one electrode (0.24 cm^2).

3. Results and discussion

The coupling between the SCBD technique and shadow mask printing was used to produce, in clean high vacuum conditions and at room temperature, carbon based electrodes on plain paper sheets without employing any pre- or post-deposition treatment of the substrates. Supersonic beams of gold and carbon neutral clusters, produced by a Pulsed Microplasma Cluster Source (PMCS), were employed to print

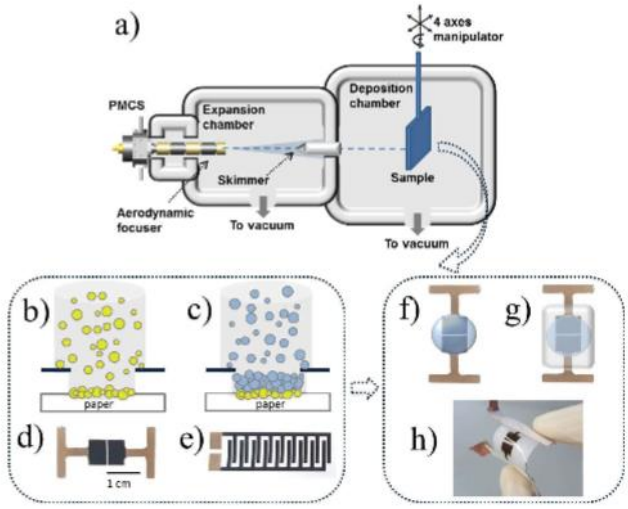

Figure 1. SCBD fabrication of microsupercapacitors on paper: (a) Schematic representation of a SCBD apparatus coupled to a PMCS source for the production of supersonic beams of neutral nanoparticles, (b) and (c) sketch of the SCBD fabrication through stencil masks of the Au current collector and nsC active material, respectively, (d) and (e) photographs of microsupercapacitors deposited on paper with different electrode design, (f) and (g) sketch of the coating of the electrodes with the ionic liquid electrolyte and the PDMS encapsulation layer, respectively, (h) photograph of an encapsulated microsupercapacitor.

electrodes with a two layer structure consisting of gold and carbon cluster-assembled thin films serving as current collector (figure 1(b)) and active material (figure 1(c)), respectively. The intrinsic porous nature of cluster-assembled nanostructured carbon (nsC) originates electrodes with a large surface area (ca. 700 m^2 g^{-1}) easily accessible to the electrolytes and beneficial towards electrochemical applications [30, 31, 33]. The use of stencil masks together with the SCBD process allows to precise positioning nanoparticles in desired locations on paper and enables the preparation of electrodes with different designs by simply

varying the shadow patterns. Figure 1(d) and 1(e) report the photographs of SCBD-made microsupercapacitors with coplanar normal and interdigitated electrodes, respectively. These electrode designs were easily realized exploiting the different shadow effects of handmade stencil masks fabricated by cutting a piece of paper. As prepared electrodes were then covered with a thin layer of a hydrophobic imidazolium-based room temperature ionic liquid by drop coating technique in order to allow the ionic contact between the two electrodes (figure 1(f)).

Figure 2 reports the electrochemical characterization of the SCBD-made microsupercapacitor consisting of two coplanar electrodes with a normal design, such as that reported in figure 1(d). The microsupercapacitor features a single electrode area of 0.24 cm^2 and a nsC layer thickness of 200 nm. This electrode design was preferred as, ceteris paribus (e.g. gap width and nsC area), it minimizes the device footprint area. As reported in figure 2(a) the complex impedance of the discharged device highlights a low frequency capacitive behavior owed to the electric double layer formation at the carbon/electrolyte interface. The value of the complex impedance at 10 mHz indicates a capacitance of about 0.2 mF cm^{-2} (figure 2(b)) while from the real axis intercept at 100 kHz an equivalent series resistance (ESR) of about 150 Ω cm^2 is estimated. The capacitive behavior of the device is observed also under cyclic voltammetric (CV) polarization conditions between 0 and 1.8 V as demonstrated by the almost box shaped CV curves acquired at sweep rates of 0.1, 0.5 and 1 V s^{-1} (figure 2(c)). A capacitance of about 0.2 mF cm^{-2} is calculated by normalizing by the scan rates the mean of the anodic currents in the 0.4÷1.2 V range. This value is in agreement with the capacitance value estimated by electrochemical impedance spectroscopy. The microsupercapacitor was also galvanostatically charged/discharged at various currents (from 20 µA cm^{-2} up to 800 µA cm^{-2}) with 0÷1.8 V cut off voltage. The cell voltage profiles of the device upon charge and discharge cycling at 80, 200 and 400 µA cm^{-2} are shown in figure 2(d). At these current densities the discharge time ranged between 6 and 1 s with a high coulombic efficiency of 90÷95 %. On the basis of the slope of the discharge voltage profiles the microsupercapacitor capacitance is calculated to be 7÷6 F cm^{-3}. The ohmic drop at the beginning of the discharge points out

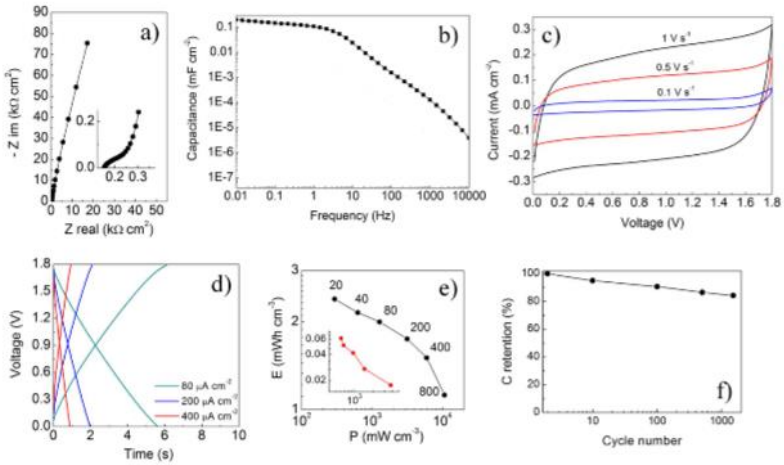

Figure 2 Electrochemical characterization of the microsupercapacitor printed on paper by SCBD. (a) Nyquist plot of the complex impedance, (b) capacitance vs. frequency plot, (c) cyclic voltammetric curves at 0.1, 0.5 and 1 V s^{-1} scan rate, (d) galvanostatic charge and discharge profiles at 80, 200 and 400 µA cm^{-2}, (e) Ragone plot, the labels indicate the GLV current densities in µA cm^{-2}, inset reports thickness normalized performances of a Mxene-on-paper microsupercapacitor [21], (f) capacitance retention as function of cycle number upon galvanostatic cycling at 200 µA cm^{-2}.

that the ESR is between 500 Ω cm^2 (at 80 µA cm^{-2}) and 375 Ω cm^2 (at 400 µA cm^{-2}) thus leading to a time constant of about 0.1 s. Considering the capacitance and the ESR measured at the lowest current, the energy ($E = \frac{1}{2} C V^2$) and power ($P = V^2 / 4 ESR$) densities are 3 mWh cm^{-3} and 40 W cm^{-3}, respectively. The galvanostatic survey at different current densities was used to build the Ragone plot shown in figure 2(e) where the volumetric energy and power densities are reported. As prepared microsupercapacitor

shows a specific energy density in the range between 1 and 2.5 mWh cm^{-3} and specific power density of 0.2 ÷10 W cm^{-3}.

Although the comparison with other devices may be not appropriate due to differences in the fabrication techniques, test conditions, material characteristics, electrolytes and electrode thicknesses, the volumetric properties of the SCBD-made supercapacitor overcome that of recently reported high-performance coplanar microsupercapacitors on paper (inset of figure 2(e)) [21]. Moreover, if compared to other forms of carbon that have been tested for the fabrication of microsupercapacitors (e.g. carbon nanotubes, carbide derived carbons, onion like carbons and graphenes) [16, 34-36], nsC has the key advantages of being deposited at room temperature with precise control over its thickness (from few tens of nanometers up to micrometers), of being inherently porous and well-adhered to substrates thus avoiding complicated multistep processing, including sintering, chemical activation and binder mixing [28, 29]. As reported in figure 2(f), the capacitance retention ratio of the microsupercapacitor, tested by galvanostatic charging and discharging at 200 μA cm^{-2}, was measured to be ca. 85 % after 1.5 x 10^3 cycles indicating a good cycling stability.

The encapsulation of the device is crucial towards many practical applications and, even if in our case the ionic liquid was well confined in the nsC film [33], helps in preventing electrolyte losses and contamination [4]. In this work a thin layer of polydimethylsiloxane (PDMS) was applied on the electrolyte-soaked electrodes, as schematically showed in figure 1(g), by blade coating and subsequent curing in an oven. The PDMS coating allowed the electrical insulation and leakage protection of the structure. A photograph of a PDMS-coated device is reported in figure 1(h). The encapsulated device retains the capacitive behavior, as indicated by its complex impedance (figure 3(a)), and, despite a significant increase in the ESR that is reasonably due to a reduced ion mobility, presents an areal capacitance similar to that of the bare device (figure 3(b)). The wrapping of the encapsulated device around a tube of 2 cm in diameter was used to test the possibility of operating the microsupercapacitor

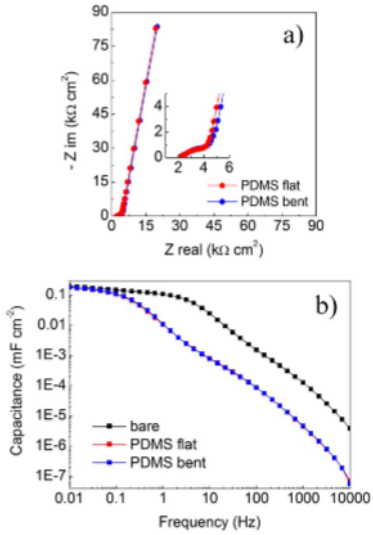

Figure 3 (a) Nyquist and (b) capacitance vs. frequency plots of the PDMS-encapsulated microsupercapacitor in the flat and bent state.

under bending conditions. As reported in figure 3(a) and 3(b) no significant differences in the electrochemical performances are present between the flat and bent state.

The reported energy storage capabilities make the SCBD-produced microsupercapacitors interesting toward the development of paper-based self-powered systems. Indeed the measured performances are useful in a variety of applications where low power electronic devices must be operated, as for instance radio-frequency identification tags (RFID) [37], or the charge generated by paper-based power sources, such as fluidic batteries [38], nanogenerators [39] and biobatteries [40] must be stored. Moreover, in view of real applications, the versatility of SCBD in integrating and precisely positioning nanoparticles onto paper allows the production of a variety of microsupercapacitors and circuits with tunable shape and

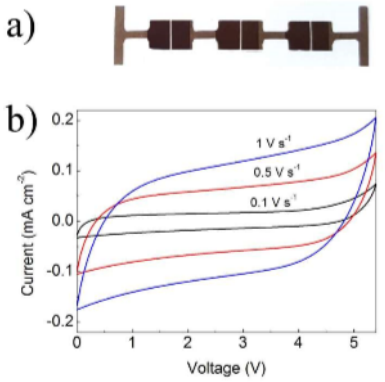

Figure 4 (a) Photograph of a series connection of three microsupercapacitors printed on paper by SCBD, (b) cyclic voltammetries at different scan rates of the three microsupercapacitors connected in series.

dimensions according to specific requirements in terms of device footprint, thickness, capacitance and operating voltage. As example, in order to increase the maximum output voltage of the cluster-assembled energy storage structures, a series connection of several microsupercapacitor can be easily fabricate in a single-step by SCBD employing a properly designed shadow mask. This approach was used to print a circuit consisting in the series combination of three microsupercapacitors featuring electrodes with similar nsC thickness and area (figure 4(a)) thus increasing the operation voltage of the SCBD-made device from 1.8 to 5.4 V, as shown by the CV curves of figure 4(b).

Finally, to demonstrate the practical application the SCBD-printed devices and test their integration with standard technological components we realized a system (figure 5(a)) enabling both the inductive charging of two encapsulated microsupercapacitors connected in series (figure 5(b)) and their use to drive a commercial analog temperature sensor (Linear Active Thermistor™ Intergrated Circuit, Microchip) requiring an operating current of few µA and an operating voltage of 2.3÷5.5 V. We built a wireless

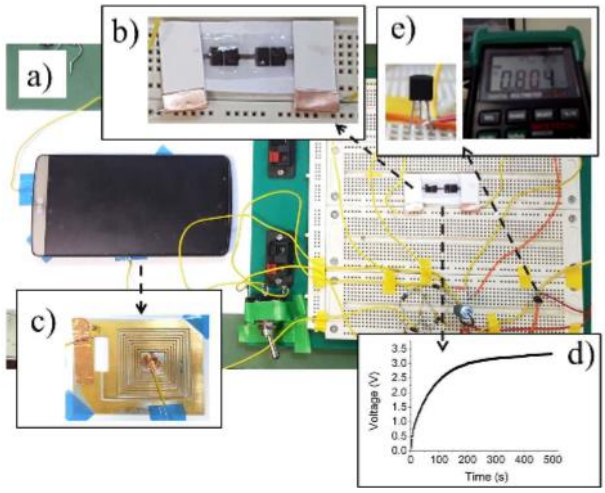

Figure 5 System integration of SCBD-printed microsupercapacitors. (a) Photograph of the circuit board used to test the charging and the discharging of (b) the series connection of two microsupercapacitors printed on paper by SCBD microsupercapacitors, (c) home-built antenna to harvest energy from a NFC-enabled mobile phone, (d) voltage vs. time of the microsupercapacitor series connection during inductive charging, (e) voltage output of the temperature sensor powered by the microsupercapacitors.

energy harvester based on an inductive coupler, shown in figure 5(c), to transfer energy from a NFC-enabled mobile phone to the microsupercapacitors. Despite the low efficiency due to the lack of optimization in the charging circuits, this system allowed to charge wirelessly the microsupercapacitors up to a voltage of ca. 2.5 V in less than 2 minutes (figure 5(d)). The stored charge was then successfully used to activate the sensor for sufficient time (ca. 1 s) to measure the temperature of the room. As shown in Figure 5e the sensor output voltage was measured to be 804 mV corresponding to a temperature of about 30 °C.

4. Conclusions

We presented a fast, single-step and high precision method for the integration of microsupercapacitors, based on cluster-assembled carbon electrodes, into standard paper sheets. Ready to use porous electrodes were deposited employing non-contact shadow masks by taking advantage of the high directionality and collimation typical of supersonic beams. As prepared electrodes were soaked in ionic liquid to fabricate capacitive paper-based devices that were also demonstrated to be easily sealed by means of a PDMS layer. The use of these devices for driving a temperature sensor was demonstrated. The manufacturing process reported in this work and based on Supersonic Cluster Beam Deposition (SCBD) enables the room temperature fabrication of thin, planar and flexible devices with energy storage performances that are consistent with the typical low-power requirements of paper electronics thus paving the way for the development of smart and autonomous paper based electronic platforms.

References

[1] Widmer R, Oswald-Krapf H, Sinha-Khetriwal D, Schnellmann M and Böni H 2005 Global perspectives on e-waste *Environ. Impact. Asses.* **25** 436–458.

[2] Stahel WR 2016 The circular economy *Nature* **531** 435–438.

[3] Niaounakis M *Biopolymers: Reuse, Recycling, and Disposa* William Andrew Publishing: Oxford, 2013.

[4] Tobjörk D and Österbacka R 2011 Paper Electronics *Adv. Mater.* **23** 1935–1961.

[5] Mahadeva SK, Walus K and Stoeber B 2015 Paper as a Platform for Sensing Applications and Other Devices: A Review *ACS Appl. Mater. Interfaces* **7** 8345−8362.

[6] Martinez AW, Phillips ST, Butte MJ and Whitesides GM 2007 Patterned Paper as a Platform for Inexpensive, Low-Volume, Portable Bioassays *Angew. Chem. Int. Ed.* **46** 1318 –1320.

[7] Hamedi MM, Ainla A, Güder F, Christodouleas DC, Fernández-Abedul MT and Whitesides GM 2016 Integrating Electronics and Microfluidics on Paper *Adv. Mater.* **28** 5054–5063.

[8] Ge L, Wang P, Ge S, Li N, Yu J, Yan M, and Huang J 2013 Photoelectrochemical lab-on-paper device based on an integrated paper supercapacitor and internal light source *Anal. Chem.* **85** 3961–3970.

[9] Beidaghi M and Gogotsi Y 2014 Capacitive energy storage in micro-scale devices: recent advances in design and fabrication of micro-supercapacitors *Energy Environ. Sci.* **7** 867-884.

[10] Soavi F, Bettini LG, Piseri P, Milani P, Santoro C, Atanassov P and Arbizzani C 2016 Miniaturized supercapacitors: key materials and structures towards autonomous and sustainable devices and systems *J. Power Sources* **326** 717–725.

[11] Yu Z, Tetard L, Zhai L and Thomas J 2015 Supercapacitor electrode materials: nanostructures from 0 to 3 dimensions *Energy Environ. Sci.* **8** 702-730.

[12] Zhang LL and Zhao XS 2009 Carbon-based materials as supercapacitor electrodes *Chem. Soc. Rev.* **38** 2520-31.

[13] Pandolofo AG and Hollenkamp AF 2006 Carbon properties and their role in supercapacitors *J. Power. Sour.* **157** 11-27.

[14] El-Kady MF and Kaner RB 2013 Scalable fabrication of high-power graphene micro-supercapacitors for flexible and on-chip energy storage *Nature Commun.* **4** 1475.

[15] Huang P, Lethien C, Pinaud S, Brousse K, Laloo R, Turq V, Respaud M, Demortière A, Daffos B, Taberna PL et al. 2016 On-chip and freestanding elastic carbon films for micro-supercapacitors *Science* **351** 691-695.

[16] Beidaghi M and Wang C 2012 Micro-supercapacitors based on interdigital electrodes of reduced graphene oxide and carbon nanotube composites with ultra high power handling performance *Adv. Funct. Mater.* **22** 4501–4510

[17] Huang P, Heon M, Pech D, Brunet M, Taberna PL, Gogotsi Y, Lofland S, Hettinger JD and Simon P 2013 Micro-supercapacitors from carbide derived carbon (CDC) films on silicon chips *J. Power Sour.* **225** 240-244.

[18] Zheng G, Hu L, Wu H, Xie X and Cui Y 2011 Paper supercapacitors by a solvent-free drawing method *Energy Environ. Sci.* **4** 3368-3373.

[19] Kurra N and Kulkarni GU 2013 Pencil-on-paper: electronic devices *Lab. Chip.* **13** 2866-2873.

[20] Weng Z, Su Y, Wang DW, Li F, Du J and Cheng HM 2011 Graphene–cellulose paper flexible supercapacitors *Adv. Energy Mater.* **1** 917–922.

[21] Kurra N, Ahmed B, Gogotsi Y and Alshareef HN 2016 MXene-on-Paper Coplanar Microsupercapacitors *Adv. Energy Mater.* 1601372.

[22] Piseri P, Tafreshi HV and Milani P 2004 Manipulation of nanoparticles in supersonic beams for the production of nanostructured materials *Curr. Opin. in Solid State and Mater. Sci.* **8** 195-202.

[23] Wegner K, Piseri P, Tafreshi HV and Milani P 2006 Cluster beam deposition: a tool for nanoscale science and technology *J. Phys. D: Appl. Phys.* **39** R439.

[24] Barborini E, Vinati S, Leccardi M, Repetto P, Bertolini G, Rorato O, Lorenzelli L, Decarli M, Guarnieri V and Ducati C 2008 Batch fabrication of metal oxide sensors on micro-hotplates *J. Micromech. Microeng.* **18** 055015-22.

[25] Corbelli G, Ghisleri C, Marelli M, Milani P and Ravagnan L 2011 Highly deformable nanostructured elastomeric electrodes with improving conductivity upon cyclical stretching *Adv. Mater.* **23** 4504–4508.

[26] Barborini E, Piseri P, Podestà A and Milani P 2000 Cluster beam microfabrication of patterns of three-dimensional nanostructured objects. *Appl. Phys. Lett.* **77** 1059-61.

[27] Caruso F, Bellacicca A and Milani P 2016 High-throughput shadow mask printing of passive electrical components on paper by supersonic cluster beam deposition *Appl. Phys. Lett.* **108**, 163501.

[28] Bettini LG, Bardizza G, Podestà A, Milani P and Piseri P 2013 Electrochemical impedance spectroscopy on nanostructured carbon electrodes grown by supersonic cluster beam *J. Nanopart. Res.* **15** 1429.

[29] Bettini LG, Divitini G, Ducati C, Milani P and Piseri P 2014 Nickel nanoparticles effect on the electrochemical energy storage properties of carbon nanocomposite films *Nanotechnology* **2** 435401.

[30] Yi Z, Bettini LG, Tomasello G, Kumar P, Piseri P, Valitova I, Milani P, Soavi F and Cicoira F 2017 Flexible conducting polymer transistors with supercapacitor function *J. Poly. Sci. Pol. Phys* **55** 96–103.

[31] Bettini LG, Piseri P,De Giorgio F, Arbizzani C, Milani P and Soavi F 2015 Flexible, ionic liquid-based micro-supercapacitor produced by supersonic cluster beam deposition *Electrochim. Acta* **170** 57-62.

[32] Barborini E, Piseri P and Milani P 1999 A pulsed microplasma source of high intensity supersonic carbon cluster beams *J. Phys. D: Appl Phys* **32** L105

[33] Bettini LG, Galluzzi M, Podestà A, Milani P and Piseri P 2013 Planar thin film supercapacitor based on cluster-assembled nanostructured carbon and ionic liquid electrolyte *Carbon* **59** 212-220.

[34] Chmiola J, Largeot C, Taberna PL, Simon P and Gogotsi Y 2010 Monolithic carbide-derived carbon films for micro-supercapacitors *Science* **328** 480-483.

[35] Pech D, Brunet M, Durou H, Huang P, Mochalin V, Gogotsi Y, Taberna PL and Simon P 2010 Ultrahigh-power micrometre-sized supercapacitors based on onion-like carbon *Nat. Nanotechnol.* **5** 651-54.

[36] Xiong G, Meng C, Reifenberger RG, Irazoqui PP and Fisher TS 2013 A review of graphene-based electrochemical microsupercapacitors *Electroanalysis* **26** 30-51.

[37] Pillai V, Heinrich H, Dieska D, Nikitin PV, Martinez R and Seshagiri Rao KV 2007 An ultra-low-power long range battery/passive RFID tag for UHF and microwave bands with a current consumption of 700 nA at 1.5 V *IEEE T. Circuits Syst.* **54** 1500-1512.

[38] Thom NK,Yeung K, Pillion MB and Phillips ST 2012 "Fluidic batteries" as low-cost sources of power in paper-based microfluidic devices *Lab Chip* **12** 1768-1770.

[39] Zhong Q, Zhong J, Hu B, Hu Q, Zhou J and Wang ZL 2013A paper-based nanogenerator as a power source and active sensor *Energy Environ. Sci.* **6** 1779-1784.

[40] Fraiwan A, Kwan L and Choi S 2016 A disposable power source in resource-limited environments: A paper-based biobattery generating electricity from wastewater *Biosens. Bioelectron.* **85** 190-197.

5.3 Conclusions

I have demonstrated how to exploit SCBD to print electronic components to deposit gold clusters on paper substrate. It is possible to print conductive paths, resistors (with resistance values that span in a range of several order of magnitude) and capacitors controlling both the amount of nanoparticles deposited on a certain area and its geometry. I have also demonstrated that it is possible to combine these elements to realize low pass and high pass RC filters whose behavior is in agreement with the theoretical model.

In order to increase the capacitance of the printed capacitors, I designed and realized with SCBD a planar capacitor with gold/carbon electrodes on paper substrate. The high capacitance value is obtained using an ionic liquid as electrolyte. I have used this super capacitor to power a small temperature sensor, showing also the possibility to wireless recharge it using the near-field communication system of a common smartphone.

6 Hybrid devices

6.1 Introduction

Combining hard materials, soft materials and electronic components it's crucial to develop innovative devices with cutting-edge functionalities, yet it is a challenging task. Several critical issues, already discussed, have to be overcome. This chapter aim to show the possibility to fabricate working devices by means of SCBI. Hard materials, soft materials and electronic components have been successfully incorporated in a single device with unique features, exploiting all the peculiarities of the materials involved in the fabrication. In the next section I will present an innovative multilayer stretchable keyboard that drives a LED matrix printed on paper substrate. The keyboard is provided with stretchable conductive vias that create an electrical link among the layers. Paper/gold connectors are exploited to link the stretchable materials with the electronic circuit that is in charge to drive the system. The paper softness avoids the issues related with the different mechanical properties of the materials involved. The electronic system also turns on or off the LEDS of a LED matrix printed on a paper substrate. The matrix is made out of nine LEDs powered by nine gold resistors printed with SCBD.

Then I will describe a novel pressure sensor that exploit optical and electrical signals to discriminate different type of deformations. It is made by a led and a light sensor embedded in a PDMS block. On the surface, several conductive electrodes are made by means of SCBI. The electrical properties and the shape of the conductive electrodes are tailored in such a way that a tiny bending of the device induces a significant alteration of its conductivity.

6.2 Supersonic Cluster Beam Fabrication of a Stretchable Keyboard with Multilayer Electrical Interconnects Integrated with Paper-based Flexible Devices

Submitted to: Smart Materials and Structures

Supersonic Cluster Beam Fabrication of a Stretchable Keyboard with Multilayer Electrical Interconnects Integrated with Paper-based Flexible Devices

Andrea Bellacicca and Paolo Milani

CIMAINA and Dipartimento di Fisica, Università degli Studi di Milano,

via Celoria 16, 20133 Milano, Italy

Abstract

The development of stretchable and flexible electronics based on soft polymeric substrates and components requires the development of novel approaches in the design, fabrication, integration, and packaging of passive and active electronic components. Here we demonstrate the fabrication, based on the use of supersonic cluster beam implantation and deposition, of a system consisting of a stretchable keyboard made by PDMS connected with a touch sensor and a matrix of LEDs printed on paper through paper-based interconnections. The stretchable keyboard has conductive vias to electrically link the front and bottom layers. Gold conductive films printed on paper are used to connect the keyboard with the electronic circuit that is in charge to drive the LED matrix.

Introduction

The development of stretchable and flexible electronics based on soft polymeric substrates and components is pivotal for applications in wearable devices and sensors, personalized healthcare, soft robotics, and smart prosthetics [1, 2, 3]. The use of polymeric substrates requires a radical change in the design, fabrication, integration, and packaging of passive and active electronic components [3, 4, 5], this has to cope with the necessity of rely on well-established and economically sustainable production technologies developed in the last four decades for rigid substrates.

Complex stretchable electronic systems have been fabricated by embedding ultra-thin semiconductor-based integrated circuits in elastomeric matrices such as PDMS [6]. This approach required the development of an electrical interconnectivity based on meander-like conductive paths resilient to compressive and tensile strain associated with stretching, bending and twisting [7]. Although very powerful and effective, this solution is highly complex and expensive since it requires the same facilities of silicon micro and nanofabrication.

An alternative to circuit embedding is the Direct Chip Attachment (DCA) where a microchip or die are directly mounted on and electrically connected through a circuit printed on a flexible substrate (Chip on Flex, COF) [8, 9]. DCA typically deals with relatively large conductive features: low cost, speed of fabrication, and the ability to integrate multiple, discrete components into a functional system are the key parameters [3]. At present flexible substrate materials for COF are based on multilayer manufacturing and the attached discrete components are connected by wire bonding [9].

A recently proposed approach to produce stretchable electrical circuits is based on the use of polymer-metal nanocomposites produced by implanting neutral metallic clusters in PDMS by supersonic cluster beam implantation (SCBI) [10, 11]. Metal-polymer nanocomposites are very convenient as substrates for stretchable circuits, however their mechanical properties (Young modulus) are unfavorable for the interconnection with other devices where the use of wires and rigid substrates is required.

Two major challenges are still associated with the fabrication of stretchable devices: i) the limitation to integration density of the components when only a single layer of interconnects is used; ii) the connection of stretchable parts with different hard components or substrates: the matching between soft and rigid components in electrical or mechanical connections remains a major technical issue to be solved.

A polymeric substrate very promising for the fabrication of flexible electronic circuits is paper [3, 12]: it is low cost and fully recyclable, it can be easily shaped and trimmed with scissors

or cutters and it can be used for complex self-standing 3D structures, fluidics and electrochemical applications [13, 14]. Recently we have reported the fabrication of passive electrical components (resistors and capacitors) on plain paper by an additive and parallel technology consisting of supersonic cluster beam deposition (SCBD) coupled with shadow mask printing [15]. Compared to standard deposition technologies, SCBD allows for the rapid production of components with different shape and dimensions while controlling independently the electrical characteristics. Discrete electrical components produced by SCBD are very robust against deformation and bending and they can be easily assembled to build circuits with desired characteristics [15]. This suggests the use of paper for the fabrication of flexible electrical connection and substrates with suitable mechanical properties to be used in conjunction with soft stretchable components as well as with rigid substrates.

Here we demonstrate the fabrication, based on the use of SCBI/SCBD, of a system consisting of a stretchable keyboard made by PDMS connected with a touch sensor and a LED matrix printed on paper through paper-based interconnections. The stretchable keyboard has conductive vias to electrically link the front and bottom layers. Gold conductive films printed on paper are used to connect the keyboard with the electronic circuit that is in charge to drive the LED matrix.

System Fabrication and Characterization

Principle of operation and lay-out

A schematic diagram of the system consisting of a stretchable keyboard, a touch sensor, an Arduino board and a LED matrix is reported in Fig. 1. The stretchable keyboard is connected to a 12-key capacitive touch sensor MPR121 [16] through a flexible wiring made by printed electrically conductive gold paths on a paper substrate. An Arduino electronic board drives the capacitive sensors and runs the paper-based LED matrix according to the signals received from the touch sensor. The LED matrix is composed by nine LEDs powered by resistors printed on paper by SCBD and it is connected to the Arduino board by standard led-strip connectors.

The capacitance variation produced by touching a pad on the keyboard is transmitted to the rear side of the keyboard through conducting vias and then to the capacitive sensor connected by the metallized paper conductors. The sensor generates a set of univocal numbers identifying which pad has been touched and it sends them to the Arduino board through an Inter-Integrated Circuit (I2C) communication channel. This triggers the Arduino board to turn on or off the correspondent LED fixed on the flexible paper substrate.

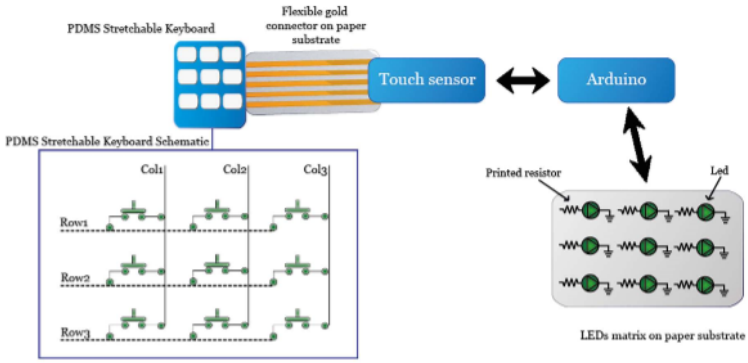

Figure 1: *Schematic representation of a PDMS stretchable keyboard connected to a touch sensor with flexible conductive electrodes realized on a paper substrate. The touch sensor sends data to an Arduino controller that, in turn, turn on or off the LEDs on a matrix printed on a paper substrate.*

The stretchable keyboard is based on a matrix architecture (Fig. 1) printed on both sides of the PDMS substrate. The bottom layer controls the columns of the matrix and it establishes the electrical connection between the keyboard and the paper connectors, the top layer integrates nine touchpads and electrical paths acting as bus dedicated to control the rows of the matrix. The two layers of the keyboard are electrically connected by twelve conductive vias. Every touchpad is realized splitting the pad in two separate parts: one connected to the column-control bus and the other connected to the row-control bus. The keyboard and the electrodes printed on paper are superimposed and bolted to a polylactic acid (PLA) plate to assure the electrical connection.

Printing of conductive paths and vias

Conductive paths (on PDMS and paper) and vias were fabricated by a Supersonic Cluster Beam Implantation/Deposition (SCBI/SCBD) apparatus equipped with a Pulsed Microplasma Cluster Source (PMCS) (Fig. 2). A detailed description of the SCBI/SCBD technology and of the deposition apparatus is reported in [10, 17]. Briefly neutral gold clusters are produced by a PMCS and accelerated for deposition or implantation in a supersonic expansion. A PMCS schematically consists of a ceramic body with a cavity where a target gold rod, acting as a cathode, is sputtered by

a localized electrical discharge ignited during the pulsed injection of Ar gas at high-pressure (40 bar). The sputtered metal atoms from the target thermalize with the carrier gas and aggregate in the source cavity forming metal clusters; the carrier gas-cluster mixture expands out of the PMCS through a nozzle into a low-pressure (10−4 mbar) expansion chamber, thus producing a highly collimated supersonic beam with a divergence lower than 1°. The central part of the beam enters a second vacuum chamber (deposition chamber, at a pressure of about 10-5 mbar) through a skimmer and it impinges on the stencil mask-target substrate system. The cluster beam flux is monitored in real time by a quartz microbalance placed close to the substrate. A motorized samples holder allows large area deposition moving the substrate target in the perpendicular plane of the nanoparticles beam [10]. An additional servomotor rotates the substrate target along is vertical axis spanning 180 degrees with a resolution of ~9 degree.

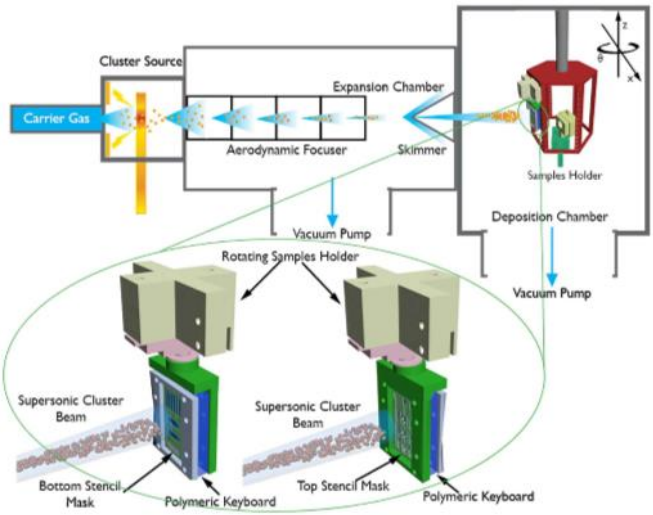

Figure 2: *Schematic representation (no to scale) of the SCBI/SCBD deposition apparatus. The inset shows the substrate holder used to fabricate on PDMS a double-sided electronic circuit electrically linked through metalized vias in a single-step process.*

In the case of the PDMS substrate, due to its soft nature, we worked in the regime of Supersonic Cluster Beam Implantation (SCBI) [10, 11]. SCBI is based on the use of a highly

collimated supersonic beam carrying metallic clusters with a kinetic energy of about 0.5 eV·atom-1. Even if the kinetic energy is significantly lower than in ion implantation, neutral clusters are able to penetrate up to tens of nanometers into the polymeric target forming a conducting nanocomposite and avoiding electrical charging and carbonization [11]. The amount of nanoparticles deposited onto the substrate target is measured in term of equivalent thickness defined as the thickness of a film made by an equivalent amount of nanoparticles deposited onto a rigid substrate [10]. We put a partially masked Si wafer close to the substrate during the metallization process. Then the mask was removed and the step between the bare Si and the metallic film was measured using a P-6 stylus profilometer (KLA Tencor, USA).

Keyboard fabrication

The keyboard (100x50x0.5 cm) has been printed on a PDMS substrate by implantation of gold clusters. PDMS was fabricated by mixing the monomer and the curing agent (Dow Corning, Sylgard 184) in a 10:1 ratio and stirred with a spatula for 20 minutes. Subsequently the mixture was put in a desiccator and degassed for one hour. The compound was then poured into the mold provided with twelve dowels pins to shape high smoothed holes to be used as conductive vias (Fig. 3A).

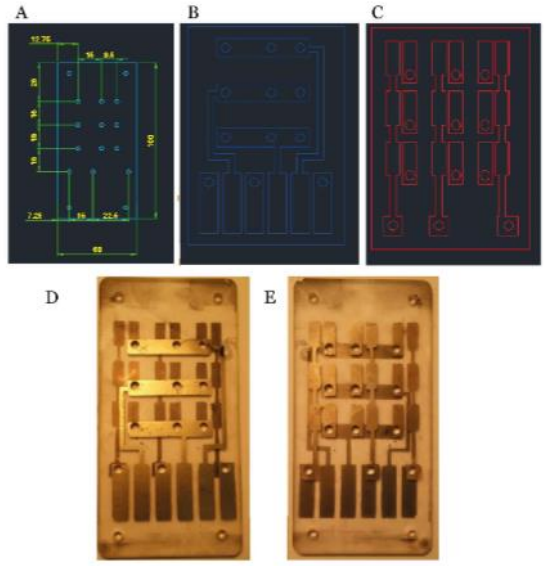

***Figure 3**: A) Keyboard design: twelve holes are used as conductive vias to connect the electrodes on the top side of the keyboard with the electrodes on the bottom side. B) Top side stencil mask with the nine touchpads used as buttons. C) Bottom side stencil mask with the six electrodes used to send the capacitive signal to the external electronic circuit. D) Picture of the keyboard bottom side after metallization. E) Picture of the keyboard top side, after metallization, with the conductive pads*

The PDMS substrate was sandwiched between two stencil masks reproducing the electrical paths to be printed and mounted on the rotating sample holder system (Fig. 2) in order to print the conductive electrodes on both sides of the target and the conductive vias during the same implantation process. The conductive paths were printed using SCBI with silver nanoparticles combined with a raster scanning technique to ensure a homogeneous metallization [18]. First the top and bottom sides of the keyboard were deposited (Figs. 3B and 3C). The substrate was then rotated of roughly 30 degrees and 120 degrees respectively to metalize the twelve holes and to obtain the conductive vias that link the top and bottom sides of the keyboard. The angles were chosen to assure that the nanoparticles beam covers all the internal surface of the vias (see Fig. 4). The nine conductive pads and the bus controlling the columns were printed on the top side of the keyboard (Figs. 3C and 3E) while on the bottom side we printed the bus to control the rows and the

links between the touchpads and the electrodes used to transfer electrical signals to the external control circuit (Figs. 3B and 3D).

Figure 4: *Top side view and section of the PDMS vias metallized by SCBI.*

LED matrix fabrication

The LED matrix was realized using SCBD to deposit gold nanoparticles on a paper substrate topped with a PLA stencil mask to shape the electrical paths [15]. The electrical resistance of the conductive paths was tailored by measuring in situ the amount of nanoparticles deposited onto the paper. High power LEDs were glued on the paper and connected to the paths through a conductive silver paste to establish a good electrical link (Figs. 5A and 5B).

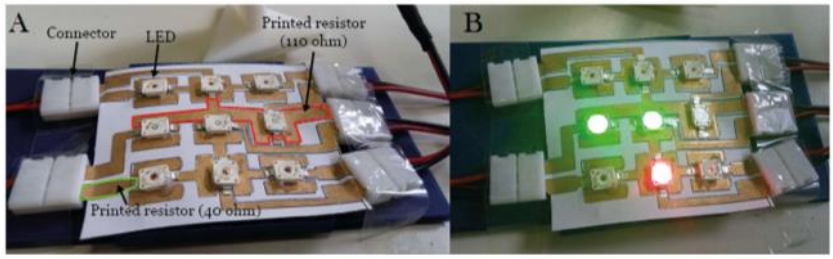

Figure 5: *A) Picture of the LEDs matrix showing the electrical circuit fabricated by SCBD of gold clusters on paper and the glued LEDS. B) LEDs are turned on by touching the PDMS keyboard.*

Gold/Paper conductive connectors

The connection between the electrodes of the bottom side of the PDMS keyboard and an external drive electronic circuit were made depositing gold with physical vapor deposition on a paper substrate topped with a PLA stencil mask to frame the electrical paths (Fig. 6).

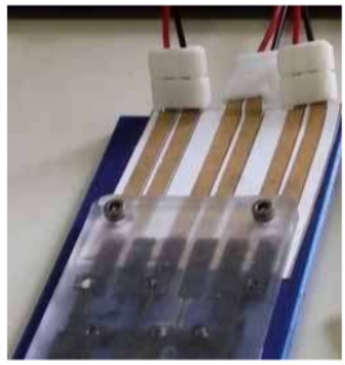

Figure 6: *Conductive paths on paper connecting the PDMS keyboards with standard connectors and wires.*

Electro-mechanical characterization

The electrical resistance of the vias were measured using an Agilent 34410A under stretching cycles up to 2.5% and 5% of linear deformation. In order to assess the durability of the electrical connection under repeated stress cycles, a portion of the keyboard of 10x20 mm including a vias were cut. The resistance was recorded after one hundred cycles of stretch/relax a 5% along the longest side.

Results and Discussion

The assembled device is shown in Fig. 7: touching the touchpads causes the correspondent LED to turning on or off. This test is replicated while bending, twisting and stretching the keyboard with no observation of delays or malfunctioning. The electrical connection between the keyboard and the electrodes printed on paper is robust enough to pipe the capacitive signal from the keyboard to the touch sensor, withstanding the mechanical deformation applied to the keyboard.

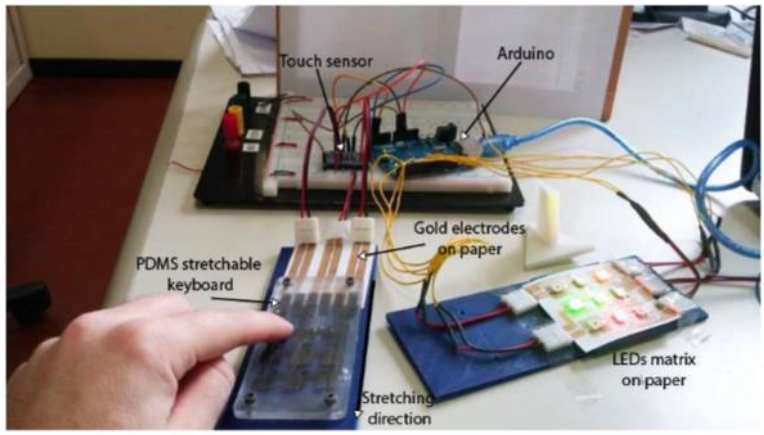

Figure 7: *Picture of the assembled device working under the finger pressure. The electric signal is red from the keyboard to the electronic circuit through a gold/paper flexible electrodes. The Arduino board in response to the touch turn on or off a LED in the LEDs matrix made of the flexible gold/paper circuit. The picture shows a test performed with the keyboard stretched of 5%.*

We used a matrix architecture for the keyboard in order to significantly simplify the electronic circuit needed to control it. In fact, a direct connections scheme (one pin per one pad) would require a one-to-one link between the touchpads and the capacitive sensor inputs. Cleary, this is not feasible mainly because of two reasons: i) this scheme would require a touch sensor with the same number of input as the number of touchpads and the higher the amount of pins, the higher the complexity of the internal logic and thus the higher the price of the electronic circuit; ii) this electrical arrangement would have required a high number of conductive paths, leading to a considerable increasing in the final complexity of the whole electronic circuit.

On the contrary, a matrix architecture significantly reduces the design complexity allowing to control up to N2 touchpads with just 2N sensor pins at the simple cost of using a two-layers electronic circuit. One layer has a bus dedicated to control the rows of the matrix, the second handles the columns of the matrix. This implies that it is possible to deal with up 36 independent touchpads with a 12-key touch sensors.

The matrix architecture is implemented in a device using a double sided electronic circuit with conductive through-hole vias links. While this is of course trivial for standard electronic circuits made on hard substrates, on the other hand the realization of conductive vias in elastomeric substrates is still challenging with common metallization techniques [4, 19].

By using SCBI it is possible the fabrication of conductive vias in PDMS thick layers, the direct metallization of the inner wall of the vias is obtained by exploiting the high collimation of the cluster to be implanted in the beam typical of supersonic expansions [17]. By tilting the substrate against the cluster beam it is possible to uniformly implant the clusters. The formation of a polymer-metal nanocomposite assures the resilience of the conducting film against stretching and bending [11].

As showed in Fig. 8 the electrodes and vias are still conductive during the stretching phase undergoing a small increase in the resistance values and restoring the initial value when the keyboard is reset to rest position.

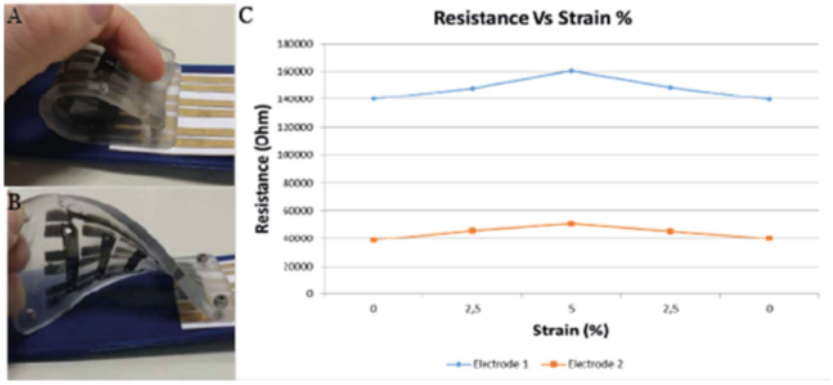

Figure 8 *A-B) stretching and bending of the PDMS keyboard. C) Evolution of the resistance for two of the conductive path-vias-conductive path of the keyboard during a stretch/relax cycle. The initial value of the resistance is recovered when the keyboard is back to the rest position.*

In order to realize the LED matrix on paper, we exploited the capability of directly printing on paper resistors by SCBD [15]. Standard electronic circuits are made by discrete components like resistors, capacitors, transistors, etc, or integrated components like microprocessors, electrically soldered on rigid printed circuit boards (PCB). The components are connected through conductive paths (CPs) usually made of copper. This architecture implies a net separation between components and electrical paths. For example, a typical circuit to power a LED is assembled using the following scheme: CP-resistor-CP-LED-CP.

Exploiting SCBD resistors and capacitors with well-defined electrical characteristic can be deposited on paper simply by controlling the amount of deposited nanoparticles [15]. This allows to

fabricate conductive paths with controlled resistance value (resistive conductive path or RCP) to limit the amount of current that flows in the LEDs and demonstrating an alternative circuit scheme such as: RCP-LED-RCP. This provides a substantial simplification in the design and realization of electronic circuits on paper.

In the case of the LEDs matrix, the resistance of the gold elements printed of paper spanned from 100 ohm to 250 ohm obtained with a cluster-assembled gold film with an equivalent thickness of 180nm (Fig. 7). These resistance values guarantee that the current sunk from the Arduino board doesn't exceed the maximum value, attested around 200 mA.

Conclusions

In summary, we reported the fabrication of a hybrid device based on the integration of electronic components and electrical circuits on different stretchable and flexible polymeric materials such PDMS and paper. By using supersonic cluster beam implantation and deposition it is possible to fabricate conductive paths and vias on polymeric stretchable substrates able to sustain deformations without altering their electrical properties. The use of electrically conductive paths printed on paper allowed the connection of PDMS devices with classical "hard" electronic units and the fabrication of complex devices matrices. This work demonstrates that SCBI/SCBD is an enabling technology for the fabrication of a novel class of complex devices based on non-conventional substrates.

References

[1] Pang C C Lee and K-Y Suh 2013 Recent advances in flexible sensors for wearable and implantable devices *J. Appl. Polym. Sci.* 130 1429-1441

[2] Rus D and Tolley M T 2015 Design, fabrication and control of soft robots *Nature* 521 467-475

[3] Siegel A C, Phillips S T, Dickey M D, Lu N, Suo Z and G. M. Whitesides 2009 Foldable Printed Circuit Boards on Paper Substrates *Adv. Funct. Mater.* 20 28-35

[4] Larmagnac A, Eggenberger S, Janossy H and Vörös J 2014 Stretchable electronics based on Ag-PDMS composites *Sci. Rep.* 4 7254.

[5] Lin Z, Moon K-S and Wong C-P 2011 Nanocomposite for low stress underfill *IEEE 61st Electronic Components and Technology Conference (ECTC)* 2045.

[6] Wu J, Liu Z J, Song J, Huang Y, Hwang K-C, Zhang Y W and Rogers J A 2011 Stretchability of encapsulated electronics *Appl. Phys. Lett.* 99 061911

[7] Rogers J A, Someya T and Huang Y 2010 Materials and Mechanics for Stretchable Electronics *Science* 3271603

[8] Baldwin D F and Beerensson J T 1999 Thermal Management in Direct Chip Attach Assemblies *J. Electron. Packaging* 121 222-230

[9] Frisk L, Järvinen J and Ristolainen R 2002 Chip on flex attachment with thermoplastic ACF for RFID applications *Microelectron. Reliab.* 42 1559-1562

[10] Ghisleri C, Borghi F, Ravagnan L, Podestà A, Melis C, Colombo L and Milani P 2013 Patterning of gold–polydimethylsiloxane (Au–PDMS) nanocomposites by supersonic cluster beam implantation *J. Phys. D. Appl. Phys.* 47 015301

[11] Corbelli G, Ghisleri C, Marelli M, Milani P and Ravagnan L 2011 Highly Deformable Nanostructured Elastomeric Electrodes With Improving Conductivity Upon Cyclical Stretching *Adv. Mater* 23 4504-4508

[12] Martins R, Ferreira I and Fortunato E 2011 Electronics with and on paper *Phys. Status Solidi RRL* 5 332-335

[13] Winfield J, Chambers L D, Rossiter J, Greenmanc J and Ieropoulos I 2015 Urine-activated origami microbial fuel cells to signal proof of life *J. Mater. Chem. A* 3 7058-7065

[14] Nogi M Komoda N Otsuka K Suganuma K 2013 Foldable nanopaper antennas for origami electronics *Nanoscale* 5 4395-4399

[15] Caruso F Bellacicca A and Milani P 2016 High-throughput shadow mask printing of passive

electrical components on paper by supersonic cluster beam deposition *Appl. Phys. Lett.* 108 163501

[16] MPR121 datasheet: https://www.sparkfun.com/datasheets/Components/MPR121.pdf

[17] Wegner K, Piseri P, Tafreshi H V and Milani P 2006 Cluster beam deposition: A tool for nanoscale science and technology," *J. Phys. D Appl. Phys.* 39 R439

[18] Marelli M, Divitini G, Collini C, Ravagnan L, Corbelli G, Ghisleri C, Gianfelice A, Lenardi C, Milani M and Lorenzelli L 2010 Flexible and biocompatible microelectrode arrays fabricated by supersonic cluster beam deposition on SU-8 *J. Micromech. Microeng.* 21 045013

[19] Guo L and DeWeerth S P 2010 High-Density Stretchable Electronics: Toward an Integrated Multilayer Composite *Adv. Mater.* 22 4030-4033

6.3 Integrated simultaneous detection of tactile and bending cues for soft robotics

Integrated simultaneous detection of tactile and bending cues for soft robotics

Massimo Totaro[*,1], *Alessio Mondini*[1], *Andrea Bellacicca*[2], *Paolo Milani*[2], *Lucia Beccai*[*,1]

[1]Center for Micro-BioRobotics, Istituto Italiano di Tecnologia, Viale Rinaldo Piaggio 34, 56025 Pontedera (Italy)

[2]CIMaINa and Department of Physics, Università degli Studi di Milano, Via Celoria 16, 20133, Milano, (Italy)

*Corresponding authors:

Dr. Massimo Totaro
Center for Micro-BioRobotics
Istituto Italiano di Tecnologia (IIT)
Viale Rinaldo Piaggio 34
56025, Pontedera (Pisa) - Italy
E-mail: Massimo.Totaro@iit.it

Dr. Lucia Beccai
Center for Micro-BioRobotics
Istituto Italiano di Tecnologia (IIT)
Viale Rinaldo Piaggio 34
56025, Pontedera (Pisa) - Italy
E-mail: Lucia.Beccai@iit.it

Mary Ann Liebert, Inc., 140 Huguenot Street, New Rochelle, NY 10801

Abstract

Soft robots should move in an unstructured environment and explore it, and, to do so they should be able to measure and distinguish proprioceptive and exteroceptive stimuli. This can be done by embedding mechanosensing systems in the body of the robot. Here, we present a polydimethylsiloxane block sensorized with an electro-optical system and a resistive strain gauge made with the Supersonic Cluster Beam Implantation (SCBI) technique. We show how to integrate these sensing elements during the whole fabrication process of the soft body and we demonstrate that their presence does not change the mechanical properties of the bulk material. Exploiting the position of both sensing systems and a proper combination of the output signals, we present a strategy to measure simultaneously external pressure and positive/negative bending of the body. In particular, the optical system can reveal any mechanical stimulation (external from the soft block or due to its own deformation), while the resistive strain gauge is insensitive to the external pressure, but sensitive to the bending of the body. This solution, here applied to a simple block of soft material, could be easily extended to the whole body of a soft robot. This approach provides detection and discrimination of the two stimuli (pressure and bending), with low computational effort and without significant mechanical constraint.

Introduction

In recent years, soft robotics[1-7] is introducing new concepts in designing artificial systems, which today are mainly based on rigid materials and joints with finite degrees of freedom that can be modeled and controlled based on widely studied mathematical tools. Most of the classical robots are designed to work in a well-defined environment and to perform precise tasks. On the other hand, soft robots are made of non-rigid materials, can have a very high number of degrees of freedom and are expected to move and operate in an unstructured environment.[8-9] All these aspects introduce several challenges in the modeling, design and control of such kind of artifacts. Materials used for building soft robots are mainly stretchable elastomers, such as platinum catalyzed silicones (i.e. polydimethylsiloxane –PDMS- or EcoflexR series). While elastic for small deformations, these materials exhibit a highly nonlinear behavior for large strains[10]. At the same time, their mechanical characteristics are useful to attempt mimicking natural skin and underlying tissues. They are a good choice for the fabrication of bioinspired robots with *mechanosensing* capability so that they can reconstruct their shape and deformation (*proprioception*) and perceive external objects by touch (*exteroception*)[11]. To our knowledge only Shepherd's group has uniquely embedded proprio- and exteroception in a soft robot[12] by way of a highly stretchable skin. Owing to the skin's capacitive and electroluminescent functions, it was demonstrated that the robot can either sense its skin stretching due to its own movement, or that it can detect a pressure coming from the outside.

In the last decade, artificial mechanosensing solutions, including tactile sensing and mechanical sensing more at large (e.g. like strain sensing), have shown a strong boost[13-17] . This has mainly been pushed by the exploitation of novel materials (e.g. graphene, metallic nanowires, functional organic compounds) and to the rapid development of fabrication techniques at the micro/nanoscale. In particular, highly deformable materials (both conductive and non-conductive) were used to mimic the basic characteristics of skin like flexibility or elasticity. For instance, strain or bending sensors, based on silver nanowires[18-19], graphene[20-22] or carbon nanotubes[23-24], have been embedded in ultrathin polymeric films. Also, sensors based on gold nanowires[25], organic transistors[26-28], and conductive textiles have been proposed[29-31]. In addition to single sensors, electronic skins (e-skin) have shown remarkable advancements, especially in the field of ultra-thin and ultra-conformable systems[12, 32-38]. However, in soft robots and wearable systems [39-44] it becomes crucial using such deformable devices to encode a variety of mechanical inputs. In doing so, several aspects that are not considered (e.g. owing to testing single specific functionalities of the devices or to

implementing them *per se*) become important. One key issue is the capability of detecting and distinguishing different types of mechanical cues either external or originated by the movement of the artifacts (e.g. pressure, strain, or bending), which we name *mechanical multi-modality*. One possible strategy should be the integration of separate transducers, each sensing one mechanical stimulus. Nevertheless, in general soft tactile sensing devices respond in a very similar way under different solicitations. This is mainly due to their basic building blocks made of soft materials that exhibit a very similar response (e.g. mostly electrical, like change in resistance, capacitance or current) to deformations induced in the device by any type of outer mechanical stimuli (e.g. indentation, traction, etc.). Most of the multimodal mechanical sensors found in the literature suffer from such limitation [45-47]. Another possible strategy is the integration of many similar sensors (i.e. transducing the same mechanical solicitation) and adopting an *ad hoc* elaboration data algorithm to discriminate between different stimulations.

Following this approach, in a previous work, we addressed the discrimination of two different types of mechanical stimuli in a soft body[48]. We used two similar sensing elements (based on e-textiles and elastomers embedded in the soft module) to recognize the convex from the concave side and detect the bending angle (or maximum deflection), and to distinguish between bending (i.e. local strain) and external force solicitation. However, when this solution is distributed along the body of the whole robot, it can be limited by the high number of connections, which would affect the mechanical behavior of the system, and by the electronic and computational complexities. For example,in Cianchetti *et al.*[49] resistive stretch sensors are exploited to reconstruct the spatial configuration of a continuum soft arm. In this case, the local curvature of the arm is retrieved with differential strain measurements, and the reconstruction method allows obtaining the spatial configuration from local deformations. Yet, the wiring needed for measuring each resistance variation is a bottleneck for real applications. Another example is given by Chossat *et al.*[50], with a soft tactile skin using an embedded ionic liquid matrix. Here, a tomographic imaging process is needed for reconstructing the stimulation map, and for larger matrices real-time elaboration is computationally very demanding.

Indeed, another and very promising strategy is to combine material structuring at the micro/nanoscale with nano-composites, such as graphene, nanowires or carbon nanotubes (CNT). For instance, following this approach a multilayer device, made of a porous rubber and an air gap between two polydimethylsiloxane (PDMS)/CNT conductive thin films, was developed to distinguish between pressure and lateral strain[51]. Similarly, a device based on

nylon and polyurethane fibers, functionalized with silver nanowires and coated with piezoresistive rubber[52] has the capability to discriminate pressure, strain and flexion.
Nevertheless, even with remarkable sensing capabilities like the abovementioned example, the current devices are optimized as single components, without considering the direct integration in a soft body. Also, they are characterized on rigid supports of the experimental set-ups. This represents another key issue that must be tackled for sensorizing soft robots, (i.e. where the substrate is the robot body made of soft elastomers, such as PDMS or EcoflexR), and wearable systems (i.e. where the substrate is the human body).

Proposed solution

In this article, we present a new mechanosensing solution that has three key aspects. The first is that it can retrieve both exteroceptive (pressure) and proprioceptive (strain due to bending) information; the second is that the two exploited transduction principles (i.e. electro-optical and resistive) are obtained through, and thanks to, a soft body; finally, the third is that the sensing technologies used do not alter the original mechanical characteristics of the starting soft material (i.e. PDMS) that will easily constitute the bulk of a future actuated structure. In future works, this proposed solution can be scaled up to sensorize an entire soft robot.
More in detail, our device is made of a PDMS block, with a photodiode and a phototransistor embedded during the fabrication process. The photodiode and the phototransistor are used as transmitter and receiver, respectively, obtaining an electro-optical sensor. The use of PDMS as soft waveguide, in combination with optical elements, for sensing mechanical stimulations has been already reported. For instance, Ramuz *et. al.[53]*presented a transparent pressure sensitive artificial skin based on a layer of PDMS embedding organic LEDs and photodetectors, while we have previously shown how the soft waveguide principle can be used to develop an extended electronic skin for distributed and multiple pressure mapping[54]. Also, very recently a fiber-reinforced soft prosthetic hand was reported, in which PDMS-based optical waveguides are exploited to detect either curvature, elongation, or external force[55]. All these results are encouraging and are starting to show the potential of using a soft transparent material having the two-fold function of mechanical substrate and waveguide material. We also use it in the present work for pressure sensing function. Then, one of the body surfaces has patterned conductive electrodes forming a resistive strain gauge, which are produced by Supersonic Cluster Beam Implantation (SCBI) that is an innovative technique for making conductive parts in soft elastomers[56]. The key point is to keep the implanted plane far away from the external surface, since the upper PDMS layer acts as a mechanical shield

for stimuli coming from the external environment, such as pressure or contact with an object. Otherwise, the resistive strain gauge would be sensitive to external pressure (in addition to strain) if the upper surface is patterned, avoiding the discrimination of multiple stimuli by combining optical and resistive signals.

In this way, the body and the sensing elements are completely merged during the whole fabrication process. We demonstrate that all embedded sensing elements do not affect the mechanical behavior of the soft body. Finally, we show that combining properly the signal outputs, it is possible to distinguish and to measure both sequential and simultaneous pressure/bending stimulations.

Materials and methods

Design and strategy for revealing simultaneous multiple stimuli

PDMS is one of the most used materials in soft robotics and the device here proposed (shown in Figure 1) can be considered as a proof-of-concept for a section of soft robot with embedded sensing capabilities. The bulk body acts as a waveguide for the light emitted by the photodiode and collected by the phototransistor. Due to the reduced dimensions of the optical elements, the mechanical bulk characteristics are not affected by their integration in the body. The implanted conductive pattern on one of the device surface is produced by SCBI. Since it is not in the middle plane (for more detail see SI), bending of the structure induces a strain on the patterned surface, which can be measured from its resistance variation. In a previous work[56], the characterization of linear strain (i.e. resistance variation vs. elongation of metal layer) has been presented, demonstrating the effectiveness of this kind of implantation as reliable and sensitive strain gauge. From this resistance variation, the positive or negative bending in a 2D plane can be revealed. Otherwise, the resistive strain gauge is almost insensitive to a pressure applied on the non-implanted surface; since the PDMS body thickness avoids that the deformation is transmitted to the opposite side. Remarkably, in contrast to other available technologies used to implant or integrate conductive paths on a soft substrate, the fabrication of conductive patterns based on a metal-polymer nanocomposite produced by SCBI ensures a complete integration of the sensing elements in the bulk, with excellent mechanical stability under deformation, while the mechanical properties of the nanocomposite (Young modulus) are substantially unchanged compared to the pristine polymer[57].

By contrast, any mechanical deformation of the body can be revealed measuring the output signal of the phototransistor, which is proportional to the incident light collected by the

receiver. Then, by combining this asymmetrical behavior, the system is able to distinguish clearly between the pressure applied on the upper surface and the positive or negative bending of the body.

This sensing strategy is quite general, since it depends weakly on the soft body shape and on the materials employed. A key point is to exploit different sensing principles completely decoupled both from the transduction and the mechanical point of view. But, at the same time, the sensing elements should be completely embedded in the body without interfering on the bulk mechanical properties. Indeed, in this case we exploit an optical system and a resistive layer as sensing elements. In addition, the strain gauge is built in a buried region of the body, in order to shield the mechanical deformations due to external applied pressure. In this way, the optical system is able to detect all bulk mechanical deformations, while the resistive gauge only the strain applied on its surface. Regarding the bulk material, a compromise in its elasticity is needed, since a completely rigid body will not be able to reveal an applied pressure, while a very soft will not shield the buried strain sensor. For these reasons, we chose a basic body shape (a parallelepiped) for experimental validation, and PDMS as soft body material, which is widely used in soft robots and it is transparent to IR light.

Finally, we should note that the described strategy is strictly valid for movement/stimulation in a 2D plane. However, it can be the basis for reconstructing movements and stimulations in the 3D space, by combining several sensing elements.

Device fabrication

The whole fabrication process is depicted in Figure 1. First of all, the PDMS block, with dimensions of 40x15x5 mm, is obtained by curing degassed PDMS (Dow Corning, Sylgard 184), with a prepolymer /cross-linker ratio of 10:1 by weight, for 24 hours at room temperature in a rigid plexiglass mold. Before pouring the PDMS, an infrared (IR) photodiode (VSMY1850, Vishay Semiconductors, USA) and an IR phototransistor (TEMT7100X01, Vishay Semiconductors, USA) are fixed into the mold, in order to be embedded in the PDMS block after the curing phase.

Additionally, one of the body surfaces has patterned conductive electrodes, produced by a Supersonic Cluster Beam Implantation (SCBI) apparatus equipped with a Pulsed Microplasma Cluster Source (PMCS). PMCS consists in a ceramic body with a cavity in which a solid gold target is vaporized by a localized electrical discharge supported by a pulsed injection of an inert gas (He or Ar) at high pressure (40 bar). The metal atoms, sputtered from the target, aggregate in the source cavity to form metal clusters; the mixture of clusters and

inert gas expands through a nozzle forming a supersonic beam into an expansion chamber kept at a pressure of about 10-6 mbar. Electrically neutral nanoparticles exiting the PMCS are aerodynamically accelerated in a highly collimated beam with divergence lower than 1° and with a kinetic energy of roughly 0.5 eV • atom-1. The central part of the cluster beam enters, through a skimmer, a second vacuum chamber (deposition chamber) where the beam is intercepted by the polymeric substrate. By means of a stencil mask and substrate rastering in the plane perpendicular to the cluster beam (see Figure 1b), it is possible to homogenously implant gold nanoparticles into the target polymer with the required pattern.
In this way, a fully stretchable and conductive pattern is obtained on the surface[56], as shown in Figure 1b. The amount of nanoparticles implanted is measured in term of equivalent thickness (*teq*), defined as the thickness of a film made by an equivalent amount of nanoparticles deposited onto a rigid substrate. In this case, devices have been fabricated with *teq* = 81,5 } 3 nm. SCBI has been demonstrated as an effective method for the microfabrication of stretchable conductive circuits on PDMS[57], since it is applicable at room temperature (without any heating of the samples) and does not induce any charging or carbonization of the polymeric substrate.
Then, the nanoparticle paths are sealed to external wires by means of a layer of nickelgraphite filled silicone adhesive (Sol-08, Soliani EMC, Italy) cured at room temperature for 12 hours. These soft contacts ensure both high conductivity and elasticity also in the connecting region of the patterned surface to the external measuring circuitry (depicted in Figure 1c). Finally, the whole surface is protected and electrically insulated with a 200 μm thick film of soft elastomer (EcoflexR 00-30, Smooth-on Inc, USA), as sketched in Figure 1d, deposited by spin coating at 500 rpm for 60 seconds and successive curing at room temperature for 12 hours. The final device is shown in Figure 2a.

Read-out electronic system

The device is connected to an external custom made printed circuit board (PCB), where the conditioning and the signal elaboration circuitry is embedded (see Figure 2b for the schematic electrical circuit) and the signal acquisition is performed by a PSoC3 (Programmable System on Chip CY8C3866AXI-040 from Cypress Semiconductor Corporation , San Jose, CA, USA). Regarding the optical system, both the IR Led and the phototransistor are biased by means of variable resistors, in order to tune the emitting light intensity and the receiver collector voltage, respectively. Moreover, it is possible to vary the sensitivity of optical system. The phototransistor can be biased at different collector-to-emitter voltages V_0, and at lower bias

voltages, the sensitivity is higher (see SI for addition details). This lets the system to adapt the response to different scenarios, where a lower or a higher sensitivity could be useful. To improve the system performance, a differential mode signal treatment is adopted. The photodiode is biased with a pulse wave, with a duty cycle of 2% at frequency of 20 Hz. For each cycle, the output signal is given by the difference between the collector voltage with and without the emitted diode light (i.e. before and the end of the pulse wave biasing the diode, respectively). This strategy avoids losing any information and has two main advantages. First of all, the pulse length (1 ms) allows to filter the low frequency noise of the diode current, such as the random telegraph signal (RTS) noise usually due to trapping-detrapping phenomena, which affects the emitted light and, by consequence, the system output signal. The second advantage is the possibility to implement a differential read-out strategy, in order to cancel the environmental light variations that may cause interferences on the output signal. Regarding the resistive strain gauge, it is connected in a voltage divider with a 10 kΩ resistor and acquired by reading the drop voltage on it. In the case of the bending experiments with a cantilever configuration (shown in SI), a capacitive linear accelerometer (LIS2L02AL, STMicroelectronics Inc., Geneva, CH) is connected to the same PCB. The output voltages, together with the accelerometer outputs in the case of cantilever experiments, are collected and elaborated by a 32-bit PIC (PIC32MX460F512L, Microchip Technology Inc., Chandler, AZ, USA) microcontroller and transmitted to a PC by means of USB communication. Finally, the whole system is controlled by a custom made graphical user interface (GUI).

Results and discussion

For characterizing the system response to external applied pressure, the device is fixed on a rigid surface, and it is indented in the middle of the non-implanted (upper) surface, as depicted in Figure 3a. First, a DelrinR probe with flat head (8 mm × 8 mm) is aligned to the center of the sensing area by means of three orthogonal manual micrometric translational stages with crossed roller bearing (M-105.10, PI, Karlsruhe, Germany); then, indentation of the loading probe in the normal direction is obtained by means of a servo-controlled micrometric translational stage (M-111.1, PI, Karlsruhe, Germany). At its opposite side, the probe is mechanically interfaced to a 6-components load cell (ATI NANO 17 SI-25-0.25, Apex, NC, USA) capable of recording the indentation force applied to the soft sensing body (the acquisition frequency is 20 Hz). The probe is indented into the soft body at a constant velocity of 0.05 mm/s and 1 mm/s for quasi-statical and load-unload characterizations, respectively, gradually increasing the displacement and then the applied load. With this set-up,

a positive variation of the phototransistor output signal occurs, while a null resistance variation of the gold nanoparticle paths is observed.

The results are shown in Figure 3b, with a pressure up to 250 kPa. The optical output signal is given by the variation of V_{ce}. In particular, we consider the normalized voltage variation $\Delta V/V_0$, with V_0 the V_{ce} bias voltage of the phototransistor. In the same plot, different signal variations of the optical system are depicted, with V_0 tuned from 0.5 to 2 V. As shown, the signal amplitude is much larger for lower values of V_0, demonstrating the possibility to adjust the sensitivity in a relevant way. While the configuration with $V_0 = 0.5$ V is the most efficient, higher bias voltages could be used if we are interested in filtering lower pressure stimulations. For instance, we could trigger an actuator at a certain pressure level without introducing any other electronic/logical element, whose integration could be difficult in a soft robot. Moreover, in Figure 3c the typical time response of both signals under load-unload cycles is shown. For this example, the bias voltage is put to V_0= 1 V, and the indenter is cyclically load and unload, simulating a pressure square function and applying for each cycle a maximum pressure of50 kPa.

Instead, in the case of bending, both optical and resistive signals vary. If the bending stretches the implanted surface (positive bending) the resistance variation is positive; otherwise, in the case of compression (negative bending) the variation is negative (see Figure 4). By contrast, the optical variation is always positive, since any mechanical deformation lowers the incident light on the receiver. In order to bend the device in a precise and repeatable way, the device is installed on a thin metallic support by means of Parafilm strip in order to ensure both adhesion and flexibility to the device. Then, the metallic strip is clamped to a fixed mechanical support at one extremity, while the other end is clamped to a servo-controlled precision translation stage (M-126.CG1, PI, Karlsruhe, Germany), whose movement causes the bending of the metallic strip and the device fixed over it.

Conventionally, positive or negative bending is caused by a positive or negative moment, respectively, while the vertical deflection has the opposite sign. For small deflections, the curved profile can be approximated with a circular arc. Given the strip length $L = 70$ mm and the vertical deflection h it is possible to find the strain ε as

$$\varepsilon = -\frac{\bar{y}}{r} \simeq -\frac{4\bar{y}}{L^2}h = -\frac{2t}{L^2}h\,, \tag{1}$$

where $\bar{y}$ = t/2 is the vertical distance of the neutral axis to the implanted surface. Since the device thickness t is much higher with respect to those of the strip, the neutral axis is positioned nearly the middle of the device. Noticeably, while the relation between the strain

and the lateral compression Δx is highly non-linear (see SI for detailed calculations), the strain vs. vertical deflection characteristic becomes linear. Finally, considering the relative resistance variation $\Delta R/R_0 = \alpha\varepsilon$,

$$\frac{\Delta R}{R_0} = -2\alpha \frac{t}{L^2} h \,, \tag{2}$$

The quasi-static characteristics of output signals vs. vertical deflection h is shown in Figure 4b. The optical signal variation (blue solid curve) is positive for both positive and negative vertical deflections, while the resistance variation (red solid curve) follows Equation (2) (black dashed line), with $\alpha_p \simeq 24$ and $\alpha_n \simeq 12.5$ for positive and negative bending, respectively. This different value can be due to the different rearrangement of nanoparticle clusters during compression or extension. Figure 4d and 4f show the time response of output signals due to bending/unbending cycles. In particular, panel d) shows the response to negative bending cycles. For each cycle, the system starts from the flat configuration (depicted in Figure 4a), it reaches a maximum vertical deflection of 5 mm, and then it comes back to the initial flat condition. Instead, panel f) shows the response to positive bending cycles, where at each cycles the maximum deflection is of -5 mm. It can be noted that the optical signal has a positive variation in both cases, while the resistive variation is positive or negative according to the bending direction. Finally, for analyzing the hysteresis in bending/unbending cycles, the behavior of output signals vs. vertical deflection is shown in Supplementary Information (see Figure S7 and S8 for negative and positive bending/unbending cycles, respectively). We can also note a good repeatability and a fast response to the mechanical stimulation.

To demonstrate the multimodal capabilities of the system and its possible application in soft robotics, the two previous experimental setups have been combined. In particular, the setup used for pressure characterization, composed by the load cell and the flat indenter mounted on the precision vertical stage, is positioned above the bending system described above, as sketched in Figure 5a.

First of all, the capability of distinguish sequential stimulations is tested, and the result is shown in Figure 5b. In phase I, the sample, starting from a flat configuration, is bent negatively, without coming in contact with the indenter placed over it. This bending causes an increase of the optical output signal (blue solid line) and a negative resistance variation (red solid line). Then, in phase II, the indenter is cyclically moved vertically upwards and downwards, stimulating the bent device with load-unload cycles. The applied pressure is measured by the load cell (shown in black dashed line). As expected, during this phase the

optical signal presents an additional variation, in phase with the applied pressure , while the resistance change is null. Finally, in phase III the cyclical vertical indentation is stopped, and the sample is released from bending, recovering initial values for both output signals. Observing this behavior, we can combine the two signals in such a way to enhance only the variation due to the external pressure, cancelling the contribution due to bending. In particular, defining

$$S = \frac{\Delta V}{V_0} + k\frac{\Delta R}{R_0} \quad (3)$$

we could find the optimal k value in order to have an almost null S value in case of pure bending. The combined output signal, with k = 2.3, is shown in Figure 5b (green solid line). We can note that the signal S has a positive variation only when the external force (black dashed line) is applied. Instead, as already shown in Equation (2), the bending is proportional only to the resistance variation. Then, using Equation (2) and (3), we can distinguish clearly between the two different mechanical stimulations, and measure them.

In order to further demonstrate the effectiveness of this strategy, also simultaneous mechanical stimulations are investigated. The results are shown in Figure 6. In this case, the indenter is put close to the sample surface. Then, when performing bending/unbending cycles, the sample hits the indenter (connected to the load cell) for a fraction of each cycle. In the non-contact phase, both output signal vary, as shown in Figure 6a. Instead, in the contact phase, the optical signal presents a very large variation (blue solid line), while the resistance change is almost null, being affected only by bending. The corresponding combined output signal (calculated with the same previous value for k) is shown in Figure 6b (green solid line), and it matches the pressure measured by the load cell (black dashed line). Then, also in this case, by exploiting Equation (2) and (3) it is possible to discriminate and measure bending and pressure.

Conclusion

In conclusion, we presented a multimodal mechanosensing system where the sensing elements can be embedded in a soft body during its initial molding. Thanks to SCBI process, the addition of sensing items to the system does not change the mechanical properties of the bulk material (in this case PDMS). This solution is particularly desired in the field of wearable systems and in the fabrication of soft robots with sensing capabilities. In particular, we demonstrated how, combining the optical and the resistive outputs in a proper (but very simple) way, the proposed system can detect and distinguish different stimuli, such as strain

related to bending and external pressure. While pressure is strictly related to exteroception, bending is typical proprioceptive information. We believe that this is a key enabling technology for building future multimodal soft robots. Indeed, as mentioned in the introduction, to our knowledge the only example of soft robot with both proprioceptive and exteroceptive capabilities is presented by Larson *et al[12]*. However, in that case the discrimination of simultaneous pressure/bending stimulation was not demonstrated.

The aim of this work was to demonstrate the effectiveness of a novel strategy for multimodal sensing in soft robotics. Several aspects remain to be properly studied and analyzed in future works. For instance, how the responses of both electro and optical mechanisms would change in the case of integration in an entirely soft body, or if a pneumatic actuator is embedded in a soft robot or in a gripper. Also, the dependence of the output signals on the characteristics of a contacting object (i.e. its shape and dimensions, if it is optically reflective or not) should be analyzed. Finally, here we considered movements only in a 2D plane, while soft robots will move in the 3D space. Then, this sensing strategy should be generalized in order to reconstruct 3D deformations and movements.

Given the promising results at component level, the presented approach can be further investigated in the near future at robotic level to evaluate its potential during the movement and exploration of a soft robot, without needing unwieldy wiring and distributed conditioning circuits that nowadays are the main technological limits in this field.

Author disclosure statements

No competing financial interests exist

References

1. Rus D., Tolley M. T. Design, fabrication and control of soft robots. Nature. 2015; 521 (7553): 467.

2. Laschi C., Soft robotics research, challenges, and innovation potential, through showcases. In *Soft Robotics*, Springer: 2015; pp 255.

3. Paik J., Soft components for soft robots. In *Soft Robotics*, Springer: 2015; pp 272.

4. Lu N., Kim D.-H. Flexible and stretchable electronics paving the way for soft robotics. Soft Robotics. 2014; 1 (1): 53.

5. Shepherd R. F., Ilievski F., Choi W., Morin S. A., Stokes A. A., Mazzeo A. D., Chen X., Wang M., Whitesides G. M. Multigait soft robot. Proceedings of the National Academy of Sciences. 2011; 108 (51): 20400.

6. Suzumori K., Endo S., Kanda T., Kato N., Suzuki H. In *A Bending Pneumatic Rubber Actuator Realizing Soft-bodied Manta Swimming Robot*, Proceedings 2007 IEEE International Conference on Robotics and Automation, 10-14 April 2007; **2007**; pp 4975.

7. Trimmer B. Soft robots. Current Biology. 2013; 23 (15): R639.

8. Kim S., Laschi C., Trimmer B. Soft robotics: a bioinspired evolution in robotics. Trends in Biotechnology. 2013; 31 (5): 287.

9. Iida F., Laschi C. Soft Robotics: Challenges and Perspectives. Procedia Computer Science. 2011; 7 (0): 99.

10. Case J. C., White E. L., Kramer R. K. Soft Material Characterization for Robotic Applications. Soft Robotics. 2015; 2 (2): 80.

11. Beccai L., Lucarotti C., Totaro M., Taghavi M., Soft Robotics Mechanosensing. In *Soft Robotics: Trends, Applications and Challenges: Proceedings of the Soft Robotics Week, April 25-30, 2016, Livorno, Italy*, Laschi, C.; Rossiter, J.; Iida, F.; Cianchetti, M.; Margheri, L., Eds. Springer International Publishing: Cham, 2017; pp 11.

12. Larson C., Peele B., Li S., Robinson S., Totaro M., Beccai L., Mazzolai B., Shepherd R. Highly stretchable electroluminescent skin for optical signaling and tactile sensing. Science. 2016; 351 (6277): 1071.

13. Xu S., Zhang Y., Jia L., Mathewson K. E., Jang K.-I., Kim J., Fu H., Huang X., Chava P., Wang R., Bhole S., Wang L., Na Y. J., Guan Y., Flavin M., Han Z., Huang Y., Rogers J. A. Soft microfluidic assemblies of sensors, circuits, and radios for the skin. Science. 2014; 344 (6179): 70.

14. Park Y.-L., Chen B.-R., Wood R. J. Design and fabrication of soft artificial skin using embedded microchannels and liquid conductors. Sensors Journal, IEEE. 2012; 12 (8): 2711.

15. Laflamme S., Kollosche M., Connor J. J., Kofod G. Soft capacitive sensor for structural health monitoring of large-scale systems. Structural Control and Health Monitoring. 2012; 19 (1): 70.
16. Majidi C., Kramer R., Wood R. J. A non-differential elastomer curvature sensor for softer-than-skin electronics. Smart Mater. Struct. 2011; 20: 7.
17. Mannsfeld S. C. B., Tee B. C. K., Stoltenberg R. M., Chen C. V. H. H., Barman S., Muir B. V. O., Sokolov A. N., Reese C., Bao Z. Highly sensitive flexible pressure sensors with microstructured rubber dielectric layers. Nat Mater. 2010; 9 (10): 859.
18. Amjadi M., Pichitpajongkit A., Lee S., Ryu S., Park I. Highly Stretchable and Sensitive Strain Sensor Based on Silver Nanowire–Elastomer Nanocomposite. ACS Nano. 2014; 8 (5): 5154.
19. Wang J., Jiu J., Nogi M., Sugahara T., Nagao S., Koga H., He P., Suganuma K. A highly sensitive and flexible pressure sensor with electrodes and elastomeric interlayer containing silver nanowires. Nanoscale. 2015; 7 (7): 2926.
20. Jang H., Park Y. J., Chen X., Das T., Kim M.-S., Ahn J.-H. Graphene-Based Flexible and Stretchable Electronics. Advanced Materials. 2016: n/a.
21. Jeong Y. R., Park H., Jin S. W., Hong S. Y., Lee S.-S., Ha J. S. Highly stretchable and sensitive strain sensors using fragmentized graphene foam. Advanced Functional Materials. 2015; 25 (27): 4228.
22. Yan C., Wang J., Kang W., Cui M., Wang X., Foo C. Y., Chee K. J., Lee P. S. Highly Stretchable Piezoresistive Graphene–Nanocellulose Nanopaper for Strain Sensors. Advanced Materials. 2014; 26 (13): 2022.
23. Lipomi D. J., Vosgueritchian M., Tee B. C. K., Hellstrom S. L., Lee J. A., Fox C. H., Bao Z. Skin-like pressure and strain sensors based on transparent elastic films of carbon nanotubes. Nat Nano. 2011; 6 (12): 788.
24. Wichmann M. H. G., Buschhorn S. T., Boger L., Adelung R., Schulte K. Direction sensitive bending sensors based on multi-wall carbon nanotube/epoxy nanocomposites. Nanotechnology. 2008; 19 (47): 475503.
25. Gong S., Schwalb W., Wang Y., Chen Y., Tang Y., Si J., Shirinzadeh B., Cheng W. A wearable and highly sensitive pressure sensor with ultrathin gold nanowires. Nat Commun. 2014; 5.
26. Sekitani T., Zschieschang U., Klauk H., Someya T. Flexible organic transistors and circuits with extreme bending stability. Nat Mater. 2010; 9 (12): 1015.
27. Someya T., Kato Y., Sekitani T., Iba S., Noguchi Y., Murase Y., Kawaguchi H.,

Sakurai T. Conformable, flexible, large-area networks of pressure and thermal sensors with organic transistor active matrixes. Proceedings of the National Academy of Sciences of the United States of America. 2005; 102 (35): 12321.

28. Schwartz G., Tee B. C. K., Mei J., Appleton A. L., Kim D. H., Wang H., Bao Z. Flexible polymer transistors with high pressure sensitivity for application in electronic skin and health monitoring. Nat Commun. 2013; 4: 1859.

29. Viry L., Levi A., Totaro M., Mondini A., Mattoli V., Mazzolai B., Beccai L. Flexible three-axial force sensor for soft and highly sensitive artificial touch. Advanced Materials. 2014; 26 (17): 2659.

30. Castano L. M., Flatau A. B. Smart fabric sensors and e-textile technologies: a review. Smart Materials and Structures. 2014; 23 (5): 053001.

31. Syduzzaman M., Patwary S. U., Farhana K., Ahmed S. Smart textiles and nanotechnology: a general overview. Journal of Textile Science & Engineering. 2015; 5 (1): 1.

32. Chou H.-H., Nguyen A., Chortos A., To J. W. F., Lu C., Mei J., Kurosawa T., Bae W.-G., Tok J. B. H., Bao Z. A chameleon-inspired stretchable electronic skin with interactive colour changing controlled by tactile sensing. Nat Commun. 2015; 6.

33. Park J. W., Jang J. Fabrication of graphene/free-standing nanofibrillar PEDOT/P(VDF-HFP) hybrid device for wearable and sensitive electronic skin application. Carbon. 2015; 87: 275.

34. Park J., Lee Y., Hong J., Lee Y., Ha M., Jung Y., Lim H., Kim S. Y., Ko H. Tactiledirection-sensitive and stretchable electronic skins based on human-skin-inspired interlocked microstructures. ACS nano. 2014; 8 (12): 12020.

35. Kim D.-H., Lu N., Ma R., Kim Y.-S., Kim R.-H., Wang S., Wu J., Won S. M., Tao H., Islam A., Yu K. J., Kim T.-i., Chowdhury R., Ying M., Xu L., Li M., Chung H.-J., Keum H., McCormick M., Liu P., Zhang Y.-W., Omenetto F. G., Huang Y., Coleman T., Rogers J. A. Epidermal electronics. Science. 2011; 333 (6044): 838.

36. Shao Q., Niu Z., Hirtz M., Jiang L., Liu Y., Wang Z., Chen X. High-Performance and Tailorable Pressure Sensor Based on Ultrathin Conductive Polymer Film. Small. 2014; 10 (8): 1466.

37. Webb R. C., Bonifas A. P., Behnaz A., Zhang Y., Yu K. J., Cheng H., Shi M., Bian Z., Liu Z., Kim Y.-S., Yeo W.-H., Park J. S., Song J., Li Y., Huang Y., Gorbach A. M., Rogers J. A. Ultrathin conformal devices for precise and continuous thermal characterization of human skin. Nat Mater. 2013; 12 (10): 938.

38. Kaltenbrunner M., Sekitani T., Reeder J., Yokota T., Kuribara K., Tokuhara T., Drack

M., Schwodiauer R., Graz I., Bauer-Gogonea S., Bauer S., Someya T. An ultra-lightweight design for imperceptible plastic electronics. Nature. 2013; 499 (7459): 458.

39. Yuen M., Cherian A., Case J. C., Seipel J., Kramer R. K. In *Conformable actuation and sensing with robotic fabric*, Intelligent Robots and Systems (IROS 2014), 2014 IEEE/RSJ International Conference on, 14-18 Sept. 2014; **2014**; pp 580.

40. Leonov V. Thermoelectric energy harvesting of human body heat for wearable sensors. Sensors Journal, IEEE. 2013; 13 (6): 2284.

41. Nesenbergs K., Selavo L. In *Smart textiles for wearable sensor networks: Review and early lessons*, Medical Measurements and Applications (MeMeA), 2015 IEEE International Symposium on, IEEE: **2015**; pp 402.

42. Kong J.-H., Jang N.-S., Kim S.-H., Kim J.-M. Simple and rapid micropatterning of conductive carbon composites and its application to elastic strain sensors. Carbon. 2014; 77 (0): 199.

43. Lee J., Kwon H., Seo J., Shin S., Koo J. H., Pang C., Son S., Kim J. H., Jang Y. H., Kim D. E., Lee T. Conductive Fiber-Based Ultrasensitive Textile Pressure Sensor for Wearable Electronics. Advanced Materials. 2015; 27 (15): 2433.

44. Gerratt A. P., Michaud H. O., Lacour S. P. Elastomeric Electronic Skin for Prosthetic Tactile Sensation. Advanced Functional Materials. 2015; 25 (15): 2287.

45. Kim S. Y., Park S., Park H. W., Park D. H., Jeong Y., Kim D. H. Highly sensitive and multimodal all-carbon skin sensors capable of simultaneously detecting tactile and biological stimuli. Advanced Materials. 2015; 27 (28): 4178.

46. Park J., Lee Y., Hong J., Ha M., Jung Y.-D., Lim H., Kim S. Y., Ko H. Giant tunneling piezoresistance of compositeelastomers with interlocked microdome arrays for ultrasensitive and multimodal electronic skins. ACS nano. 2014; 8 (5): 4689.

47. Engel J., Nannan C., Tucker C., Chang L., Sung-Hoon K., Jones D. In *Flexible multimodal tactile sensing system for object identification*, Sensors, 2006. 5th IEEE Conference on, 22-25 Oct. 2006; **2006**; pp 563.

48. Lucarotti C., Totaro M., Sadeghi A., Mazzolai B., Beccai L. Revealing bending and force in a soft body through a plant root inspired approach. Scientific Reports. 2015; 5: 8788.

49. Cianchetti M., Renda F., Licofonte A., Laschi C. In *Sensorization of continuum soft robots for reconstructing their spatial configuration*, Biomedical Robotics and Biomechatronics (BioRob), 2012 4th IEEE RAS & EMBS International Conference on, 24-27 June 2012; **2012**; pp 634.

50. Chossat J.-B., Shin H.-S., Park Y.-L., Duchaine V. Soft Tactile Skin Using an

Embedded Ionic Liquid and Tomographic Imaging. Journal of Mechanisms and Robotics. 2015; 7 (2): 021008.

51. Park S., Kim H., Vosgueritchian M., Cheon S., Kim H., Koo J. H., Kim T. R., Lee S., Schwartz G., Chang H. Stretchable energy-harvesting tactile electronic skin capable of differentiating multiple mechanical stimuli modes. Advanced Materials. 2014; 26 (43): 7324.

52. Ge J., Sun L., Zhang F.-R., Zhang Y., Shi L.-A., Zhao H.-Y., Zhu H.-W., Jiang H.-L., Yu S.-H. A Stretchable Electronic Fabric Artificial Skin with Pressure-, Lateral Strain-, and Flexion-Sensitive Properties. Advanced Materials. 2016; 28 (4): 722.

53. Ramuz M., Tee B. C. K., Tok J. B. H., Bao Z. Transparent, Optical, Pressure-Sensitive Artificial Skin for Large-Area Stretchable Electronics. Advanced Materials. 2012; 24 (24): 3223.

54. Levi A., Piovanelli M., Furlan S., Mazzolai B., Beccai L. Soft, Transparent, Electronic Skin for Distributed and Multiple Pressure Sensing. Sensors. 2013; 13 (5): 6578.

55. Zhao H., O'Brien K., Li S., Shepherd R. F. Optoelectronically innervated soft prosthetic hand via stretchable optical waveguides. Science Robotics. 2016; 1 (1).

56. Corbelli G., Ghisleri C., Marelli M., Milani P., Ravagnan L. Highly Deformable Nanostructured Elastomeric Electrodes With Improving Conductivity Upon Cyclical Stretching. Advanced Materials. 2011; 23 (39): 4504.

57. Borghi F., Melis C., Ghisleri C., Podesta A., Ravagnan L., Colombo L., Milani P. Stretchable nanocomposite electrodes with tunable mechanical properties by supersonic cluster beam implantation in elastomers. Applied Physics Letters. 2015; 106 (12): 121902.

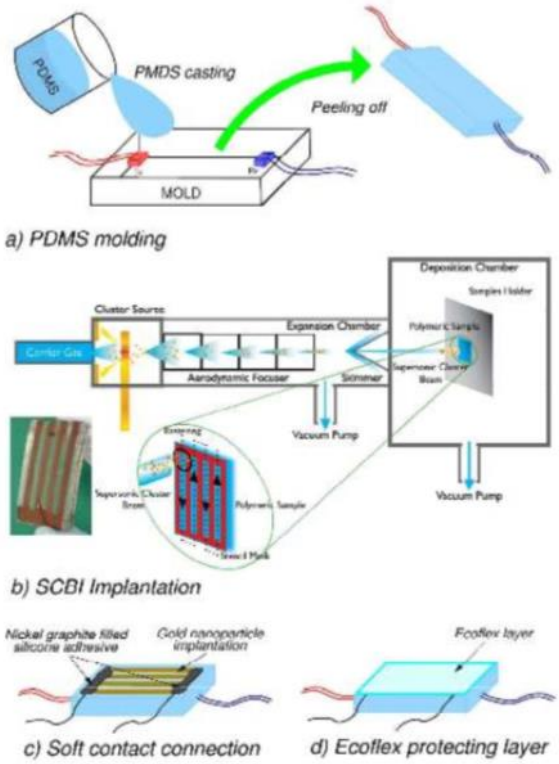

Figure 1. Fabrication process of the device. a) PDMS molding for making the bulk body with embedded optical elements. b) Supersonic cluster beam process for the implantation of gold nanoparticle-based resistive strain gauge, with the implanted surface shown in the inset. c) Soft contact connection to external wires of the implanted strain gauge by means of a nickel graphite filled silicone adhesive. d) Insulation and protection of the implanted surface with a thin Ecoflex® layer deposited by spin coating.

252x343mm (300 x 300 DPI)

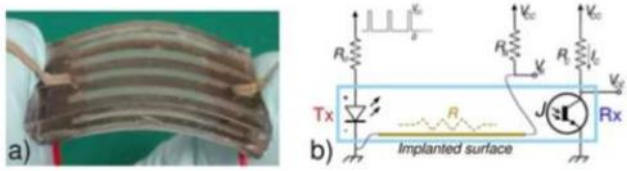

Figure 2. a) Photograph of the final device. b) Electrical schematization of the sensing system with its conditioning and read-out circuitry.

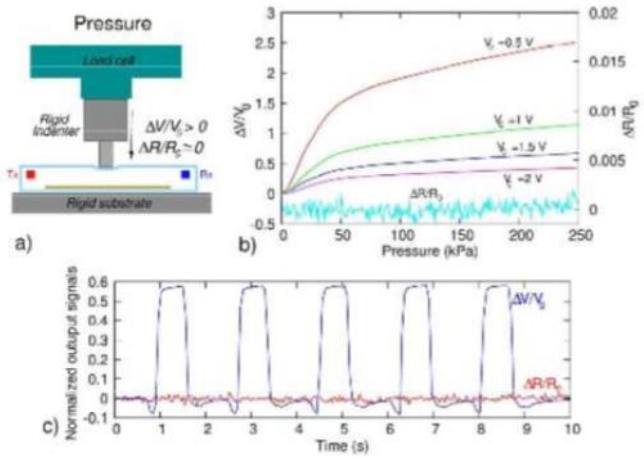

Figure 3. Response to applied pressure. a) Scheme of the experimental setup with the sensing system fixed on a rigid surface. The device is stimulated with a rigid flat square indenter, connected to a load cell, by means of a motorized vertical translation stage. b) Output characteristics of the sensing system versus applied pressure. Different optical outputs are shown, with V0 spanning from 0.5 V to 2 V, demonstrating the tunable sensitivity of the system. In this case, the resistive output signal is null. c) Output signals for load/unload cycles, with an applied pressure around 50 kPa and V_0 = 1 V.

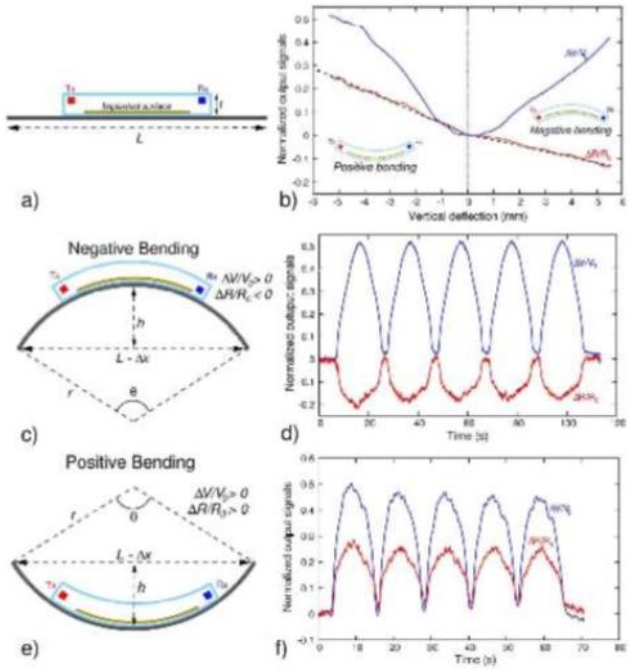

Figure 4. Response to negative/positive bending. a) The device is fixed on a thin metallic strip of length L=70 mm, and bent by means of an horizontal translation stage connected to one extremity of the strip, with the other fixed. b) Output characteristics of the optical (solid blue line) and resistive (red solid line) signals versus vertical deflection h. Schematics (c) and output signals (d) for load/unload cycles for negative bending, with vertical deflection around 5 mm. In this case, the optical signal is positive, while the resistive output is negative. Schematics (e) and output signals (f) for load/unload cycles for positive bending, with vertical deflection around -5 mm. In this case, both optical and resistive signals are positive.

198x210mm (300 x 300 DPI)

v

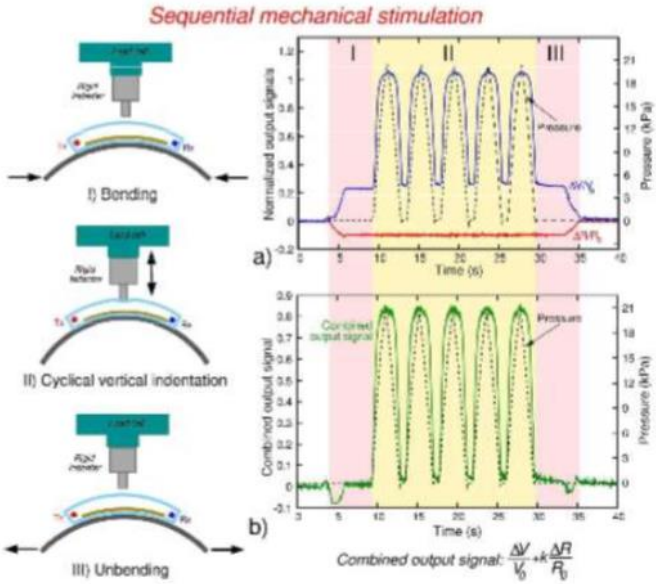

Figure 5. Sequential stimuli detection. a) Output signals under sequential mechanical stimulation. In phase I) the device is bent, without hitting the indenter placed above it. During this phase, both optical (blue solid line) and resistive (red solid line) signals varies. In phase II) the indenter is moved cyclically in the vertical direction, applying a load/unload stimulations on the device. In this case, only the optical signal has a variation, in phase with the pressure measured by the load cell (black dashed line). b) Combined output signal (green solid line), proportional to the measured pressure (black dashed line).

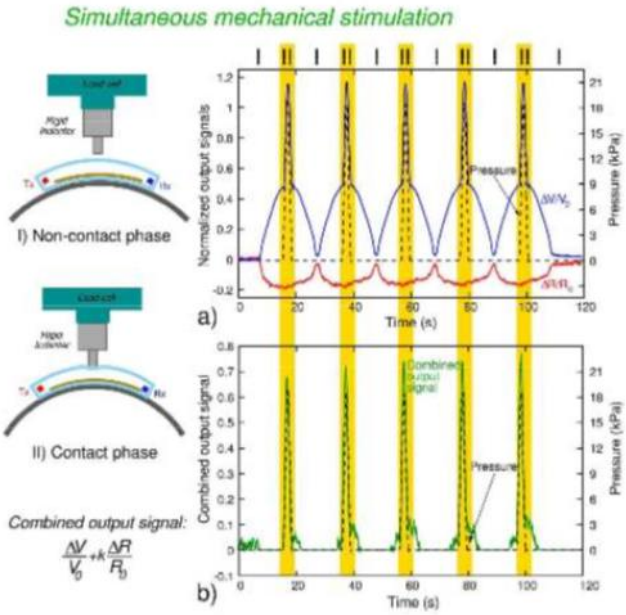

Figure 6. Simultaneous stimuli detection. a) Output signals under simultaneous mechanical stimulation. By means of bending/unbending cycles, the device hits the indenter for a fraction of each cycle. In non-contact phase (I) the device approaches the indenter placed above it. Here, both optical (blue solid line) and resistive (red solid line) signals varies. In contact phase (II) the device hits the indenter, causing a pressure on its upper surface. In this case, only the optical signal has a variation, in phase with the pressure measured by the load cell (black dashed line). b) Combined output signal (green solid line), proportional to the measured pressure (black dashed line).

Supporting Information

Integrated simultaneous detection of tactile and bending cues for soft robotics

Massimo Totaro, Alessio Mondini, Andrea Bellacicca, Paolo Milani, Lucia Beccai

1. Tunable sensitivity of the optical system

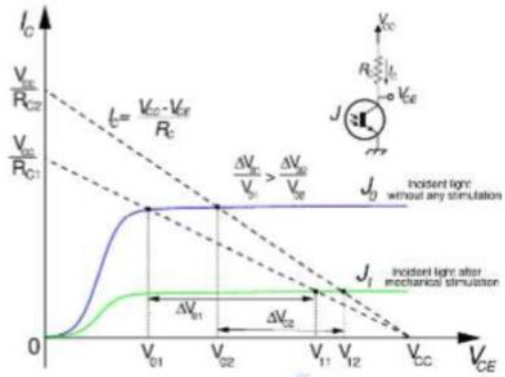

Figure S1. Tunable sensitivity of the optical system

In Figure S1 the tunable sensitivity of the optical system is explained. Indeed, supposing J_0 the incident light without any stimulation, with the phototransistor polarized in the active region, the incident light after a mechanical stimulation is $J_1 < J_0$, with a consequent lower output current I_c. Since the working point lies on the load line (dashed line in the graph), the same light intensity variation causes a larger output V_{CE} variation for lower V_0. Then, the ratio $\Delta V_{CE}/V_0$ can be varied by tuning V_0, with higher values for lower V_0.

2. Bending characteristic equations

Starting from the device in a flat configuration, depicted in Figure 4a, the horizontal linear stage bend the system as sketched in Figure 4c (negative bending) or 4e (positive bending). Considering the curve profile as a circular arc of length L, and the curvature angle $\theta = L/r$, with r the curvature radius, the vertical deflection is

$$h = r\left[1 - \cos\frac{\theta}{2}\right] = \frac{L}{\theta}\left[1 - \cos\frac{\theta}{2}\right]. \quad \text{(S2)}$$

Then, expanding the cosine in Taylor's series at the second order ($\cos\theta/2 \simeq 1 - \theta^2/4$), we obtain $h \simeq L\theta/4$.

The strain is

$$\varepsilon = -\frac{\bar{y}}{r} = -\frac{t}{2}\frac{\theta}{L} \simeq -\frac{2t}{L^2}h\,, \quad \text{(S3)}$$

with t the thickness of the body and $\bar{y} = t/2$ the distance from the neutral axis.

Finally,

$$\frac{\Delta R}{R_0} = \alpha\varepsilon \simeq -\alpha\frac{2t}{L^2}h. \quad \text{(S4)}$$

3. Cantilever configuration

Considering a cantilever configuration of the system, it is possible to predict the resistance variation as a function of the maximum bending angle θ_{max} of the free end. Indeed, the strain ε on the surface is

$$\varepsilon = \frac{\pi}{360}\frac{t}{L}\theta_{max} \quad \text{(S5)}$$

with t and L the thickness and the length of the body, respectively. In addition, supposing a linear resistance variation of the strain gauge $\Delta R/R_0 = \alpha\varepsilon$, we obtain

$$\frac{\Delta R}{R_0} = \frac{\pi}{360}\frac{t}{\alpha L}\theta_{max} \quad \text{(S6)}$$

In Figure S7 the experimental results of the system under bending are shown. In this case, the system is mounted in a cantilever configuration, and the angle is measured by means of a biaxial accelerometer attached on the free extremity. As shown, the optical signal presents positive variations for both positive (upward bending) and negative (downward bending) angles. By contrast, the resistance varies positively or negatively for upward and downward bending, respectively. This is due to the different kind of strain (extensive and compressive, respectively) applied on the implanted surface during bending.

Moreover, for positive angles the behavior of the resistive device is quite linear, while for negative angles it presents some non-linearities. This is probably due to the fact that nanoimplanted clusters behave differently under compression and extension. Then, for positive angles, it is possible to predict quantitatively the applied bending, by means of Equation (S6). In Figure S7 the experimental data (red solid line) are compared with the

fitting of Equation (S6) (black dashed line), with a good agreement in the range -20°÷ 80°. In this case, with t = 5mm and L= 30 mm, the fitted value is $\alpha = 0.27$.

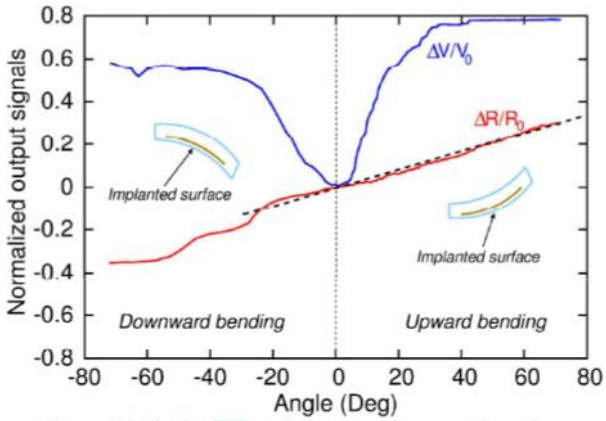

Figure S7. Output characteristics in cantilever configuration.

4. Hysteresis in bending/unbending cycles

In Figure S8, the hysteresis of output signals for negative bending/unbending cycles is shown. In particular, for the optical system, bending and unbending scans are depicted in blue and red solid lines, respectively. Instead, the resistance variation for bending and unbending scans is shown in green and violet solid lines, respectively.

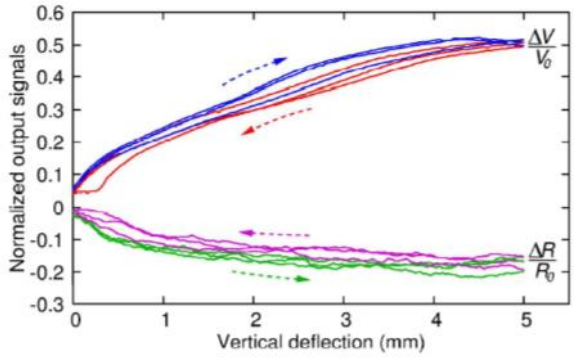

Figure S8. Output signals vs. vertical deflection for negative bending/unbending cycles.

The results for positive bending/unbending cycles are shown in Figure S9, using the same color code of Figure S8.

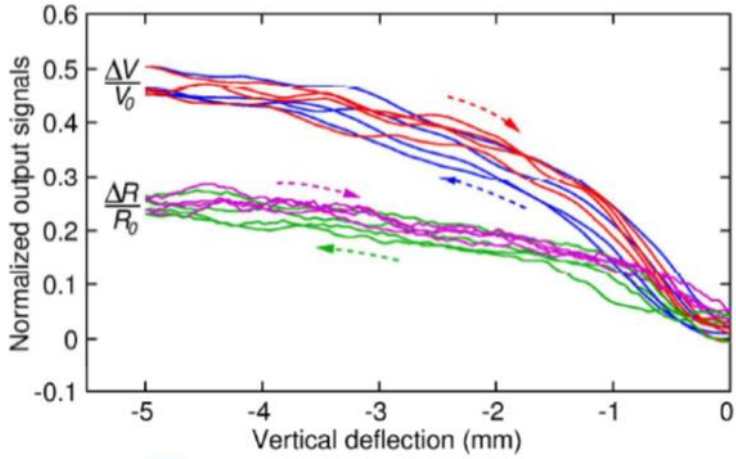

Figure S9. Output signals vs. vertical deflection for positive bending/unbending cycles.

6.4 Conclusions

This chapter described the possibility to exploit SCBI to fabricate smart materials starting from different substrates and how it is possible to incorporate them to obtain innovative hybrid devices. Two examples have been provided: a multilayer stretchable keyboard and a tactile/bending sensor.

Multilayer architectures are the most practical way to arrange electronic components on a board. Electrical connection among layers is assured by means of conductive vias. Fabricating stretchable conductive vias is demanding to integrate advanced features also in devices based on stretchable substrate. Up to now, this issue has been poorly addressed. Exploiting SCBI I have demonstrated the possibility to shape stretchable conductive vias also on soft substrate. I have realized a stretchable keyboard with a matrix architecture that requires two layers. I have fully exploited a set of rotating sample holders to fabricate both layers and vias within the same implantation process. I have tested the keyboard with several mechanical deformations showing that it maintains good electrical properties during the tests. Then I have addressed a second issue typical of stretchable electronics: how to bind standard rigid electronic with soft component. Our solution relies in using conductive electrodes printed on a paper substrate. While paper could be used coupled with standard electronic connectors, its softness takes in account for the mechanical deformation of the keyboard preserving the electrical links. I have also proved that resistors printed on paper with SCBI can be used to power a set of LEDs, limiting the flow of the current and avoiding the need for standard resistors, simplifying the circuit fabrication.

In the second device, SCBI have been used to fabricate conductive electrodes on a soft substrate. The electrical properties of the electrodes have been tailored to realize a pressure sensor, controlling the amount of nanoparticles

implanted in the polymeric matrix. The device is thus able to sense small deformations that cause measurable changes in the electrical properties of the electrodes. Coupling the electrodes with a standard optical sensor a hybrid pressure sensor that is able to discriminate mechanical deformations caused either by bending or by an external pressure exerted on it has been fabricated.

7 Conclusions

In this work, I have shown that supersonic cluster beam implantation/deposition is a robust technology for the fabrication of novel smart materials, systems, and devices with unique properties that can be exploited to complement and to extend the capabilities of standard electronic devices and micromechanical systems.

During my thesis work I have conducted a substantial upgrade of SCBI/SCBD set up, realizing an automatic and parallel system that allow the fabrication and characterization in situ of multiple samples. This set up have greatly enhanced the fabrication process: it reduces the time needed to obtain a large number of working samples, it permits large area implantation on different sides of the same sample and it permits the electrical characterization of several samples in real time.

SCBI coupled with this system has been used to fabricate micrometric thin conductive stretchable metal-polymer nanocomposites, able to sustain large mechanical deformation without significantly altering their elastic properties. At the same time, these systems exhibit good conductivity both at rest and when stretched. This has been exploited to obtain micrometric thin soft actuators than can be driven with voltage values lower than 1 kV. The actuators show good mechanical and electrical properties also for repeated actuation cycles (10000 cycles).

SCBD has been exploited to print passive electronic components (resistors, capacitors and super capacitors) on a paper substrate to deposit gold and carbon clusters with SCBD. Small circuits (low-pass, high pass filters and a wireless power storage/power supply system) have been realized combining printed electronic components.

The upgraded setup developed has been crucial to demonstrate how SCBI can be used to fabricate 3D conductive stretchable materials leading the way in the realization of full stretchable multi-layer electronic systems with high degree of complexity. So far, 3D stretchable conductive materials have been realized using several workarounds that never allowed for a real full stretchable conductive system. I have then exploited that to fabricate a multilayer stretchable capacitive keyboard that requires a complex architecture design: it is a standard for classical electronic system but it is challenging to implement with soft materials. This keyboard has been used as a platform to address another long-standing issue: how to make smart material-based components interact with classical electronic circuits.

I have also demonstrated how SCBI can be used to fabricate a smart material with sensing capabilities that directly integrates standard electronic components. This smart material has been exploited as a pressure sensor able to discriminate different mechanical deformations (strain caused by bending or external pressure). The behavior of this material is particularly desired in wearable systems or for soft robots: in fact, embedding sensing capabilities within a soft structure enable a robot to interact with an unstructured environment without the need for complex mechanical and software systems.

8 Bibliography

[1] L. Sha, S. Gopalakrishnan, X. Liu and Q. Wang, "Cyber-Physical Systems: A New Frontier," in *Machine Learning in Cyber Trust*, Springer, 2009, p. 3.

[2] S. S. Shipp, N. Gupta, B. Lal, J. A. Scott, C. L. Weber, M. Blake, S. F. M., S. Newsome and S. Thomas, "Emerging Global Trends in Advanced Manufacturing," Institute for defense analysis.

[3] Smart Clothes and Wearable Technology, Elsevier, 2009.

[4] J. M. Rabaey, "A Brand New Wireless Day," in *Proceedings of the 2008 Asia and South Pacific Design Automation Conference*, Seoul, Korea, 2008.

[5] C. Soh, Y. Yang and S. Bhalla, Smart Materials in Structural Health Monitoring, Control and Biomechanics, Springer, 20012.

[6] J. Brockgreitens and A. Abbas, "Responsive Food Packaging: Recent Progress and Technological Prospects," *Comprehensive Reviews in Food Science and Food Safety*, vol. 15, no. 1, p. 3, 2016.

[7] infosys, "The future of Maintenance," 2014. [Online]. Available: https://www.infosys.com/industries/aerospace-defense/white-papers/Documents/enabled-predictive-maintenance.pdf.

[8] P. Kamalinejad, C. Mahapatra, Z. Sheng, S. Mirabbasi, V. C. M. Leung and Y. L. Guan, "Wireless energy harvesting for the Internet of Things," *IEEE Communications Magazine* , vol. 53, no. 6, p. 102, 2015.

[9] K. David, D. Dixit and N. Jefferies, "2020 Vision," *IEEE Vehicular Technology Magazine*, vol. 5, no. 3, p. 22, 2010.

[10] D.-H. Kim, N. Lu, Y. Huang and J. A. Rogers, "Materials for stretchable electronics in bioinspired and biointegrated devices," *MRS Bulletin*, vol. 37, no. 3, p. 226, 2012.

[11] F. Carpi, I. Anderson, S. Bauer, G.Frediani, G. Gallone, M. Gei, C. Graaf, C. Jean-Mistral, W. Kaal, G. Kofod, M. Kollosche, R. Kornbluh, B. Lassen, M. Matysek, S. Michel, S. Nowak, B. O'Brien, Q. Pei, R. Pelrine, B. Rechenbach, S. Rosset and H. Shea, "Standards for dielectric elastomer transducers," *Smart Materials and Structure,* vol. 24, no. 10, p. 105025, 2015.

[12] S. Xu, Y. Zhang, J. Cho, J. Lee, X. Huang, L. Jia, J. A. Fan, Y. Su, J. Su, H. Zhang, H. Cheng, B. Lu, C. Yu, C. Chuang, T.-I. Kim, T. Song, K. Shigeta, S. Kang, C. Dagdeviren, I. Petrov, P. V. Braun, Y. Huang, U. Paik and J. A. Rogers, "Stretchable batteries with self-similar serpentine interconnects and integrated wireless recharging systems," *Nature Communications,* vol. 4, no. 1543, 2013.

[13] Z. Suo, "Mechanics of stretchable electronics and soft machines," *MRS Bulletin,* vol. 37, no. 3, p. 218, 2012.

[14] F. Carpi, G. Frediani, S. Turco and D. De Rossi, "Bioinspired Tunable Lens with Muscle-Like Electroactive Elastomers," *Advanced Functional Materials,* vol. 21, no. 21, p. 4152, 2011.

[15] L. Maffli, S. Rosset, M. Ghilardi, F. Carpi and H. Shea, "Ultrafast All-Polymer Electrically Tunable Silicone Lenses," *Advanced Functional Materials,* vol. 25, no. 11, p. 1656, 2015.

[16] M. A. Zwienieck, P. J. Melcher and N. M. Holbrook, "Hydrogel Control of Xylem Hydraulic Resistance in Plants," *Science,* vol. 291, no. 5506, p. 1059, 2001.

[17] D. J. Beebe, J. S. Moore, J. M. Bauer, Q. Yu, R. H. Liu, C. Devadoss and B.-H. Jo, "Functional hydrogel structures for autonomous flow control inside microfluidic channels," *Nature,* vol. 404, no. 6778, p. 588, 2000.

[18] C. Majidi, "Soft robotics: A perspective - current trends and prospective for the future," *Soft Robotics,* vol. 1, no. 1, p. 5, 2014.

[19] S. Bauer, S. Bauer-Gogonea, I. Graz, M. Kaltenbrunner, C. Keplinger and R. Schwödiauer, "25th Anniversary Article: A Soft Future: From Robots and Sensor Skin to Energy Harvesters," *Advanced Materials,* vol. 26, no. 1, p. 149, 2014.

[20] S. Rosset and H. R. Shea, "Small, fast and tough: shrinking down integrated elastomer transducers," *Applied Physics Reviews,* vol. 3, no. 3, p. 031105, 2016.

[21] R. F. Shepherd, F. Ilievski, W. Choi, S. A. Morin, A. A. Stokes, A. D. Mazzeo, X. Chen, M. Wang and G. M. Whitesides, "Multigait soft robot," *Proceedings of the National Academy of Sciences of the United States of America ,* vol. 108 , no. 51, p. 20400, 2011.

[22] R. V. Martinez, J. L. Branch, C. R. Fish, L. Jin, R. F. Shepherd, R. M. D. Nunes, Z. Suo and G. M. Whitesides, "Robotic Tentacles with Three-Dimensional Mobility," *Advanced Materials,* vol. 25, no. 2, p. 205, 2012.

[23] G. Frediani, D. Mazzei, D. E. D. Rossi and F. Carpi, "Wearable wireless tactile display for virtual interactions with soft bodies," *Frontiers in Bioengineering and Biotechnology,* vol. 2, 2014.

[24] H. A. Sonar and J. Paik, "Soft Pneumatic Actuator Skin with Piezoelectric Sensors for Vibrotactile Feedback," *Frontiers in Robotics and AI,* vol. 2, 2016.

[25] S. Shian, R. M. Diebold and D. R. Clarke, "Tunable lenses using transparent dielectric elastomer actuators," *Optic Express,* vol. 21, no. 7, p. 8669, 2013.

[26] M. Kollosche, S. Doering, J. Stumpe and G. Kofod, "Voltage-controlled compression for period tuning of optical surface relief gratings," *Optics Letters,* vol. 36, no. 8, p. 1389, 2011.

[27] J. Rossiter, B. Yap and A. Conn, "Biomimetic chromatophores for camouflage and soft active surfaces," *Bioninspiration & Biomimetics,* vol. 7, no. 3, p. 036009, 2012.

[28] A. Fishman, J. Rossiter and M. Homer, "Hiding the squid: patterns in artificial cephalopod skin," *Journal of the Royal Society Interface*, vol. 12, no. 108, 2015.

[29] L. Maffli and S. R. H. R. Shea, "Zipping dielectric elastomer actuators: characterization, design and modeling," *Smart Materials and Structures*, vol. 22, no. 10, p. 104013, 2013.

[30] E. C. Jensen, A. M. Stockton, T. N. Chiesl, J. Kim, A. Bera and R. A. Mathies, "Digitally programmable microfluidic automaton for multiscale combinatorial mixing and sample processing," *Lab on a Chip*, vol. 13, no. 2, p. 288, 2013.

[31] T. G. McKay, S. Rosset, I. A. Anderson and H. Shea, "Dielectric elastomer generators that stack up," *Smart Materials and Structures*, vol. 24, no. 1, p. 015014, 2015.

[32] R. Vertechy, G. P. P. Rosati and M. Fontana, "Reduced Model and Application of Inflating Circular Diaphragm Dielectric Elastomer Generators for Wave Energy Harvesting," *Journal of Vibration and Acoustics*, vol. 137, no. 1, p. 011004, 2015.

[33] P. P., W. Z., G. K. C., W. R. J. and W. C. J., "Soft robotic glove for combined assistance and at-home rehabilitation," *Robotics and Autonomous Systems*, vol. 73, p. 135, 2014.

[34] C. Laschi, M. Cianchetti, B. Mazzolai, L. Malgheri, M. Follador and P. Dario, "Soft Robot Arm Inspired by the Octopus," *Advanced robotics*, vol. 26, no. 7, p. 709, 2012.

[35] R. F. Shepherd, A. A. Stokes, J. Freake, J. Barber, P. W. Snyder, A. D. Mazzeo, L. Cademartiri, S. A. Morin and G. M. Whitesides, "Using Explosions to Power a Soft Robot," *Angewandte chemie*, vol. 52, no. 10, p. 2892, 2013.

[36] L. Ionov, "Hydrogel-based actuators: possibilities and limitations," *Materials Today*, vol. 17, no. 10, p. 494, 2014.

[37] S. Taccola, F. Greco, E. Sinibaldi, A. Mondini, B. Mazzolai and V. Mattoli, "Toward a New Generation of Electrically Controllable Hygromorphic Soft Actuators," *Advanced Materials*, vol. 27, no. 10, p. 1668, 2015.

[38] A. C. Siegel, S. T. Phillips, M. D. Dickey, N.Lu, Z. Suo and G. M. Whitesides, "Foldable Printed Circuit Boards on Paper Substrates," *Advanced Functional Materials*, vol. 20, no. 1, p. 28, 2010.

[39] J. P. Rolland and D. A. Mourey, "Paper as a novel material platform," *MRS Bulletin*, vol. 38, no. 4, p. 299, 2013.

[40] D. Tobjork and R. Osterbacka, "Paper Electronics," *Advanced Materials*, vol. 23, no. 17, p. 1935, 2011.

[41] S. Olberding, N.-W. Gong, J. Tiab, J. A. Paradiso and J. Steimle, "A Cuttable Multi-touch Sensor," in *Proceedings of the 26th annual ACM symposium on User interface software and technology* , St. Andrews, Scotland,, 2013.

[42] W. S. Bacon, "Now They're Printing TRANSISTORS ON PAPER!," *Popular Science*, 1968.

[43] T. Brody, "The thin film transistor: A late flowering bloom," *IEEE Transactions on Electron Devices*, vol. 31, no. 11, p. 1614, 1984.

[44] J. Hu, S. Wang, L. Wang, F. Li, B. Pingguan-Murphy, T. J. Lu and F. Xu, "Advances in paper-based point-of-care diagnostics," *Biosensors and Bioelectronics*, vol. 54, no. 15, p. 585, 2014.

[45] S. Felton, M. Tolley, E. Demaine, D. Rus and R. Wood, "A method for building self-folding machines," *Science*, vol. 345, no. 6197, p. 644, 2014.

[46] S. Wagner and S. Bauer, "Materials for stretchable electronics," *MRS Bulletin*, vol. 27, no. 3, p. 207, 2012.

[47] V. Lumelsky, M. Shur and S. Wagner, "Sensitive skin," *IEEE Sensors Journal*, vol. 1, no. 1, p. 41, 2001.

[48] M. D. Pickett, G. Medeiros-Ribeiro and R. S. Williams, "A scalable neuristor built with Mott memristors," *Nature Letters*, vol. 12, no. 2, p. 114, 2012.

[49] M. Salanne, B. Rotenberg, K. Naoi, K. Kaneko, P.-L. Taberna, C. P. Grey, B. Dunn and P. Simon, "Efficient storage mechanisms for building better supercapacitors," *Nature Energy,* vol. 1, 2015.

[50] R. D. Kornbluh, R. Pelrine, H. Prahlad and A. Wong-Foy, "Dielectric elastomers: Stretching the capabilities of energy harvesting," *MRS Bulletin,* vol. 37, no. 3, p. 246, 2012.

[51] C.-W. Nan and Q. Jia, "Obtaining ultimate functionalities in nanocomposites: Design, control, and fabrication," *MRS Bulletin,* vol. 40, no. 9, p. 719, 2015.

[52] T. Hanemann and D. V. Szabò, "Polymer-Nanoparticle Composites: From Synthesis to Modern Applications," *Materials,* vol. 3, no. 6, p. 3468, 2010.

[53] A. Heilmann, Polymer Films with Embedded Metal Nanoparticles, Berlin: Springer, 2003.

[54] Y. Yang, L. Ma and J. Wu, "Organic Thin-Film Memory," *MRS Bulletin,* vol. 29, no. 11, p. 833, 2004.

[55] C. A. Fantino E1, R. I., M. D., B. R., P. C.F. and C. F, "3D Printing: 3D Printing of Conductive Complex Structures with In Situ Generation of Silver Nanoparticles," *Advanced Materials,* vol. 28, no. 19, p. 3711, 2016.

[56] F. Faupel, V. Zaporojtchenko, H. Greve, U. Schürmann, V. S. K. Chakravadhanula, C. Hanisch, A. Kulkarni, A. Gerber, E. Quandt and R. Podschun, "Deposition of Nanocomposites by Plasmas," *Contributions to Plasma Physics,* vol. 47, no. 7, p. 537, 2007.

[57] W. Caseri, "Nanocomposites of polymers and metals or semiconductors: Historical background and optical properties," *Macromolecular Rapid Communications,* vol. 21, no. 11, p. 705, 2000.

[58] M. Elbahri, M. K. Hedayati, V. S. K. Chakravadhanula and T. M. Jamali, "An Omnidirectional Transparent Conducting-Metal-Based Plasmonic Nanocomposite," *Advanced Materials,* vol. 23, no. 17, p. 1993, 2011.

[59] G.-W. Huang, H.-M. Xiao and S.-Y. Fu, "Wearable Electronics of Silver-Nanowire/Poly(dimethylsiloxane) Nanocomposite for Smart Clothing," *Scientific Reports*, p. 13971, 2015.

[60] C. Hanisch, A. Kulkarni, V. Zaporojtchenko and F. Faupel, "Polymer-metal nanocomposites with 2-dimensional Au nanoparticle arrays for sensoric applications," *Journal of Physics: Conference Series*, vol. 100, no. 5, p. 52043, 2008.

[61] R. J. Tseng, J. Ouyang, C.-W. Chu, J. Huang and Y. Yang, "Nanoparticle-induced negative differential resistance and memory effect in polymer bistable light-emitting device," *Applied Physics Letters*, vol. 88, no. 12, p. 123506, 2006.

[62] F. Macionczyk and W. Brückner, "Tensile testing of AlCu thin films on polyimide foils," *Journal of Applied Physics*, vol. 86, p. 86, 1999.

[63] E. Kay and A. Dilks, "Metal-containing plasma polymerized fluorocarbon films—their synthesis, structure, and polymerization mechanism," *Journal of Vacuum Science & Technology* , vol. 16, no. 2, p. 428, 1979.

[64] K. Behnke, T. Strunskus, V. Zaporojtchenko and F. Faupel, "Metal/polymer interfaces and composite material prepared by vapor phase deposition," in *International Conference and Poster Exhibition Micro Materials*, Dresden, 2000.

[65] U. Schurmann, W. A. Hartung, H. Takele, V. Zaporojtchenko and F. Faupel, "Controlled syntheses of Ag–polytetrafluoroethylene nanocomposite thin films by co-sputtering from two magnetron sources," *Nanotechnology*, vol. 16, no. 8, p. 1078, 2005.

[66] P. Dubois, S. Rosset, M. Niklaus, M. Dadras and H. Shea, "Metal Ion Implanted Compliant Electrodes in Dielectric Electroactive Polymer (EAP) Membranes," *Advances in Science and Technology*, vol. 61, p. 18, 2008.

[67] C. Ghisleri, F. Borghi, L. Ravagnan, A. Podestà, C. Melis, L. Colombo and P. Milani, "Patterning of gold–polydimethylsiloxane(Au–PDMS) nanocomposites by supersonic cluster beam implantation," *Journal of Physics D: Applied Physics*, vol. 47, no. 1, 2014.

[68] F. Faupel, V. Zaporojtchenko, T. Strunskus and M. Elbahri, "Metal-Polymer Nanocomposites for Functional Applications," *Advanced engineering materials*, vol. 12, no. 12, p. 1177, 2010.

[69] Q. Chao, R. Ghadiri, T. Weigel, A. Aumann, E. L. Gurevich, C. Esen, O. Medenbach, W. Cheng, B. Chichkov and A. Ostendorf, "Comparison of in Situ and ex Situ Methods for Synthesis of Two-Photon Polymerization Polymer Nanocomposites," *Polymers*, vol. 6, no. 7, p. 2037, 2014.

[70] G. Carotenuto and L. Nicolais, "Size-controlled synthesis of thiol-derivatized gold clusters," *Journal of Materials Chemistry*, vol. 13, p. 1038, 2003.

[71] E. Hutter and J. H. Fendler, "Exploitation of localized surface plasmon resonance," *Advanced Materials*, vol. 16, p. 1685, 2004.

[72] T. Li and Z. Suo, "Ductility of thin metal films on polymer substrates modulated by interfacial adhesion," *International Journal of Solids and Structures*, vol. 44, no. 6, p. 1696, 2007.

[73] H. Huang and F. Spaepen, "Tensile testing of free-standing Cu, Ag and Al thin films and Ag/Cu multilayers," *Acta Materialia*, vol. 48, no. 12, p. 3261, 2000.

[74] S. L. Chiu, J. Leu and P. S. Ho, "Fracture of metal-polymer line structures. I. Semiflexible polyimide," *Journal of Applied Physics*, vol. 76, no. 9, p. 5136, 1994.

[75] T. Li, Z. Huang, Z. Suo, S. P. Lacour and S. Wagner, "Stretchability of thin metal films on elastomer substrates," *Applied Physics Letters*, vol. 85, no. 16, p. 3435, 2004.

[76] Y. Xiang, T. Li, Z. Suo and J. J. Vlassak, "High ductility of a metal film adherent on a polymer substrate," *Applied Physics Letters,* vol. 87, no. 16, p. 161910, 2005.

[77] H. Biederman, "Introduction," in *Plasma polymer films,* London, Imperial College Press, 2004.

[78] A. Biswas, Z. Marton, J. Kanzow, J. Kruse, V. Zaporojtchenko and F. Faupel, "Controlled Generation of Ni Nanoparticles in the Capping Layers of Teflon AF by Vapor-Phase Tandem Evaporation," *Nano letters,* vol. 3, no. 1, p. 69, 2003.

[79] F. Faupel, A. Thran, V. Zaporojtchenko, M. Kiene, T. Strunskus and K. Behnke, "Nucleation, growth, interdiffusion, and adhesion of metal films on polymers," in *Stress-Induced Phenomena in Metallization,* New York, 1999.

[80] V. Zaporojtchenko, T. Strunskus, K. Behnke, C. V. Bechtolsheim, M. Kiene and F. Faupel, "Metal/polymer interfaces with designed morphologies," *Journal of Adhesion Science and Technology,* vol. 14, no. 3, p. 467, 2000.

[81] A. Thran, M. Kiene, V. Zaporojtchenko and F. Faupel, "Condensation Coefficients of Ag on Polymers," *Physical Review Letters,* vol. 82, no. 9, p. 1903, 1999.

[82] H. Takele, H. Greve, C. Pochstein, V. Zaporojtchenko and F. Faupel, "Plasmonic properties of Ag nanoclusters in various polymer matrices," *Nanotechnology,* vol. 17, no. 14, p. 3499, 2006.

[83] S. Rosset and H. Shea, "Flexible and stretchable electrodes for dielectric elastomer actuators," *Applied Physics: A,* vol. 110, no. 2, p. 281, 2013.

[84] C. Laurent and E. Kay, "Properties of metal clusters in polymerized hydrocarbon versus fluorocarbon matrices," *Journal of Applied Physics,* vol. 65, no. 4, p. 1717, 1989.

[85] E. Kay, F. Parmigiani and W. Parrish, "Microstructure of sputtered metal films grown in high- and low-pressure discharges," *Journal of Vacuum Science & Technology A*, vol. 6, no. 6, p. 3074, 1988.

[86] H. Biederman, "RF sputtering of polymers and its potential application," *Vacuum*, vol. 59, no. 2-3, p. 594, 2000.

[87] S. Rosset, M. Niklaus, P. Dubois and H. Shea, "Metal Ion Implantation for the Fabrication of Stretchable Electrodes on Elastomers," *Advanced Functional Materials*, vol. 19, no. 3, p. 470, 2009.

[88] G. Corbelli, C. Ghisleri, M. Marelli, P. Milani and L. Ravagnan, "Highly deformable nanostructured elastomeric electrodes with improving conductivity upon cyclical stretching," *Advanced Materials*, vol. 23, no. 39, p. 4504, 2011.

[89] F. Borghi, C. Melis, C. Ghisleri, A. Podestà, L. Ravagnan, L. Colombo and P. Milani, "Stretchable nanocomposite electrodes with tunable mechanical properties by supersonic cluster beam implantation in elastomers," *Applied Physics Letters*, vol. 106, 2015.

[90] L. Tröger, H. Hünnefeld, S. Nunes, M. Oehring and D. Fritsch, "Structural Characterization of Catalytically Active Metal Nanoclusters in Poly(amide imide) Films with High Metal Loading," *The Journal of Physical Chemistry N*, vol. 101, no. 8, p. 1279, 1997.

[91] S. Wu, J. Shen, J. Huang, Y. Wu, Z. Zhang, Y. Hu, W. Wu, W. Huang, K. Wang and Q. Zhang, "Ag nanoparticle/azopolymer nanocomposites: In situ synthesis, microstructure, rewritable optically induced birefringence and optical recording," *Polymer*, vol. 51, no. 6, p. 1395, 2010.

[92] G. Whittell and I. Manners, "Metallopolymers: New Multifunctional Materials," *Advanced Materials*, vol. 19, no. 21, p. 3439, 2007.

[93] C.Burda, X. Chen, R. Narayanan and M. A. El-Sayed, "Chemistry and Properties of Nanocrystals of Different Shapes," *Chemical reviews*, vol. 105, no. 4, p. 1025, 2005.

[94] M. L. Yan, X. Z. Li, L. Gao, S. H. Liou, D. J. Sellmyer, R. J. M. v. d. Veerdonk and K. W. Wierman, "Fabrication of nonepitaxially grown double-layered FePt:C/FeCoNi thin films for perpendicular recording," *Applied Physics Letters,* vol. 83, no. 16, p. 3332, 2003.

[95] E. P. Giannelis, "Polymer Layered Silicate Nanocomposites," *Advanced Materials,* vol. 8, no. 1, p. 29, 1996.

[96] Z. Wang, Z. Zheng, J. Liu, Y. Wu and L. Zhang, "Tuning the Mechanical Properties of Polymer Nanocomposites Filled with Grafted Nanoparticles by Varying the Grafted Chain Length and Flexibility," *Polymers,* vol. 8, no. 9, p. 270, 2016.

[97] E. Guth and O. Gold, "On the hydrodynamical theory of the viscosity of suspensions," *Physical Review,* vol. 53, p. 322, 1938.

[98] Y.-P. Wu, Q.-X. Jia, D.-S. Yu and L.-Q. Zhang, "Modeling Young's modulus of rubber–clay nanocomposites using composite theories," *Polymer testing,* vol. 23, no. 8, p. 903, 2004.

[99] E. Guth, "Theory of filler reinforcemen," *Journal of Applied Physics,* vol. 16, no. 20, p. 20, 1945.

[100] B. Abeles, P. Sheng, M. Coutts and Y. Arie, "Structural and electrical properties of granular metal films," *Advances in Physics,* vol. 24, no. 3, p. 407, 1975.

[101] H. Takele, U. Schürmann, H. Greve, D. Paretkar, V. Zaporojtchenko and F. Faupel, "Controlled growth of Au nanoparticles in co-evaporated metal/polymer composite films and their optical and electrical properties," *The European Physical Journal Applied Physics,* vol. 33, no. 2, p. 83, 2006.

[102] G. Ambrosetti, On the Insulator-Conductor transition in polymer nanocomposites, These Ecole polytechnique federale de Lausanne EPFL, no. 4612, 2010.

[103] G. Ambrosetti, I. Balberg and C. Grimaldi, "Percolation-to-hopping crossover in conductor-insulator composites," *Physical Review B,* vol. 82, no. 13, p. 134201, 2010.

[104] G. Ambrosetti, N. Johner, C. Grimaldi, T. Maeder, P. Ryser and A. Danani, "Electron tunneling in conductor-insulator composites with spherical fillers," *Journal of Applied Physics,* vol. 106, no. 1, p. 16103, 2009.

[105] G. Corbelli, Synthesis and Charachterization of metal-polimer nanocomposites for stretchable electronics applications, Milano: Thesis Università degli Studi di Milano, 2011.

[106] S. Alam, M. Irfan, B. D. Soomro, M. Shahid and M. Zeeshan, "Optimization of loading factor of Nanocomposite Coatings deposited by Physical Vapor Deposition," *Journal of Physics: Conference Series,* vol. 439, no. 1, p. 012016, 2013.

[107] M. Ohring, "Chapter 6 – Chemical Vapor Deposition," in *Materials Science of Thin Films,* 2002, p. 277.

[108] P. H. Haumesser, "The Precipitation of Metals: Thin Film Electroplating and Nanoparticle Synthesis," in *Nucleation and Growth of Metals: From Thin Films to Nanoparticles,* 2016, p. 59.

[109] Y. Shacham-Diamand, T. Osaka, Y. Okinaka, A. Sugiyama and V. Dubin, "30years of electroless plating for semiconductor and polymer micro-systems," *Microelectronic Engineering* , vol. 132, no. C, p. 35, 2015.

[110] H.Minemawari, T. Yamada, H. Matsui, J. Tsutsumi, S. Haas, R. Chiba, R. Kumai and T. Hasegawa, "Inkjet printing of single-crystal films," *Nature,* vol. 475, no. 7356, p. 364, 2011.

[111] H. Gleskova, S. Wagner and Z. Suo, "Failure resistance of amorphous silicon transistors under extreme in-plane strain," *Applied Physics Letters,* vol. 75, no. 19, p. 3011, 1999.

[112] D. Kim, Y. Kim, J. Wu, Z. Liu, J. Song, H. Kim, Y. Huang, K. Hwang and J. Rogers, "Ultrathin Silicon Circuits With Strain-Isolation Layers and Mesh Layouts for High-Performance Electronics on Fabric, Vinyl, Leather, and Paper," *Advanced Materials,* vol. 21, no. 36, p. 3703, 2009.

[113] J. Sun, N. Lu, J. Yoon, K. Oh, Z. Suo and J. Vlassak, "Inorganic islands on a highly stretchable polyimide substrate," *Journal of Materials Research,* vol. 24, no. 11, p. 3338, 2011.

[114] S. Lacour, S. Wagner, R. Narayan, T. Li and Z. Suo, "Stiff subcircuit islands of diamondlike carbon for stretchable electronics," *Journal of Applied Physics ,* vol. 100, no. 1, p. 014913, 2006.

[115] EE Times europe, "Soothing flexible electronics take shape," 13 10 2013. [Online]. Available: http://www.electronics-eetimes.com/news/soothing-flexible-electronics-take-shape.

[116] A. Larmagnac, S. Eggenberger, H. Janossy and J. Voros, "Stretchable electronics based on Ag-PDMS composites," *Scientific Reports,* vol. 4, 2014.

[117] E. Barborini, P. Piseri and P. Milani, "A pulsed microplasma source of high intensity supersonic carbon cluster beams," *Journal of Physics D: Applied Physics,* vol. 32, p. L105, 1999.

[118] K. Wegner, P. Piseri, H. V. Tafreshi and P. Milani, "Cluster beam deposition: a tool for nanoscale science and technology," *Journal of physics D: Applied Physics,* vol. 39, p. R439, 2006.

[119] P. Piseri, H. Tafreshi and P. Milani, "Manipulation of nanoparticles in supersonic beams," *Current Opinion in Solid State and Materials Science,* vol. 8, p. 195, 2006.

[120] F. Di Fonzo, A. Gidwani., M. H. Fan, D. Neumann, D. I. Iordanoglou, J. V. R. Heberlein, P. H. McMurry, S. L. Girshick, N. Tymiak, W. Gerberich and N. P. Rao, "Focused nanoparticle-beam deposition of patterned microstructures," *Applied Physics Letters,* vol. 77, p. 910, 2000.

[121] F. Greco, V. Domenici, A. Desii, E. Sinibaldi, B. Zupančič, B. Zalar, B. Mazzolai and V. Mattoli, "Liquid single crystal elastomer/conducting polymer bilayer composite actuator: modelling and experiments," *Soft Matter,* vol. 9, p. 11405, 2013.

[122] Y.-B. Cohen and Q. Zhang, "Electroactive polymer actuators and sensors," *MRS Bulletin,* vol. 33, no. 3, p. 173, 2008.

[123] A. Mata, A. J. Fleischman and S. Roy, "Characterization of polydimethylsiloxane (PDMS) properties for biomedical micro/nanosystems," *Biomedical Microdevices,* vol. 7, no. 4, p. 281, 2005.

[124] J. N. Lee, C. Park and G. M. Whitesides, "Solvent Compatibility of Poly(dimethylsiloxane)-Based Microfluidic Devices," *Analytical chemistry,* vol. 75, no. 23, p. 6544, 2003.

[125] A. P. Gerratt and S. Bergbreiter, "Dielectric breakdown of PDMS thin films," *Journal og Micromechanics and Microengineering,* vol. 23, no. 6, p. 67001, 2013.

Appendix A: Conducting shrinkable nanocomposites based on Au-nanoparticle implanted plastic sheet: tunable thermally-induced surface wrinkling

Hereafter it is described the fabrication of a thermally shrinkable and conductive nanocomposite material prepared by SCBI of neutral Au nanoparticles into a commercially available thermo-retractable polystyrene (PS) sheet.

Letter

Conducting shrinkable nanocomposite based on Au-nanoparticle implanted plastic sheet: tunable thermally-induced surface wrinkling

Francesco Greco, Andrea Bellacicca, Mauro Gemmi, Valentina Cappello, Virgilio Mattoli, and Paolo Milani

ACS Appl. Mater. Interfaces, **Just Accepted Manuscript** • DOI: 10.1021/acsami.5b00825 • Publication Date (Web): 26 Mar 2015

ACS APPLIED MATERIALS & INTERFACES

Letter

www.acsami.org

Conducting Shrinkable Nanocomposite Based on Au-Nanoparticle Implanted Plastic Sheet: Tunable Thermally Induced Surface Wrinkling

Francesco Greco,*[,†] Andrea Bellacicca,[‡] Mauro Gemmi,[§] Valentina Cappello,[§] Virgilio Mattoli,[†] and Paolo Milani*[,‡]

[†]Center for Micro-BioRobotics @SSSA, Istituto Italiano di Tecnologia, Viale Rinaldo Piaggio 34, 56025 Pontedera, Italy

[‡]CIMAINA and Dipartimento di Fisica, Università degli Studi di Milano, via Celoria 16, 20133 Milano, Italy

[§]Center for Nanotechnology Innovation@NEST, Istituto Italiano di Tecnologia, Piazza San Silvestro 12, 56127 Pisa, Italy

Supporting Information

ABSTRACT: A thermally shrinkable and conductive nanocomposite material is prepared by supersonic cluster beam implantation (SCBI) of neutral Au nanoparticles (Au NPs) into a commercially available thermo-retractable polystyrene (PS) sheet. Micronanowrinkling is obtained during shrinking, which is studied by means of SEM, TEM and AFM imaging. Characteristic periodicity is determined and correlated with nanoparticle implantation dose, which permits us to tune the topographic pattern. Remarkable differences emerged with respect to the well-known case of wrinkling of bilayer metal−polymer. Wrinkled composite surfaces are characterized by a peculiar multiscale structuring that promises potential technological applications in the field of catalytic surfaces, sensors, biointerfaces, and optics, among others.

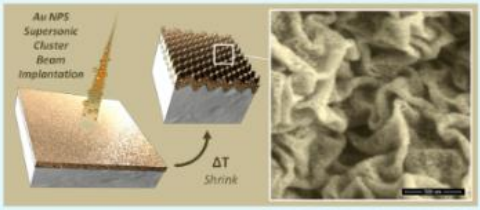

KEYWORDS: *surface wrinkling, metal NPs, implantation, nanocomposite, pattern, shrink, buckling*

Surface wrinkling is a self-organization phenomenon in which the surface of a stiff plate (or a "skin") coupled to a soft elastic substrate rearranges in wavy topographical features (wrinkles) when subjected to compressive stress exceeding a certain critical threshold.[1−3] The wavelength and the amplitude of the surface periodic structures depend on the intrinsic mechanical properties of the materials composing the bilayer system, on their thickness and on the amount of strain.[4] Surface wrinkling, driven by mechanical instability, is widely observed in natural systems such as human skin or fruits and leaves of plants, the physical mechanisms underlying it have been widely investigated.[5,6] The exploitation of surface wrinkling for the micro- and nanopatterning of surfaces has also been demonstrated recently as in view of different applications,[7,8] as well as a metrology technique for the characterization of the mechanical properties of thin films.[9] Microwrinkling has been demonstrated on the surface of shrinkable thermoplastics (e.g., commercially available films of thermoretractable polystyrene (PS) or polyolefins) subjected to heating. Wrinkled metallic surfaces obtained by depositing a metal film on shrinkable thermoplastics were reported by Khine and co-workers[10] and used as substrates for fluorescence enhancement.[11,12] Micro- and nanowrinkling was also successfully applied for the culturing and alignment of embryonic stem cells[13] and for the development of superhydrophobic and antibacterial surfaces.[14] Wrinkling of thermoretractable PS with a Pd thin film was used by Greco et al. for the development of a low-cost resistive hydrogen sensor.[15] The same group then reported wrinkling of the conductive polymer PEDOT:PSS on top of PS to obtain smart biointerfaces able to direct cell alignment and provide a means for their electrical/electrochemical stimulation.[16] Recently, a wrinkled surface composed of a thin (100 nm) film of pyrite (FeS_2) nanocrystals deposited on shrink-wrap film by spray coating has been presented as catalytic surface via Fenton chemistry for oxidative footprinting analysis of proteins.[17]

Polymer−metal nanocomposites are considered key ingredients for the fabrication of electronic skin, soft robots and smart touch sensors,[18,19] thus the micro- and nanopatterning of their surfaces would be highly beneficial for these applications; however, surface wrinkling of polymer nanocomposites embedding nanoparticles has not been demonstrated so far. This is mainly due to the intrinsic difficulty in producing nanocomposite systems able to shrink or to embed nanoparticles in preformed shrinkable materials without significantly altering their properties.

Received: January 27, 2015
Accepted: March 26, 2015
Published: March 26, 2015

DOI: 10.1021/acsami.5b00825
ACS Appl. Mater. Interfaces 2015, 7, 7060−7065

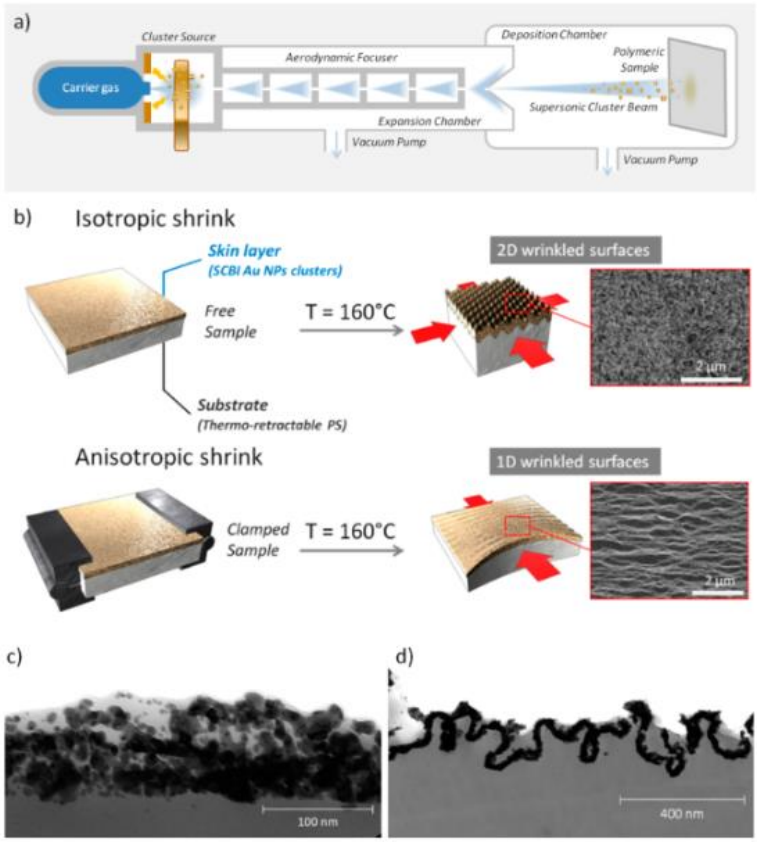

Figure 1. (a) Schematic view of AuNPs implantation process with SCBI apparatus. Neutral Au NPs (cluster size range 3−10 nm) are produced in a cluster source and accelerated by a carrier gas in a supersonic expansion. After being focused by a series of aerodynamic lenses the clusters beam impacts on the surface of a thermo-retractable PS sheet. (b) Scheme of thermally induced shrink processes for obtaining 1D and 2D wrinkling. TEM images of cross sections of AuNPs/PS composite (eq thickness, t_{eq} = 15 nm) cut by an ultramicrotome: (c) flat (not shrunk) sample; (d) 1D wrinkled sample.

Here we present a thermally shrinkable nanocomposite material obtained by supersonic cluster beam implantation (SCBI) of neutral Au nanoparticles (Au NPs) into a commercially available thermo-retractable polystyrene (PS) sheet (Polyshrink). By SCBI neutral metallic clusters are supersonically accelerated toward the surface of a target polymer film (Figure 1a).[20] The cluster kinetic energy is sufficient for implantation, while avoiding electrical charging and thermally induced modification of the polymeric substrate.[21] SCBI of metal nanoparticles in elastomers or thermoplastic polymers has been recently demonstrated as an efficient method for the microfabrication of flexible and stretchable conductive circuits and electrodes.[20−22]

After the implantation of Au nanoparticles (size distribution 3−10 nm) into the thermo-retractable polystyrene to produce an electrical conducting nanocomposite "skin" of AuNPs/PS (Figure 1c), we investigated surface wrinkling of the nanocomposite induced by thermal shrinking of the material at 40% of its original lateral dimension (Figure 1b). Isotropic surface wrinkling (biaxial 2D) was obtained on samples by inducing thermal shrinking at T = 160 °C for 6 min. By mechanically confining the shrinking of the material, we imposed the alignment of wrinkles along a given direction, creating anisotropic (uniaxially aligned, 1D) surface patterns (Figure1b).

We produced different nanocomposite samples with increasing nanoparticle implantation doses. We define an equivalent thickness t_{eq} as the thickness of the cluster-assembled film resulting from the same amount of implanted nanoparticles deposited on a hard substrate (e.g., glass) (see the Supporting Information). The equivalent thickness for the three different implantation doses investigated was varied in the range 8−15 nm.

Au nanoparticles were implanted to a depth of 70−80 nm below the surface (TEM image, Figure 1c). Such implantation depth, (the thickness of effective skin of nanocomposite AuNPs/PS) is considerably larger than the equivalent thick-

DOI: 10.1021/acsami.5b00825
ACS Appl. Mater. Interfaces 2015, 7, 7060−7065

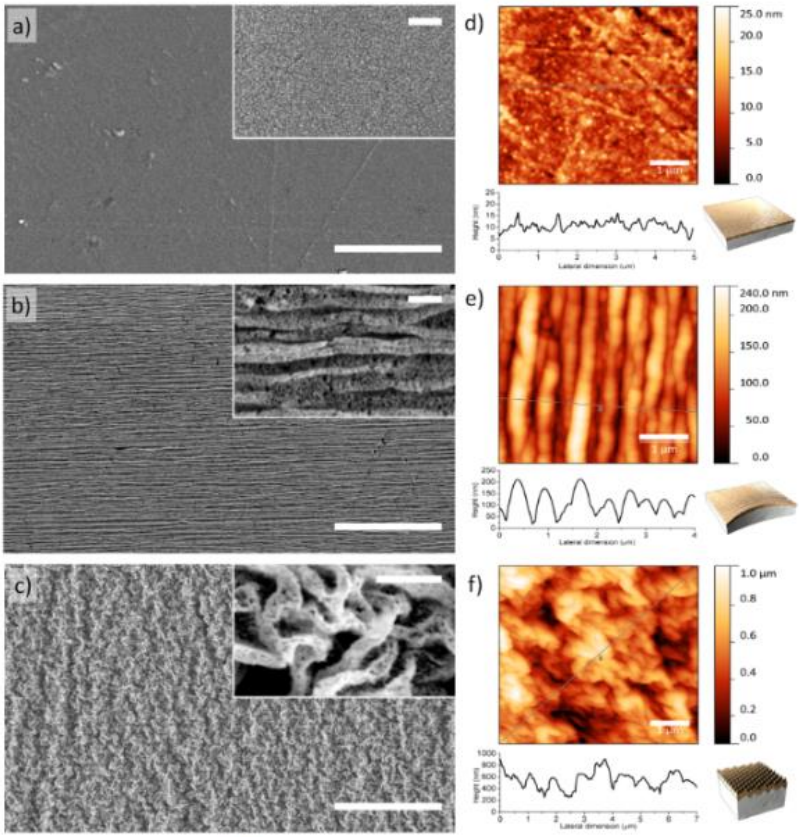

Figure 2. Micronanostructure and topography of nanocomposite with SCB-implanted Au NPs (t_{eq} = 15 nm). SEM images of (a) flat, (b) 1D wrinkled, and (c) 2D wrinkled samples; scale bar 10 μm (magnified inset scale bar 300 nm). AFM imaging and height profiles of (d) flat, (e) 1D wrinkled, and (f) 2D wrinkled samples. Scale bar 1 μm.

ness. Figure 1d shows the same sample after uniaxial shrinking. Along with formation of wrinkles, the implanted skin experienced a rearrangement: the implanted nanoparticles were compacted by compressive forces acting during the thermal shrinkage.

Upon thermal annealing and the subsequent shrinking, we observed the wrinkling of the nanocomposites (Figure 2): investigation of the surface by means of SEM and AFM imaging clearly evidenced the formation of wrinkles with submicrometric spatial periodicity and topographic reliefs over the whole implanted surface.

By comparing samples with identical implantation doses (t_{eq} = 15 ± 2 nm) but different shrinking conditions (no shrink, 1D shrink, 2D shrink) it is possible to appreciate the evolution of wrinkling and how it is affecting sample topography (Figure 2a-f). Interestingly, nanoscale roughness/porosity is evidenced in SEM images at higher magnification (inset of Figure 2b, c), and is related to the size of metal clusters and gaps between adjacent clusters. The superposition of features at different scales, namely the nanostructuring (given by the cluster arrangement of nanocomposite) combined with the microstructuring (driven by wrinkling), is interesting in view of different applications, such as the development of catalytic surfaces for sensing, energy harvesting or also for optics.[2,3]

We compared wrinkled implanted nanocomposites with Au/PS bilayer with gold layers of similar thickness deposited by sputter coating (no implantation).[10] In the latter case, the "skin" which is subjected to wrinkling is a quite uniform and stiff metal layer that is deformed by compression when the substrate (PS) is heat-shrunk. The gold layer act as a solid barrier which does not permit any flow of the PS (a viscoelastic fluid at at T = 160 °C, that is well above its glass transition temperature $T_g \approx$ 100 °C) toward the surface; a sharp boundary between PS and wrinkled Au is reported.[10] On the contrary, in our nanocomposite, such mass flow is allowed (especially at low implantation dose), so that wrinkles are well-embedded and partially buried down in PS, as visible in TEM of cross-sections (Figure 1d). As an important implication, incorporation of wrinkled conductive skin in the material causes a very strong adhesion. These observations are further

DOI: 10.1021/acsami.5b00825
ACS Appl. Mater. Interfaces 2015, 7, 7060−7065

confirmed by the AFM profiles reported in Figure 2 e, f: instead of a quasi-sinusoidal profile, as one could expect to be formed by a wrinkling phenomenon, only an half-wave profile is observed, with a peak-to-valley amplitude that is lower than the full amplitude of wrinkles, as observed in TEM images.

By varying the nanoparticle implantation dose, we were able to tune the surface topographical patterns as well as to modulate the electrical conductance G of the nanocomposite. The latter showed an evolution corresponding to a sharp increase (5–6 orders of magnitude) with increasing the implantation dose (Figure 3b), as a result of increased connectivity of implanted conductive particles.[21] Shrinked samples exhibited even better electrical conductivity, with ca. 20–50 times improvement of conductance of 2D wrinkled samples with respect to the flat. Moreover, 1D wrinkled samples showed anisotropic electrical behavior. Conductance measured along perpendicular direction to wrinkles (i.e., the direction on which shrink was allowed during sample preparation) had a similar improvement as observed in 2D samples, while only a ca. 10 times conductance improvement with respect to flat was assessed along parallel direction to wrinkles.

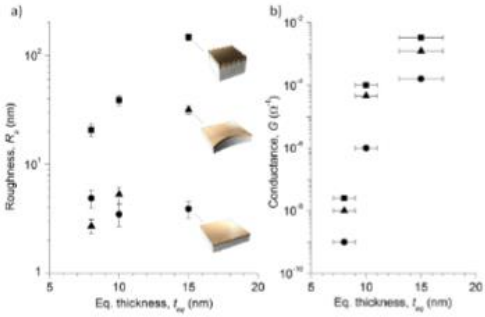

Figure 3. (a) Surface roughness R_a and (b) conductance G of SCB-implanted nanocomposites with different shrinking geometries (flat (not shrunk), circle; 1D wrinkled, triangle; 2D wrinkled, square) as a function of Au NPs t_{eq} (implantation dose).

Average surface roughness R_a of flat (not shrunk) samples, as measured by AFM images analysis, was almost unaffected by increasing the implantation dose. On the other hand, roughness R_a remarkably increased with implantation dose (equivalent thickness) in the case of shrunk nanocomposites, as a result of surface wrinkling (Figure 3a). Noteworthy, by increasing the implantation dose (i.e., the equivalent thickness) no significant change in implantation depth was observed (data not shown); this result is in agreement with previous findings of nanoparticle implantation in PDMS, in which implantation depth was found to be larger (~120 nm), because of its lower modulus, 100 kPa, with respect to polystyrene, 1–2 GPa, and independent of implantation dose.[22]

On the contrary, the observed wrinkling behavior strongly depends upon the implantation dose: as implantation dose was varied ($5 < t_{eq} < 15$ nm) features with distinctly different characteristic size were obtained. A collection of SEM, AFM, and TEM images of samples at all the different t_{eq} and shrinking geometries are reported in the Supporting Information (Figure S1–S3). Noteworthy, the grainlike structure of the nanocomposite made of individual clusters is better emerging in

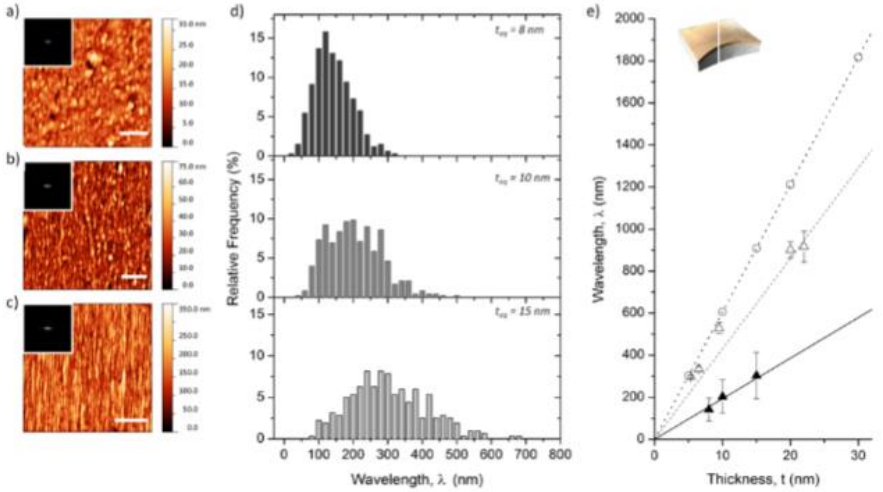

Figure 4. Uniaxially wrinkled (1D) nanocomposites: tunability of surface topography with implantation dose/equivalent thickness of SCB-implanted AuNPs. AFM images and corresponding FFT modulus of 1D samples at different eq thickness: (a) t_{eq} = 8 nm (scale bar 1 μm), (b) t_{eq} = 10 nm (scale bar 2 μm), (c) t_{eq} = 15 nm (scale bar 5 μm). (d) Relative frequency distributions of wrinkle wavelength λ, as estimated by AFM: t_{eq} = 8 nm (top panel), t_{eq} = 10 nm (middle), t_{eq} = 15 nm (bottom). (e) Average wrinkle wavelength λ as a function of t_{eq}: comparison among SCBI Au-NPs composites (black solid triangles), bilayer with sputter-coated Au thin films (open triangles) and theoretical prediction from eq 1 (circles).[2] Linear fits are represented with lines.

DOI: 10.1021/acsami.5b00825
ACS Appl. Mater. Interfaces 2015, 7, 7060–7065

samples at lower t_{eq} because of the lower amount of implanted AuNPs. To investigate the effects on wrinkling of increasing implantation dose we performed a quantitative analysis on AFM profiles (Figure 4a−c) to evaluate wrinkles alignment and to extract characteristic periodicity (wavelength) of wrinkles in the case of 1D samples. FFT of AFM images (inset of Figure 4a−c) highlight the anisotropic nature of wrinkling with good alignment of wrinkles along vertical direction for all the studied samples. Furthermore, in our analysis, we measured the wavelength λ as the distance between neighboring peaks in the AFM profiles and reconstructed the distribution of measured λ in order to describe heterogeneity of the wrinkling. By increasing the implantation dose the λ distribution broadened and shifted toward larger values (Figure 4d). Notably all the samples were characterized by nanowrinkling with median values of distributions varying from 130 to 300 nm, and distribution ranging from some tens of nanometers (t_{eq} = 8 nm) up to 680 nm (t_{eq} = 15 nm). It is important to notice that such values are among the lowest ever reported for wrinkling.

Deeper insight in these results can be gained by a comparison with experimental results of wrinkling obtained in the case of Au films deposited on top of PS by means of sputter coating (not implanted), and with predictions of a model for wrinkling. By considering the common model that describes wrinkling on an elastic substrate, spatial periodicity of wrinkles along the surface plane (characteristic wavelength λ) is determined solely by the thickness and by intrinsic material properties of the "skin" film and the soft substrate[2]

$$\lambda = 2\pi t \left[\frac{(1-\nu_s^2)E_f}{3(1-\nu_f^2)E_s} \right]^{1/3} \quad (1)$$

where t is the thickness of the film, E is the Young's modulus, ν is the Poisson ratio, f and s subscripts denote film and substrate, respectively.

Figure 4e reports the trend of characteristic λ as a function of nanoparticle equivalent thickness. Values of λ predicted by eq 1 are also reported; the material parameters used in calculation were taken from available literature and were E_f = 60 GPa, ν_f = 0.33 for sputter-coated Au,[24,25] and E_s = 20 MPa, ν_s = 0.45 for PS (at T = 160 °C, that is, the temperature at which shrinking is operated and wrinkles are generated).[26,27]

A remarkable difference in λ is observed between Au implanted nanocomposite and sputter coated Au with similar thickness on top of identical PS substrates. These results further confirm the hypothesis that the effective implanted skin layer has the properties of a nanocomposite. Indeed, by considering eq 1, $\lambda \propto (E_f/E_s)^{1/3}$, wrinkle wavelength depends on intrinsic properties of the materials: the ratio of elastic moduli of film and substrate. Thus, the finding of smaller λ and different slope in the case of implanted AuNPs is an indirect evidence for the formation of a skin layer whose elastic modulus is lower than a continuous Au film and higher than PS. This is in accordance with the behavior of a nanocomposite whose modulus is a combination of moduli of constituent materials. The not perfect accordance of predictions of eq 1 with experimental data found in the case of sputter coated Au samples is explained taking into account several factors: (i) model of eq 1 is based on the assumption of a perfectly elastic substrate, which is not the case for PS (at $T > T_g$) whose behavior is rather affected by viscoelasticity; (ii) data of E and υ taken from literature (Au, PS) must be considered as "order of magnitude" estimate: there are no available data on the materials used in this research, at same thickness; (iii) as regards sputter coated ultrathin Au film, it is known to have a transition in physical properties (elastic modulus, electrical resistivity) exactly in the thickness range of interest (5−15 nm), because of its grain structure and discontinuity during growth, which is completely avoided only at thickness >13−15 nm.[16,24]

In conclusion, we reported the fabrication and characterization of a metal−polymer nanocomposite which creates surface wrinkles at the micro and nanoscale on large areas upon shrinking. Implantation of Au NPs by SCBI in a commercial shrinkable thermoplastic material permitted to avoid its modification upon implantation, thus maintaining the relevant properties of the polymer matrix and of its surface, while imparting electrical conductivity. Surface characterization by means of SEM, AFM, and TEM permitted us to obtain a clear view of wrinkle formation and highlight the relevant differences between such a system and common wrinkled bilayers of metal/polymer. Notably, because of the nanocomposite nature of the implanted "skin", wrinkles are partly buried down into the material. By changing the implantation dose, we were able to follow and to control the corresponding evolution of wrinkling, as well as the electrical conductivity of the nanocomposite. Relevant improvement of conductive properties was observed upon shrink-induced wrinkling, with anisotropic behavior in the case of aligned wrinkles. The combination of features at the nanoscale and at hundreds of nanometer scale of the nanocomposite and the possibility to tune them by changing the amount of implanted nanoparticles are unique and they could open the way to several applications requiring multiscale integration and organization of periodic structures in the field of optics, biointerfacing, sensing, and microfabrication.

■ ASSOCIATED CONTENT

Supporting Information

Details about experimental procedures. Figures S1−S4, reporting SEM, AFM, and TEM images of all samples investigated in dependence of implantation dose and shrinking geometry. This material is available free of charge via the Internet at http://pubs.acs.org.

■ AUTHOR INFORMATION

Corresponding Authors

*E-mail: francesco.greco@iit.it.
*E-mail: paolo.milani@mi.infn.it.

Notes

The authors declare no competing financial interest.

■ ACKNOWLEDGMENTS

The authors acknowledge Paola Parlanti for assistance during the cutting process.

■ REFERENCES

(1) Groenewold, J. Wrinkling of Plates Coupled with Soft Elastic Media. *Phys. A* **2001**, *298*, 32−45.
(2) Genzer, J.; Groenewold, J. Soft Matter with Hard Skin: From Skin Wrinkles to Templating and Material Characterization. *Soft Matter* **2006**, *2*, 310−323.
(3) Bowden, N.; Brittain, S.; Evans, A. G.; Hutchinson, J. W.; Whitesides, G. M. Spontaneous Formation of Ordered Structures in Thin Films of Metals Supported on an Elastomeric Polymer. *Nature* **1998**, *393*, 146−149.

DOI: 10.1021/acsami.5b00825
ACS Appl. Mater. Interfaces 2015, 7, 7060−7065

(4) Cerda, E.; Ravi-Chandar, K.; Mahadevan, L. Thin Films: Wrinkling of an Elastic Sheet under Tension. *Nature* **2002**, *419*, 579−580.
(5) Huck, W. T. S.; Bowden, N.; Onck, P.; Pardoen, T.; Hutchinson, J. W.; Whitesides, G. M. Ordering of Spontaneously Formed Buckles on Planar Surfaces. *Langmuir* **2000**, *16*, 3497−3501.
(6) Efimenko, K.; Rackaitis, M.; Manias, E.; Vaziri, A.; Mahadevan, L.; Genzer, J. Nested Self-Similar Wrinkling Patterns in Skins. *Nat. Mater.* **2005**, *4*, 293−297.
(7) Chen, C. M.; Yang, S. Wrinkling Instabilities in Polymer Films and Their Applications. *Polym. Int.* **2012**, *61*, 1041−1047.
(8) Mei, Y.; Kiravittaya, S.; Harazim, S.; Schmidt, O. G. Principles and Applications of Micro and Nanoscale Wrinkles. *Mater. Sci. Eng., R* **2010**, *70*, 209−224.
(9) Stafford, C. M.; Harrison, C.; Beers, K. L.; Karim, A.; Amis, E. J.; VanLandingham, M. R.; Kim, H.-C.; Volksen, W.; Miller, R. D.; Simonyi, E. E. A Buckling-Based Metrology for Measuring the Elastic Moduli of Polymeric Thin Films. *Nat. Mater.* **2004**, *3*, 545−550.
(10) Fu, C. C.; Grimes, A.; Long, M.; Ferri, C. G. L.; Rich, B. D.; Ghosh, S.; Lee, L. P.; Gopinathan, A.; Khine, M. Tunable Nanowrinkles on Shape Memory Polymer Sheets. *Adv. Mater.* **2009**, *21*, 4472−4476.
(11) Fu, C. C.; Ossato, G.; Long, M.; Digman, M. A.; Gopinathan, A.; Lee, L. P.; Gratton, E.; Khine, M. Bimetallic Nanopetals for Thousand-Fold Fluorescence Enhancements. *Appl. Phys. Lett.* **2010**, *97*, 203101.
(12) Sharma, H.; Digman, M. A.; Felsinger, N.; Gratton, E.; Khine, M. Enhanced Emission of Fluorophores on Shrink-Induced Wrinkled Composite Structures. *Opt. Mater. Express* **2014**, *4*, 753−763.
(13) Chen, A.; Lieu, D. K.; Freschauf, L.; Lew, V.; Sharma, H.; Wang, J.; Nguyen, D.; Karakikes, I.; Hajjar, R. J.; Gopinathan, A.; Botvinick, E.; Fowlkes, C. C.; Li, R. A.; Khine, M. Shrink-Film Configurable Multiscale Wrinkles for Functional Alignment of Human Embryonic Stem Cells and Their Cardiac Derivatives. *Adv. Mater.* **2011**, *23*, 5785−5791.
(14) Freschauf, L. R.; McLane, J.; Sharma, H.; Khine, M. Shrink-Induced Superhydrophobic and Antibacterial Surfaces in Consumer Plastics. *PLoS One* **2012**, *7*, e40987.
(15) Greco, F.; Ventrelli, L.; Dario, P.; Mazzolai, B.; Mattoli, V. Micro-Wrinkled Palladium Surface for Hydrogen Sensing and Switched Detection of Lower Flammability Limit. *Int. J. Hydrogen Energy* **2012**, *37*, 17529−17539.
(16) Greco, F.; Fujie, T.; Ricotti, L.; Taccola, S.; Mazzolai, B.; Mattoli, V. Microwrinkled Conducting Polymer Interface for Anisotropic Multicellular Alignment. *ACS Appl. Mater. Interfaces* **2013**, *5*, 573−584.
(17) Leser, M.; Pegan, J.; El Makkaoui, M.; Schlatterer, J. C.; Khine, M.; Law, M.; Brenowitz, M. Protein Footprinting by Pyrite Shrink-Wrap Laminate. *Lab Chip* **2015**, *15*, 1646−1650.
(18) Hammock, M. L.; Chortos, A.; Tee, B. C. K.; Tok, J. B. H.; Bao, Z. 25th Anniversary Article: The Evolution of Electronic Skin (E-Skin): A Brief History, Design Considerations, and Recent Progress. *Adv. Mater.* **2013**, *25*, 5997−6038.
(19) Bauer, S.; Bauer-Gogonea, S.; Graz, I.; Kaltenbrunner, M.; Keplinger, C.; Schwödiauer, R. 25th Anniversary Article: A Soft Future: From Robots and Sensor Skin to Energy Harvesters. *Adv. Mater.* **2014**, *26*, 149−162.
(20) Ravagnan, L.; Divitini, G.; Rebasti, S.; Marelli, M.; Piseri, P.; Milani, P. Poly(Methyl Methacrylate)-Palladium Clusters Nanocomposite Formation by Supersonic Cluster Beam Deposition: A Method for Microstructured Metallization of Polymer Surfaces. *J. Phys. D: Appl. Phys.* **2009**, *42*, 082002.
(21) Corbelli, G.; Ghisleri, C.; Marelli, M.; Milani, P.; Ravagnan, L. Highly Deformable Nanostructured Elastomeric Electrodes with Improving Conductivity Upon Cyclical Stretching. *Adv. Mater.* **2011**, *23*, 4504−4508.
(22) Ghisleri, C.; Borghi, F.; Ravagnan, L.; Podestà, A.; Melis, C.; Colombo, L.; Milani, P. Patterning of Gold-Polydimethylsiloxane (Au-Pdms) Nanocomposites by Supersonic Cluster Beam Implantation. *J. Phys. D: Appl. Phys.* **2014**, *47*, 015301.
(23) Zhang, L.; Lang, X.; Hirata, A.; Chen, M. Wrinkled Nanoporous Gold Films with Ultrahigh Surface-Enhanced Raman Scattering Enhancement. *ACS Nano* **2011**, *5*, 4407−4413.
(24) Salvadori, M.; Brown, I.; Vaz, A.; Melo, L.; Cattani, M. Measurement of the Elastic Modulus of Nanostructured Gold and Platinum Thin Films. *Phys. Rev. B: Condens. Matter Mater. Phys.* **2003**, *67*, 153404.
(25) Cao, C.; Chan, H. F.; Zang, J.; Leong, K. W.; Zhao, X. Harnessing Localized Ridges for High-Aspect-Ratio Hierarchical Patterns with Dynamic Tunability and Multifunctionality. *Adv. Mater.* **2014**, *26*, 1763−1770.
(26) Gedde, U. *Polymer Physics*; Springer: New York, 1995.
(27) Mott, P. H.; Dorgan, J. R.; Roland, C. M. The Bulk Modulus and Poisson's Ratio of "Incompressible" Materials. *J. Sound Vibration* **2008**, *312*, 572−575.

DOI: 10.1021/acsami.5b00825
ACS Appl. Mater. Interfaces 2015, 7, 7060−7065